

Design Optimization of Thermal Paths in Spacecraft Systems

by

Kevin Dale Stout

B.S. Aerospace Engineering
The University of Texas at Austin (2011)

Submitted to the Department of Aeronautics and Astronautics
in partial fulfillment of the requirements for the degree of

Master of Science in Aeronautics and Astronautics

at the

MASSACHUSETTS INSTITUTE OF TECHNOLOGY

June 2013

**This material is declared a work of the U.S. Government and is not subject to
copyright protection in the United States.**

Author
Department of Aeronautics and Astronautics
May 16, 2013

Certified by
Rebecca A. Masterson
Research Engineer
Thesis Supervisor

Certified by
David W. Miller
Professor of Aeronautics and Astronautics
Thesis Supervisor

Accepted by
Eytan H. Modiano
Professor of Aeronautics and Astronautics
Chair, Graduate Program Committee

DISCLAIMER CLAUSE: The views expressed in this article are those of the author and do not reflect the official policy or position of the United States Air Force, Department of Defense, or the U.S. Government.

Design Optimization of Thermal Paths in Spacecraft Systems

by

Kevin Dale Stout

Submitted to the Department of Aeronautics and Astronautics
on May 16, 2013, in partial fulfillment of the
requirements for the degree of
Master of Science in Aeronautics and Astronautics

Abstract

This thesis introduces a thermal design approach to increase thermal control system performance and decrease reliance on system resources, e.g., mass. Thermal design optimization has lagged other subsystems because the thermal subsystem is not thought to significantly drive performance or resource consumption. However, there are factors present in many spacecraft systems that invalidate this assumption. Traditional thermal design methods include point designs where experts make key component selection and sizing decisions. Thermal design optimization literature primarily focuses on optimization of the components in isolation from other parts of the thermal control system, restricting the design space considered.

The collective thermal design optimization process formulates the thermal path design process as an optimization problem where the design variables are updated for each candidate design. Parametric model(s) within the optimizer predict the performance and properties of candidate designs. The thermal path parameterization captures the component interactions with each other, the system, and the space environment, and is critical to preserving the full design space. The optimal design is a thermal path with higher performance and decreased resource consumption compared to traditional thermal design methods.

The REgolith X-ray Imaging Spectrometer (REXIS) payload instrument serves as a case study to demonstrate the collective thermal design optimization process. First, a preliminary thermal control system model of a point design is used to determine the critical thermal path within REXIS: the thermal strap and radiator assembly. The collective thermal design optimization process is implemented on the thermal strap and radiator thermal path. Mass minimization is the objective and the REXIS detector operational temperature is a constraint to the optimization. This approach offers a 37% reduction in mass of the thermal strap and radiator assembly over a component-level optimization method.

Thesis Supervisor: Rebecca A. Masterson

Title: Research Engineer

Thesis Supervisor: David W. Miller

Title: Professor of Aeronautics of Astronautics

DISCLAIMER CLAUSE: The views expressed in this article are those of the author and do not reflect the official policy or position of the United States Air Force, Department of Defense, or the U.S. Government.

Acknowledgments

I thank God for His mercy and the strength He has provided me throughout my life. His sovereignty in both the good times and the bad are constant reminders of the gifts I have been given. I would like to thank my wife Andrea for her unending support. She is my best friend and I cannot wait to see what the future has in store for us. I would also like to thank my entire family – especially my parents, Michael Stout and Antoinette Nelson, and my sister Amanda Stout – for their love and encouragement. Without their influence, I never would have found myself on a path to MIT.

Thank you to my advisors Professor David Miller and Dr. Rebecca Masterson for the opportunity to be a part of the Space Systems Laboratory. Their mentorship has greatly improved my technical skills as a systems engineer. Furthermore, I'd like to thank other MIT faculty/staff and my peers who encouraged and help me work through my SM degree.

I would like to express my sincere gratitude to the United States Air Force for this academic opportunity. The Air Force ROTC Detachment 825 at the University of Texas at Austin taught me responsibility, teamwork, and leadership. I will always consider Det 825, the cadre and cadets, my first Air Force home. Dr. Hans Mark, Col Christopher Bowman (Ret), and Col Jeffrey Staha took a chance on me during my time in Det 825 at the University of Texas at Austin. Their efforts to enable my first assignment at MIT are both humbling and generous. I thank them for their mentorship, support, and guidance.

The summer internships during my undergraduate education in Group 93 at Lincoln Laboratory heavily influenced my graduate school path. I would like to express my appreciation to Zachary Folcik, Dr. Rick Abbot, and Dr. David Chan for the opportunity to work in Group 93 and providing me with motivation to attend MIT as a graduate student.

Table of Contents

Abstract	2
Acknowledgments.....	3
List of Figures	6
List of Tables	7
Acronym and Notation List	8
Chapter 1 – Introduction	9
1.1 Motivation	9
1.2 Literature Review	14
1.3 Traditional Thermal Design Process	18
1.4 Research Hypothesis and Objective	20
1.5 Thesis Roadmap	21
Chapter 2 – Background	24
2.1 REXIS Instrument Overview	24
2.1.1 OSIRIS-REx and REXIS Project Overview	24
2.1.2 REXIS Science Mission.....	25
2.1.3 Design Overview	26
2.2 Thermal Modeling.....	28
2.2.1 General Heat Transfer Equation	28
2.2.2 General Thermal Environment	29
2.2.3 Methods of Heat Transfer	32
2.2.4 Resistor Network Model	34
Chapter 3 – Methodology	42
3.1 Parameterization of Thermal Path.....	44
3.2 Creation of Thermal Path Model(s).....	47
3.3 Generation of Critical Figures of Merit and Optimization Formulation	48
3.4 Survey of Optimization Routines	51
Chapter 4 – Preliminary REXIS Thermal Control System Design Evaluation	56
4.1 REXIS Thermal Control System Architecture and Design.....	56
4.1.1 Requirements	56
4.1.2 Architecture.....	57
4.1.3 Design Elements	59
4.2 Reduced-Order Thermal Model	61

4.3	Thermal Model Predictions	64
4.3.1	Mission scenarios.....	64
4.3.2	Model Predictions	66
4.4	Model Verification	68
4.5	Identification of Critical Thermal Paths	71
4.6	Summary	73
Chapter 5	– Design Optimization of the REXIS Thermal Strap and Radiator Thermal Path ...	74
5.1	Parameterization of Thermal Path.....	74
5.2	Models of Thermal Path	79
5.3	Definition of Figures of Merit.....	84
5.4	Optimization Problem Formulation.....	84
5.5	Results	86
5.6	Summary	96
Chapter 6	– Conclusion.....	97
6.1	Thesis Summary	97
6.2	Contributions	98
6.3	Future Work	98
Chapter 7	– References	100
Appendix A:	REXIS N ² Diagram	103
Appendix B:	REXIS Reduced-order Model Code.....	104
Appendix C:	Thermal Strap and Radiator Nonlinear Model Code.....	118
Appendix D:	Linearized Resistor Network 3-D Radiator Thermal Model.....	129
Appendix E:	REXIS Preliminary Design Review Thermal Model	132

List of Figures

Figure 1: Dry mass distribution of average earth-orbiting spacecraft [2].....	11
Figure 2: James Webb Space Telescope [3] and REXIS; examples of cold regime space systems with a higher than average thermal mass fraction	12
Figure 3: Relationship of thesis work with prior research.....	14
Figure 4: Hull, et al. [4] radiator shape variation and design optimization	16
Figure 5: Muraoka, et al. [11] design optimization of MMP panels.....	17
Figure 6: Vlassov, et al. [13] heat pipe and radiator assembly geometry from for design optimization.....	18
Figure 7: Traditional thermal design process [14].....	18
Figure 8: Notional illustration of component-level and collective optimization of thermal paths.....	21
Figure 9: Thesis roadmap	22
Figure 10: Top view of REXIS on the instrument deck of OSIRIS-REX.....	25
Figure 11: REXIS design overview	27
Figure 12: General spacecraft system thermal environment [14]	30
Figure 13: 1-D conduction through a homogenous material [18].....	33
Figure 14: 2-D resistor grid representation of radiator plate.....	36
Figure 15: Resistor connectivity at arbitrary node location (i,j) of radiator	37
Figure 16: Sample nodal matrix structure for 2-D radiator with 10 x 100 discretization.....	39
Figure 17: Collective thermal design optimization process.....	42
Figure 18: Example 1-D heat conduction problem	46
Figure 19: Gradient-based optimization process [24]	52
Figure 20: REXIS thermal architecture	58
Figure 21: N ² diagram for REXIS TCS	60
Figure 22: Reduced-order model formulation	62
Figure 23: Reduced-order model code structure	63
Figure 24: Notional geometry for REXIS during Orbit Phase B	66
Figure 25: Reduced-order model predictions for Orbit Phase B	67
Figure 26: Model verification process.....	69
Figure 27: Thermal Desktop model of REXIS	70
Figure 28: Sensitivity Analysis of REXIS thermal paths using reduced-order model.....	72
Figure 29: REXIS TCS Concept	75
Figure 30: Thermal strap and radiator thermal path diagram.....	77
Figure 31: Thermal strap and radiator thermal path parameterization	79
Figure 32: Thermal strap and radiator thermal model.....	80
Figure 33: Thermal model governing equations definition.....	81
Figure 34: Design variable values for design solution of thermal strap and radiator thermal path (numerical values in Table 16).....	87
Figure 35: Radiator temperature distribution [°C]	90
Figure 36: Mass sensitivity analysis at optimal design	91
Figure 37: Detector temperature sensitivity analysis at optimal design	92
Figure 38: Pareto frontier of thermal strap and radiator thermal path of total mass versus detector temperature	95

List of Tables

Table 1: Enumeration of what constitutes a complete thermal path	15
Table 2: Example spacecraft thermal control components.....	20
Table 3: Resistor network analogy for multiple engineering disciplines for 1-D flow.....	34
Table 4: Parameter file for 1-D heat conduction problem	46
Table 5: Example FOMs for a thermal path	49
Table 6: Commonly used heuristic optimization algorithms	54
Table 7: Summary of gradient-based and heuristic algorithm advantages and disadvantages	55
Table 8: REXIS driving TCS requirements	57
Table 9: Thermally bounding nominal mission scenarios for REXIS.....	65
Table 10: Summary of reduced-order model predictions	67
Table 11: Model verification results of reduced-order model with Thermal Desktop model	71
Table 12: Design variables in parameter file for thermal strap and radiator thermal path.....	78
Table 13: Thermal strap and radiator FOMs	84
Table 14: Optimization algorithm selection criteria.....	85
Table 15: Design solution thermal strap and radiator masses.....	86
Table 16: Numerical design variable values for optimal thermal path solution	88
Table 17: Comparison of collective to component-level thermal design optimization	93

Acronym and Notation List

CCD – Charge-coupled Device

DAM – Detector Assembly Mechanism

DASS – Detector Assembly Support Structure

DE – Detector Electronics

ETU – Engineering Test Unit

FOM – Figure of Merit

FPGA – Field-Programmable Gate Array

GEO – Geosynchronous Earth Orbit

HCO – Harvard College Observatory

JWST – James Webb Space Telescope

KCL – Kirchhoff's Current Law

MEB – Main Electronics Board

MLI – Multi-layer Insulation

OSIRIS-REx – Origins-Spectral Interpretation-Resource Identification-Security-Regolith Explorer

PCB – Printed circuit board

REXIS – REgolith X-ray Imaging Spectrometer

SQP – Sequential Quadratic Programming

SSL – Space Systems Laboratory

SXM – Solar X-ray Monitor

TCS – Thermal Control Systems

TID – Total Ionizing Dose

TIL – Thermal Isolation Layer

XRF – X-ray Fluorescence

Chapter 1 – Introduction

1.1 Motivation

The primary responsibility of spacecraft thermal control systems (TCS) is to maintain component temperature ranges, both operational and survival, for the duration of the mission. Preliminary TCS design typically consists of experts making critical component selection and sizing decisions aided by hand calculations. After considering the mission thermal environment, the thermal engineer provides initial inputs to engineers designing other subsystems. As the system design achieves definition, a thermal model is used to evaluate candidate designs. Only then does the thermal engineer begin detailed TCS design.

The central focus of this thesis is collectively optimizing all components along a thermal path in order to improve the TCS design process. To clarify, a thermal path is the tracing of heat flow from the point or surface where it enters the system, through the system, to the point or surface where it leaves the system. Thus, a system can be composed of many thermal paths depending on its size and complexity.

The high cost of spaceflight, particularly the cost of the launch vehicle, dictates the operational cadence of space missions. System resources for a spacecraft system are fundamentally limited by the capacity of the launch vehicle fairing. Consequently, the cost per pound to orbit remains very high. As an intermediate benchmark, \$12k per pound was the average cost of a commercial payload to geosynchronous earth orbit (GEO) by the year 2000 [1]. Thus, designing a system with a high performance-to-resource cost ratio, i.e., meeting system requirements with the smallest impact to mass and volume, is desirable for any spacecraft system.

The underlying assumption often made by systems engineers is that the thermal subsystem does not drive mission performance or significantly consume system resources. The result of this design process is that TCS design is traditionally performed *outside-the-loop* from design of the rest of the system. Furthermore, thermal design is typically *manual* and does not necessarily achieve a resource-optimal or performance-optimal state. In this context, a manual design is a suboptimal point design in the context of a largely predetermined system by an experienced

professional with high fidelity models to satisfy requirements. Consequently, thermal design of spacecraft systems typically takes a backseat to the design of other subsystems (e.g., payload and structures).

Several factors create important categorical exceptions to the assumption that TCS does not drive mission performance or consumption of resources. These factors include:

- A. Tightly coupled TCS performance to mission performance
- B. Significant physical tie between the thermal subsystem and other subsystems
- C. Systems with significant TCS challenges
- D. Highly resource-constrained systems

An explanation of each system factor is provided below, followed by a summary of the discussion.

Factor A – Systems with tightly coupled TCS performance to mission performance

There are components on spacecraft systems, such as detectors, where mission performance is directly impacted by thermal control. Better thermal performance can produce a significant improvement to data quality. For detectors, colder is often better. Optical systems, for example, have signal-to-noise ratios that are intimately tied to performance of the TCS. In this scenario, mission utility from the TCS perspective is not binary but a spectrum – thermal performance will impact well-defined mission performance levels. Components whose temperature profile drives mission performance require a performance-optimal TCS design.

Factor B – Systems with a significant physical tie between the thermal subsystem and other subsystems

Assigning ownership of components to one particular subsystem is often difficult – components may serve multiple functions across different subsystems. As a result, the TCS mass is understated for many systems – particularly those where there is a significant tie between the thermal and other subsystems. For example, a satellite bus structure receives design inputs from thermal analysis and also serves as a primary mechanism for heat transfer within a system.

Components may be structural as well as significant thermal paths. Figure 1 uses spacecraft historical data to show the average mass of a subsystem as a fraction of the total system dry mass. The spacecraft considered include diverse mission types including communications, the Global Positioning System, and science applications. While the thermal mass fraction in Figure 1 is relatively small, the thermal subsystem boundary lines are not always clear. Many elements of a spacecraft system's TCS design are part of another subsystem because they have dual functionality. Consequently, the 6% compositional thermal mass shown in Figure 1 can be a misleading representation of true thermal design mass. TCS design is interdisciplinary by nature and is relevant in reducing spacecraft system mass, a vital system resource.

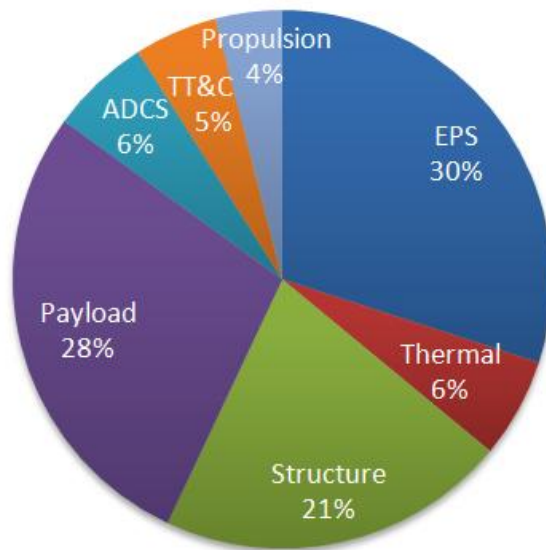


Figure 1: Dry mass distribution of average earth-orbiting spacecraft [2]

Factor C – Systems with significant TCS challenges

Systems with significant TCS challenges distinctly require more resources, typically mass, to achieve thermal requirements. One such distinction is cold regime space systems. These are systems, or a portion of a system, that must operate at a significantly colder temperature than their environment. Figure 2 shows two examples of cold regime spacecraft systems where the thermal subsystem mass fraction is higher than the average 6% shown in Figure 1.

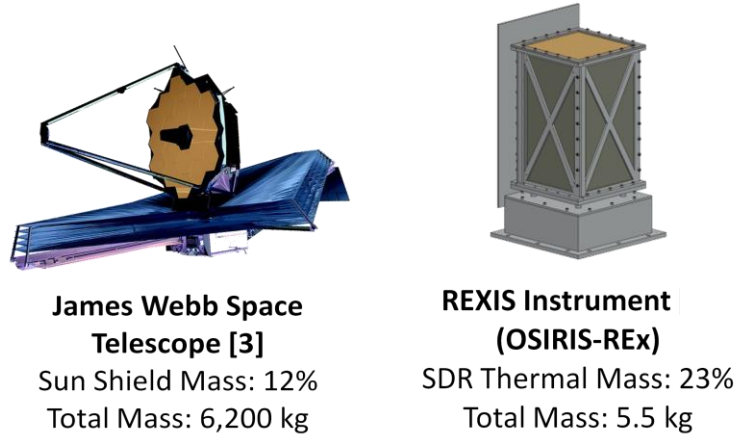


Figure 2: James Webb Space Telescope [3] and REXIS; examples of cold regime space systems with a higher than average thermal mass fraction

The first example in Figure 2 is the James Webb Space Telescope (JWST). JWST utilizes a large, deployable sun shield that allows the telescope assembly to operate at cryogenic temperatures. The sun shield, the primary TCS feature of JWST, challenges design with respect to both mass and volume. In addition to the remaining TCS mass, the sun shield is approximately 12% of the total system mass. Thus, the TCS mass of JWST is much greater than the 6% shown in Figure 1. Constrained by the launch vehicle fairing volume, the sun shield must be deployed into its operational configuration. The volumetric constraint on the JWST TCS design results in a significant increase to overall system complexity.

The second example in Figure 2, the REgolith X-ray Imaging Spectrometer (REXIS) instrument, is a small instrument on the instrument deck of the Origins-Spectral Interpretation-Resource Identification-Security-Regolith Explorer (OSIRIS-REx) spacecraft. The primary thermal challenge for REXIS is that the detectors, in a thermal path with the electronics box, need to operate below -55°C while the electronics box is approximately 30°C . The temperature differential results in a critical interface both thermally and structurally. REXIS is the primary case study for this thesis and a full instrument overview is provided in Chapter 2. The thermal subsystem mass is 23% of total system mass. Thus, both examples of the cold regime spacecraft systems, JWST and REXIS, have thermal designs that carry more mass than the average 6% in Figure 1. The TCS of spacecraft systems with significant thermal control challenges drives a disproportionate consumption of system resources, and therefore, design optimization yields

significant mass savings.

Factor D – Systems that are highly resource-constrained

Examples of resource-constrained systems include small satellites, Cubesats, and spacecraft payload instruments, such as REXIS. These systems are typically secondary launch vehicle payloads. Accordingly, these resource-constrained secondary payloads have a smaller allowable system mass, design envelope, and power requirements. While design optimization offers improvements to a system's performance-to-resource cost ratio over manual design methods, it may not always be cost- or schedule-effective to do so on larger missions where the expected gain is small – this is the traditional notion with primary payload thermal design: that TCS typically does not drive system resources and thus, does not warrant design optimization. On highly-resource constrained spacecraft systems such as REXIS, however, even small benefits to the systems performance-to-resource cost ratio are useful. For example, the not-to-exceed mass of REXIS is 5.5 kg. At this low mass, the REXIS mass margin is highly sensitive to design changes so that even small improvements to a TCS design with respect to mass are important. Commensurately, thermal design optimization is crucial to effectively allocating precious system resources in highly resource-constrained spacecraft systems.

Summary

The high cost of spaceflight necessitates a system design with a high performance-to-resource cost ratio, i.e., meeting system requirements with the smallest impact to mass and volume. Thermal design optimization is key in reducing a spacecraft system's reliance on system resources to achieve required performance levels. In particular, manual point design from an experienced professional is insufficient to optimize the TCS. In these cases, performance should be evaluated against resource consumption, (e.g., mass and volume) for different TCS designs in a Pareto-sense.

Research toward obtaining resource- or performance-optimal TCS design in spacecraft lags relative to the other subsystems due to the traditional notion that thermal subsystems do not drive

system resource consumption. Current research focuses heavily on component-level design optimization where the components are designed in isolation from the rest of the system. However, component-level optimization does not guarantee an optimal system design. This thesis aims to develop a methodology for the design optimization of thermal systems such that the performance-to-resource cost ratio for spacecraft systems is maximized.

1.2 Literature Review

To demonstrate how this thesis will relate with previous research, Figure 3 displays a spectrum, or progression, of design optimization from component-level to a complete thermal path view. Current research has primarily focused on component-level optimization. Figure 3 pictorially shows that research literature is sparse in generalizing the optimization of a complete thermal path. Categorical distinctions have been made in this thesis between component-level [4] [5] [6] [7] [8], partial [9] [10] [11], limited [12] [13], and complete thermal path representations. These categories are discussed below and are illustrated by Table 1. To illustrate the spectrum of thermal path optimization more clearly, a few examples of each category are examined in detail.

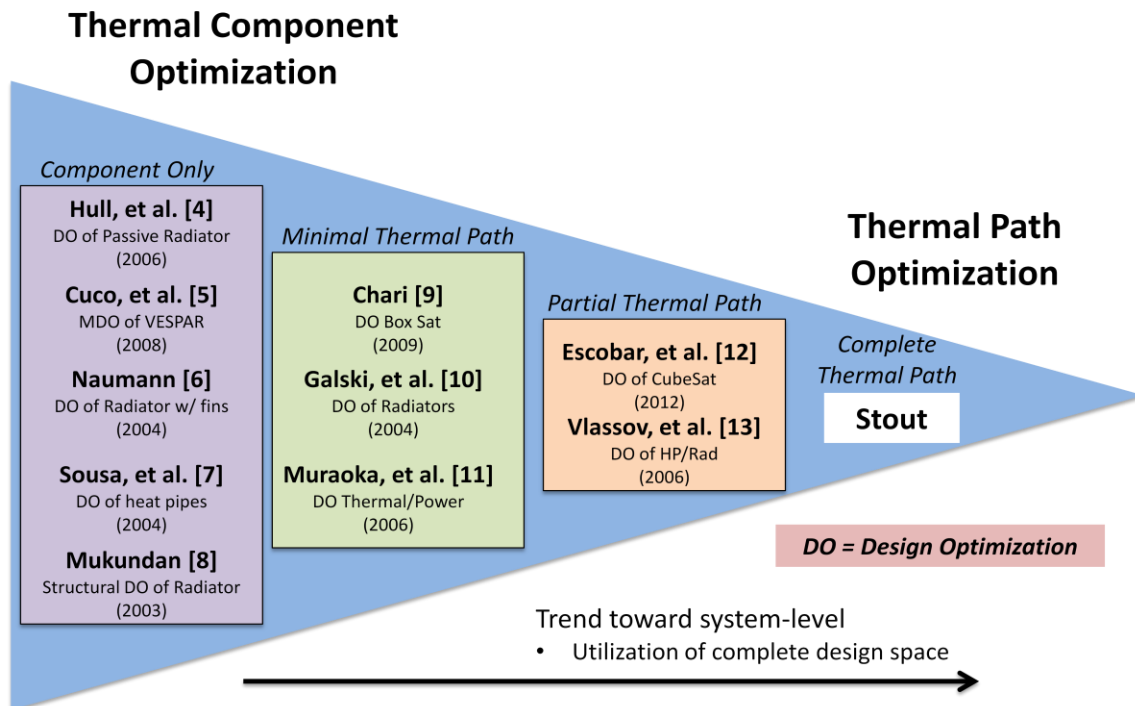


Figure 3: Relationship of thesis work with prior research

Table 1 shows the distinctions between categories made along the spectrum of research

presented in Figure 3. Each category builds on the previous in terms of complete thermal path representation. Component-level optimization considers the component itself in isolation from the rest of the system. Boundary conditions are applied to capture the effect of other parts of the system. Partial thermal path representation is the design of multiple components simultaneously. Building on the partial representation, a limited thermal path design in this context is the design of multiple components simultaneously while considering the physical and functional interactions between components. The aim of this thesis is to present an approach for the collective optimization of an entire thermal path, which considers not only interactions between the components but interactions between the components and the spacecraft system as a whole.

Table 1: Enumeration of what constitutes a complete thermal path

Thermal Path	Individual Component Design	Multiple Component Design	Component Interaction	Interaction with spacecraft
Component-level	x			
Partial	x	x		
Limited	x	x	x	
Complete	x	x	x	x

As the left side of Figure 3 illustrates, Hull, et al. [4] is representative of component-level design optimization. By allowing the upper edge of a passive space radiator to vary, the mass-to-performance ratio, specifically the radiator mass to heat rejection ratio, was minimized. Figure 4 shows graphically the process by which Hull, et al. [4] specified the upper boundary of the radiator and selected a final design. The fundamental limitation of component-level design optimizations like Hull, et al. [4] is that the component is designed in complete isolation from the rest of the system. This isolative design restricts the design space considered by the optimizer. Figure 4 illustrates the temperature point boundary condition applied to achieve the solution radiator, in this case. This thesis will draw from these component optimization techniques when comparing component-level optimization to the collective optimization of thermal paths.

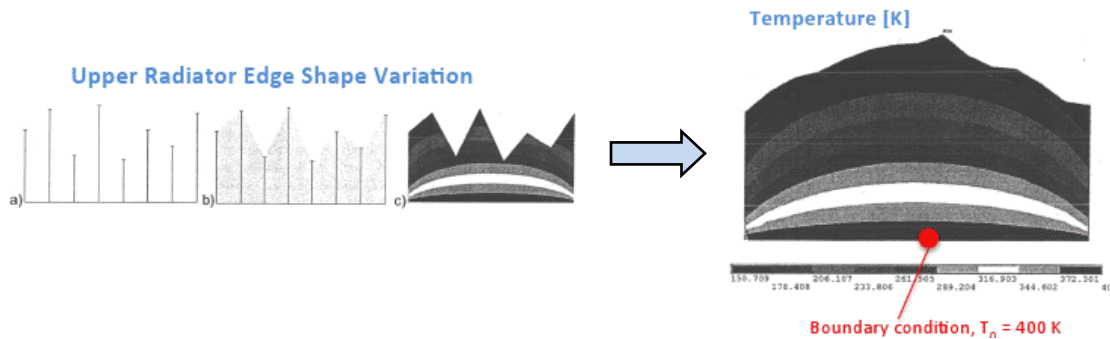


Figure 4: Hull, et al. [4] radiator shape variation and design optimization

Moving to the right in Figure 3, Muraoka, et al. [11] is a good example of partial thermal path representation. As shown by Figure 5, Muraoka, et al. [11] sought to optimize the configuration of radiators and absorbers on external panels of a multi-mission platform, i.e., a generic representation of a satellite. The multi-mission platform is shown with the design solution radiators, absorbers, and MLI blankets distributed over the external panels – each panel represents a different component in the design. The end-goal was to achieve a recipe for a rapid thermal design based on different mission scenarios. The objective function used by Muraoka, et al. [11] contained two terms for minimization: a heater consumption term and a differential of actual predicted temperature versus desired temperatures. While partial thermal path optimizations like Muraoka, et al. [11] perform the design optimization of multiple components simultaneously, the fundamental limitations are that they only capture a limited view of component interaction. Additionally, they do not capture heat transport within the system – only a system-level balance of heat flow is performed. This thesis will draw from partial thermal path representations to ensure the heat budget is satisfied for the thermal path of interest.

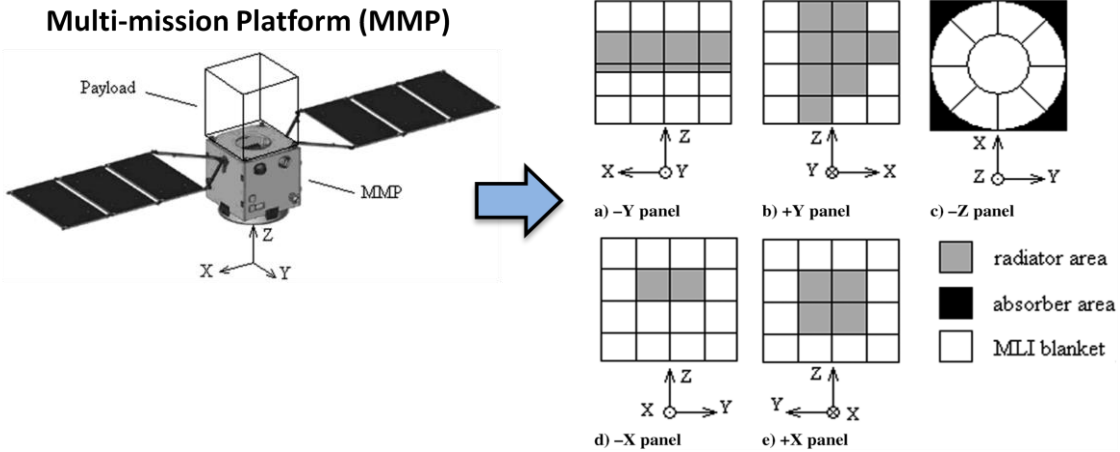


Figure 5: Muraoka, et al. [11] design optimization of MMP panels

Moving even further right toward collective design optimization in Figure 3, limited thermal path design optimization is a category that closer approximates the complete thermal path representation and is exemplified by Vlassov, et al. [13]. In this example, Vlassov, et al. [13] examined a heat pipe and radiator assembly (geometry is shown in Figure 6). The objective was to minimize mass subject to mechanical and structural constraints. Although Vlassov, et al. [13] models the important interactions between thermal control components, its limitation is that the interaction of the assembly with the spacecraft system is not captured. The interaction with the spacecraft system is a critical component of any thermal path design and is the primary distinguishing feature between limited thermal path and complete thermal path representation. Example interactions include, but are not limited to, the view factor to other parts of the system, mechanical configurations of the thermal path within the system, and conductive parasitic heat loads.

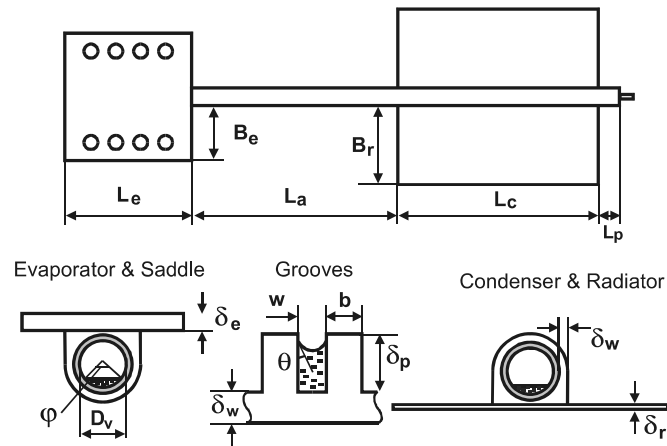


Figure 6: Vlassov, et al. [13] heat pipe and radiator assembly geometry from for design optimization

1.3 Traditional Thermal Design Process

The approach introduced in this thesis seeks to improve the thermal design process. Thus, it is relevant to review the traditional thermal design process [14] followed by most spaceflight programs. Figure 7 shows this four-step process. The overview of the traditional thermal design process will provide context to the approach introduced into the parametric modeling and design method included in Chapter 3.

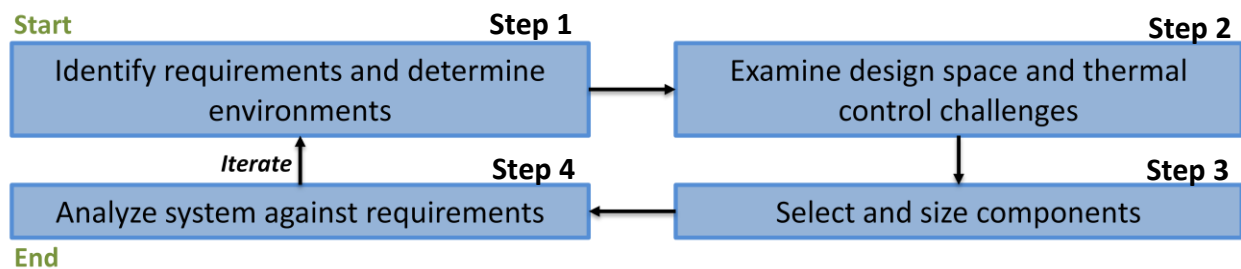


Figure 7: Traditional thermal design process [14]




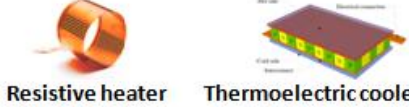


The first step is to identify requirements and determine relevant thermal environments. The key is to document driving system requirements, stated in terms of operational and non-operational temperature ranges, to understand how component temperatures must be maintained.

A relevant thermal environment refers to all thermally-bounding environments during ground operations, launch, and spaceflight through which the system must survive and operate.

The second step in the traditional TCS design process is to examine the design space and thermal control challenges. Depending on the size and complexity of the thermal control problem, the design space can range from the size and shape of a radiator to the spatial configurations and material property choices of many thermal control components both inside the spacecraft and on the periphery. Output from this step includes an understanding of the requirements in the context of the system and the mission environment, where thermal control components can exist within a system, and the mass, power and volume constraints on the design.

An inherent drawback to the process shown in the traditional thermal design process shown in Figure 7 is Step 3: selecting and sizing the thermal control components. This third step represents a significant majority of the design efforts. Experts make these critical decisions based on predicted performance approximated through modeling and a wealth of experience that captures not only modes of operation for the thermal component but the system-level impacts (e.g., outgassing or distortion). Table 2 provides a snapshot of the variety of components available to the thermal engineer. The columns divide TCS components by the active and passive operational mode categories. The rows provide additional distinctions between TCS components that are used to isolate parts of the system, transport heat within the system, and radiate heat away from the system. In general, passive methods of thermal control are preferred due to their simplicity and heritage. Large spacecraft systems will typically have at least one TCS component from each row.

Table 2: Example spacecraft thermal control components

Thermal Control Components	Passive Control	Active Control
Isolation	 <p>MLI G10</p>	 <p>Electrochromics</p>
Heat transport	 <p>Heat pipe Thermal Strap</p>	 <p>Resistive heater Thermoelectric cooler (TEC)</p>
Radiators	 <p>Structural radiator Body-mounted</p>	 <p>Louver Fluid loop</p>

The fourth and final step is to create an analytical model of the system and analyze the design against the requirements. If unsatisfactory performance is predicted, design ramifications can vary from small resizing efforts to a complete system redesign. Consequently, the process outlined in Figure 7 iterates until a satisfactory design is achieved.

1.4 Research Hypothesis and Objective

This thesis hypothesizes that collective design optimization of a thermal path offers mass savings or performance gains over the traditional component-level optimization techniques. Capturing the component interactions increases the design space and is the fundamental reason for the mass and performance improvements.

The objective of this research is to obtain the mass- or performance-optimal thermal path by collectively optimizing component geometries and configurations using parametric modeling tools while evaluating against critical Figures of Merit (FOMs). Chapter 5 considers a mass minimization of a thermal strap and radiator assembly subject to a detector operating temperature thermal constraint.

Traditionally, thermal systems are not thought to drive spacecraft system resource consumption. Consequently, previous research has focused on the optimization of individual components. Furthermore, the thermal design process is such that as a design progresses throughout the project lifecycle, experts are needed to make important component selection and

sizing decisions. However, the design optimization of thermal components individually does not guarantee a mass- or performance-optimal thermal path design. Figure 8 notionally depicts this concept. The left-hand side shows component-level optimization and the right-hand side shows a collective optimization of a complete thermal path. On the left, the hashed box indicates that the heat transport devices and radiators (i.e., heat rejection devices) have been optimized individually. That is, separate models utilized boundary conditions to evaluate the performance of candidate designs. On the right, the hashed box indicates that the heat transport devices and the radiators have design optimized within a single model. In this case, the interaction between the components is captured both functionally and spatially.

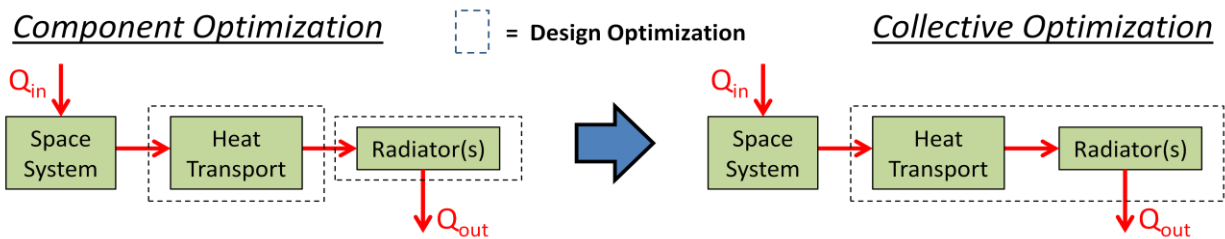


Figure 8: Notional illustration of component-level and collective optimization of thermal paths

1.5 Thesis Roadmap

This thesis is organized into three parts: (1) the background material in Chapter 2, (2) the thesis methodology for the collective thermal design optimization process presented in Chapter 3, and (3) the implementation of the methodology in Chapters 4 and 5. Figure 9 shows the thesis roadmap where the thesis methodology, preliminary design, and case study form the basis of content presented in Chapters 3-5, respectively. The preliminary design, thermal modeling, and the case study are inspired by the REXIS instrument. An overview of REXIS is provided in Chapter 2 since the instrument is a consistent thread throughout this thesis. The background material in Chapter 2 introduces the REXIS project and discusses requisite thermal engineering physics.

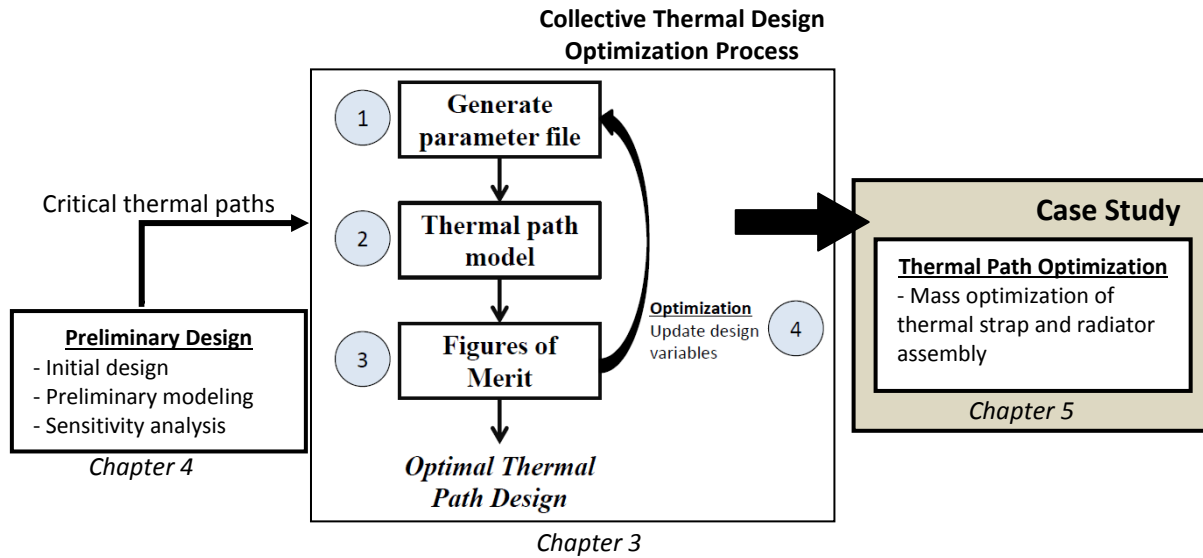


Figure 9: Thesis roadmap

Chapter 3 details the collective thermal path optimization approach and provides a high-level survey of optimization techniques. Each step of the design optimization process is explained in Chapter 3 using a simple 1-D conduction example with two components within the thermal path. A survey of optimization techniques is provided because selection of the algorithm directly controls how design variables are updated and candidate solutions are evaluated. The motivation of Chapter 3 is to provide the reader with the requisite knowledge needed to properly implement the collective thermal design optimization methodology.

Chapters 4 and 5 are the implementation of the collective optimization approach to the REXIS instrument. Recognizing that a preliminary understanding of the TCS requirements and design concepts are required to implement the Chapter 3 methodology, Chapter 4 demonstrates the necessary steps of thermal design and modeling that must be completed prior to the implementation of the collective optimization approach. These steps in Chapter 4 map to the first box presented in Figure 9. Here, an understanding of the driving thermal requirements on REXIS is presented. A preliminary design is established and modeled. Finally, verification of the model is completed via model-model correlation with a REXIS thermal model constructed with industry-standard software. As shown in Figure 9, an output of Chapter 4 is a fundamental understanding of the critical thermal paths of REXIS and what components/interfaces should be

design optimized. Understanding of the critical thermal paths is achieved via sensitivity analysis to the driving requirements and examination of the REXIS thermal mass budget.

Chapter 5 implements the collective optimization approach on the REXIS critical thermal path: the thermal strap and radiator assembly. This thermal path serves as a case study for the methodology introduced in Chapter 3. The mass of the thermal strap and radiator drives the overall REXIS TCS mass and passively cools the detectors on the instrument. Thus, it is a performance- and mass-critical thermal path. A mass-optimal thermal path is achieved subject to a thermal performance constraint using a parametric thermal model to evaluate candidate thermal path designs.

Chapter 6 will summarize the findings of this thesis and draw conclusions based on the results and analyses of Chapters 4 and 5. Finally, contributions will be reviewed and future work documented. The appendices to this thesis contain all code used for analysis and additional documentation of the REXIS thermal design. In particular, Appendix E contains higher fidelity thermal modeling documentation that was presented at the REXIS instrument Preliminary Design Review.

Chapter 2 – Background

2.1 REXIS Instrument Overview

The primary focus of this section is to provide the reader with background material regarding the REXIS mission. In addition to the instrument science objectives, the instrument mechanical design is presented. The architecture and design information serve as inputs to the preliminary modeling and analysis performed in Chapter 4.

2.1.1 OSIRIS-REx and REXIS Project Overview

The OSIRIS-REx mission is the third planetary science mission selected for development in NASA's New Frontiers Program. Launching in September 2016, the spacecraft will encounter the organic-rich asteroid Bennu in October 2018. Study of Bennu will occur for up to 505 days, globally mapping the surface from a distance of 5 km to a distance of 0.7 km. The mission seeks to help scientists learn about the formation and evolution of our solar system because the asteroid's surface is primitive, undergoing very little geological change over time. To do so, OSIRIS-REx will return at least 60 g of pristine, uncontaminated, organic-rich regolith for analysis on Earth. In addition to the science return, study of the asteroid and its regolith will advance: [15]

- Refining position estimates of the asteroid which currently has a 1:1800 probability of impacting the Earth in 2180
- Study of the Yarkovsky effect: thermal forces that cause small objects to deviate from Keplerian orbits, with the goal of understanding how to mitigate against a civilization-ending or species-ending impact catastrophe.
- Provide "ground truth" for telescope observations of airless bodies by returning a pristine sample of the surface of RQ36.
- Proximity operations and learning how to mitigate impact catastrophes
- Evaluation of resources available for future human missions, including materials and technologies

Two years of funded studies are carried out by the U.S. and world community before end of mission in 2025, after which samples will still be available through the NASA Johnson Space

Center Curation Facility. [15]

The REXIS instrument is a student project and a collaboration between MIT Space Systems Laboratory (SSL), MIT Kavli Institute for Astrophysics and Space Research, and Harvard College Observatory (HCO). REXIS will fly on the instrument deck of the OSIRIS-REx spacecraft on its interplanetary mission to the asteroid Bennu set for launch in 2016. REXIS is shown near the edge instrument deck of OSIRIS-REx in Figure 10. REXIS operates at much cooler temperatures relative to other systems on the instrument deck. The proximity to edge provides the REXIS radiator with the necessary view factors to deep space for heat rejection. The design envelope is 20 x 20 x 40 cm where the 40 cm dimension is in the +Z direction and along the REXIS telescope axis. The placement of REXIS on the instrument deck with the telescope axis aligned with +Z (shown in Figure 10) is necessary because the instrument deck is nadir-pointed at the asteroid to take measurements of its surface during the REXIS science mission.

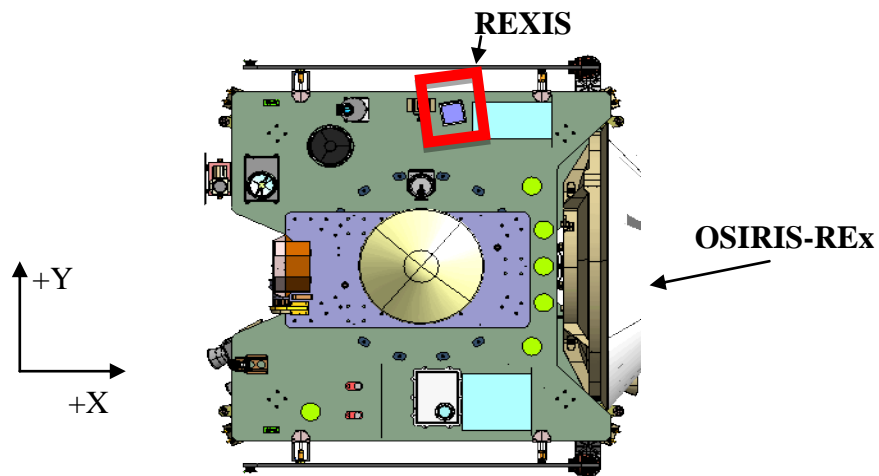


Figure 10: Top view of REXIS on the instrument deck of OSIRIS-REx

2.1.2 REXIS Science Mission

REXIS contributes to the OSIRIS-REx mission by generating two science products. First, REXIS will characterize the asteroid Bennu among the major subgroups by globally measuring elemental abundances in spectral mode. The elemental ratios Mg/Si, Fe/Si, and S/Si will be measured to within 20% accuracy integrated over the entire asteroid surface. Second, REXIS will generate a spatial elemental abundance map of the asteroid. REXIS will identify the

distribution of elements on the asteroid Bennu with a spatial resolution of 50 meters or better. The elements Mg and Fe will be mapped with a signal-to-noise ratio of greater than five. REXIS will achieve the first coded-aperture, wide field imaging for fluorescent line composition mapping of an asteroid. REXIS science data can provide context to the sample site selection process to ensure the sample collected is representative of the entire asteroid surface.

REXIS uses charged-coupled devices (CCDs) to characterize the surface of asteroid Bennu. The CCD-based coded aperture soft X-ray (0.5-7.5keV) telescope performs remote X-ray Fluorescence (XRF) spectrometry. X-rays emitted from the sun are absorbed by elements on the surface of the asteroid and are re-emitted, or fluoresced, at energy levels corresponding to the element type. The re-emitted light passes through the coded aperture of REXIS and is incident on the CCDs. Additionally, a solar X-ray monitor (SXM) is used to monitor solar activity during instrument observation of the asteroid to provide context for each measurement.

In addition, REXIS uses coded aperture imaging to generate a spatial abundance map of the asteroid. REXIS collects fluorescent X-rays through a coded-aperture mask that is composed of randomly populated pinholes. The mask casts a shadow pattern on the detectors and encodes the direction of the incoming photons. The raw instrument data are decoded by cross-correlation of the data collected by the instrument and the mask pattern. Using the spatial encoding information provided by the mask, REXIS will generate a list of X-ray events and 2-D locations on the asteroid for the most likely point of origin for each event. Without this mask, REXIS could not produce a map of the asteroid and would only generate a global X-ray spectrum of the asteroid.

2.1.3 Design Overview

REXIS has three major mechanical subassemblies: (1) the electronics box, (2) the telescope truss structure, and (3) the SXM. The electronics box and telescope truss structure subassemblies are connected and collocated on the instrument deck, while the SXM is stationed at another location on the spacecraft for good viewing angles to the sun during REXIS operation. Because this thesis focuses on the instrument deck subassemblies, the design overview focuses on the electronics box and telescope truss structure. The two instrument deck subassemblies are connected via the thermal isolation layer (TIL). The TIL drives the large temperature differential between the electronics box and telescope truss structure necessary for the proper operation of

both the electronics and the detectors. Mechanically, the TIL consists of five, low thermal conductivity standoffs and multi-layer insulation (MLI) to isolate the telescope truss structure in both conduction and radiation. The net effect of the TIL is that the electronics box is warm and the telescope truss structure is cold. Figure 11 shows the computer-aided design representation of the current REXIS design. The overall instrument footprint of the electronics box at the mechanical interface with the spacecraft is approximately 15 x 15 cm. Excluding the radiator and coded aperture mask, the external surfaces of REXIS in its flight configuration will be covered with MLI.

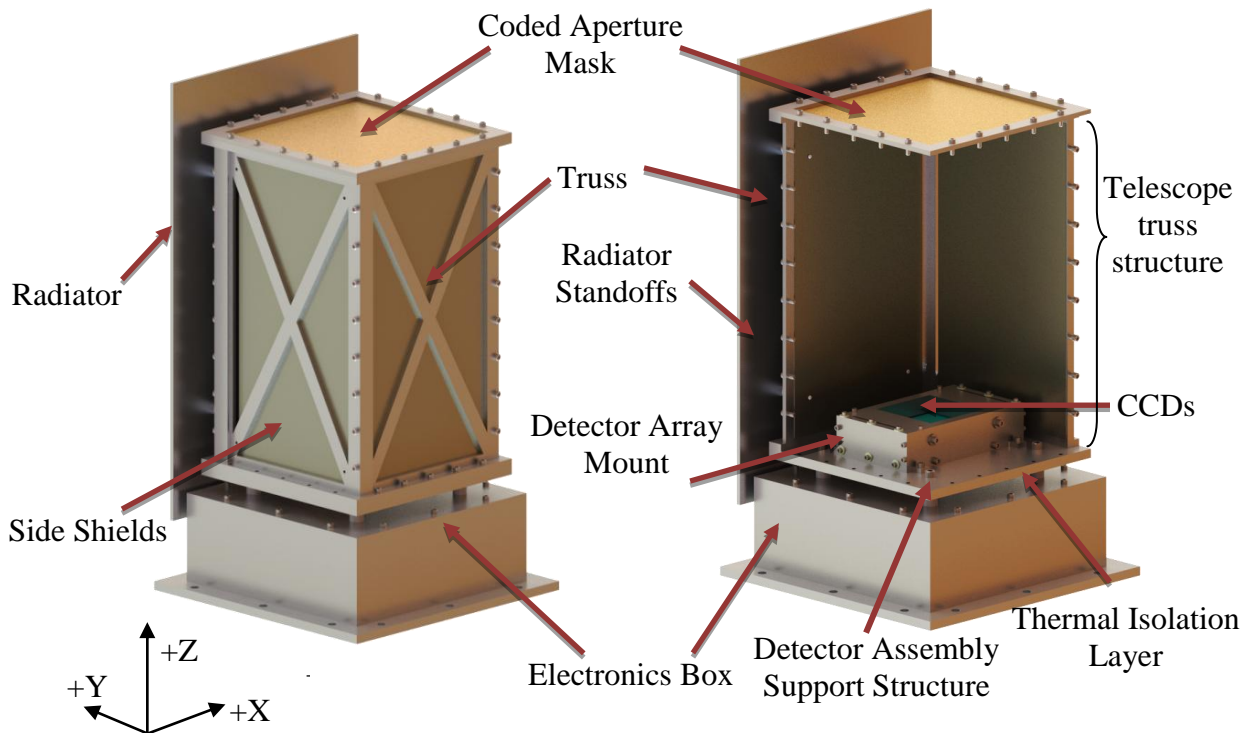


Figure 11: REXIS design overview

The electronics box is a six-sided aluminum box that supports the trays that hold the electronics. There are three printed circuit boards (PCBs) within the electronics box: two detector electronics (DE) boards and the main electronics board (MEB). The DEs drive the CCDs and convert the analog CCD signal to a digital output. The MEB performs all REXIS housekeeping functions, on-board image processing, and power regulation. A Virtex-5 field-programmable gate array (FPGA) on the MEB performs all REXIS command and data handling. Furthermore,

the MEB also contains the SXM electronics. All three PCBs rest on aluminum trays that are mounted to the four side walls of the electronics box via fasteners.

The telescope truss structure consists of a detector assembly support structure (DASS), the detector assembly mount (DAM), a truss structure to support the coded aperture mask and radiator, radiation door cover mechanism, and thermal strap. The DAM mechanically and structurally supports the CCDs and shields the CCDs from radiation on the multi-year interplanetary mission. The thermal strap (not depicted in Figure 11), is mounted to the DASS and the radiator to passively cool the telescope. The radiation door cover (not pictured in Figure 11) protects the CCDs from a total ionizing dose (TID) of radiation during the multi-year cruise phase to the asteroid. Prior to REXIS operation, a Frangibolt actuator mechanism releases the spring loaded door cover to expose the detectors. Finally, the coded aperture mask is a thin sheet of stainless steel with gold electroplate. X-ray fluorescence traveling perpendicular to the mask (+Z direction) casts a random shadow pattern on the CCDs. This shadow enables spatial variations in elemental abundances to be resolved through analysis.

To summarize the physical and functional design of REXIS, an N^2 diagram is provided in Appendix A of the current REXIS design. N^2 diagrams are powerful tools in analyzing functional linkages within and between subsystems. A reduced version of the N^2 diagram is used in Chapter 4 as the framework for the system-level thermal model. The functional blueprint of the thermal system model is realized by isolating only thermal connections in the N^2 diagram.

2.2 Thermal Modeling

This section provides a sufficient thermal engineering physics background for the technical reader to understand the basic thermal modeling framework presented. First, the general heat transfer equation for all spacecraft systems is presented. Then, the space thermal environment is discussed to form the basis of source terms in the general heat transfer equation. The primary modes of heat transfer in space, conduction and radiation, are explained, followed by a description of the resistor network modeling framework used in Chapter 5. Readers seeking supplementary material for thermal engineering physics should see [16].

2.2.1 General Heat Transfer Equation

The general heat transfer equation governing the temperature of a body in space is given

by the partial differential equation in Equation 2.1 [16]. The general heat transfer equation is valid for a stationary, heterogenous, anisotropic solid.

$$\rho C_p \frac{\partial T}{\partial t} = \nabla \cdot (K \cdot \nabla T) + Q(T, t) \quad (2.1)$$

In Equation 2.1, ρ is the density of the materials used in the system, C_p is the specific heat, t is time, K is the conductivity tensor, and $Q(T,t)$ is the source term. Temperature, $T(x,y,z,t)$, is a function of position within the material and time. The source term captures the heat entering and leaving the system. For a spacecraft system, the external sources are mostly heat loads from the sun and nearby planetary bodies – these are discussed in the next section. The heat leaving the spacecraft system is equivalent to the heat leaving the radiator(s). The net heat load and the efficiency with which heat is transferred, specified by K , dictates the temperature profile of the system. K captures conduction within the system and is a design variable in TCS design. Solving the general heat transfer equation for a spacecraft system is the objective of all thermal analysis tools.

2.2.2 General Thermal Environment

Most spacecraft systems operate in a general space environment as shown in Figure 12 [14]. The environment shown in Figure 12 yields three external heat input terms: (1) direct solar, (2) albedo and (3) re-emitted radiation, i.e., infrared radiation from the nearby planetary body. These three external heat input terms, in addition to the internal power dissipation of the spacecraft system, sum to the total amount of heat the spacecraft must reject. These four terms are captured by the source term, $Q(T,t)$, in Equation 2.1.

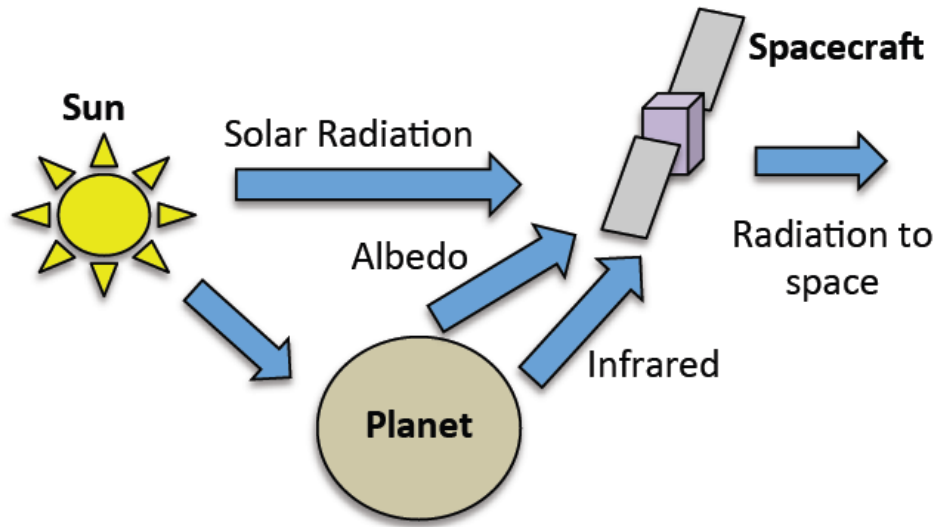


Figure 12: General spacecraft system thermal environment [14]

The total spacecraft system heat load is given by $Q(T,t) = Q_{total}$ in Equation 2.2.

$$Q_{total} = Q_{solar} + Q_{IR} + Q_{albedo} + Q_{int} \quad (2.2)$$

In Equation 2.2, Q_{int} is the internal heat dissipation of components with stored energy such as batteries. Q_{solar} , Q_{IR} , and Q_{albedo} are the environmental source terms from direct sunlight and the nearby planetary bodies, as shown in Figure 12.

Direct solar radiation is solar flux directly incident on the spacecraft system and is defined by Equation 2.3.

$$Q_{solar} = \frac{\alpha A_{inc} G_s}{R_{\odot}^2} \cos \theta \quad (2.3)$$

In Equation 2.3, α is the dimensionless absorptivity of the incident surface, A_{inc} is the total area of the incident surface, θ is the angle between the incident surface normal and the incoming

sunlight, G_s is the solar flux at 1 AU (equal to $1,367 \text{ W/m}^2$, on average), and R_O is the heliocentric radius of the spacecraft in its orbit [16]. In TCS design, the α and A_{inc} terms regulate the amount of heat entering the system directly from the sun. Typically, designers seek to reduce Q_{solar} by covering the sun-facing side of a spacecraft system with low α material, such as white paint or MLI.

Albedo radiation is heat that has reflected from the nearby planetary body, such as Earth, and is incident on the spacecraft system. The system input heat from albedo effects is proportional to the albedo constant, ρ , and the view factor, F , as given by Equation 2.4 [17].

$$Q_{albedo} = \rho F Q_{solar} \quad (2.4)$$

The third and final major heat source on spacecraft systems is the infrared component. To capture the external heat flux incident on the spacecraft system, measurements or calculations of the nearby planet's effective infrared temperature are required [14]. An earth-orbiting spacecraft, for example, does not experience a uniform heat flux in the infrared spectrum as it traverses its orbit because Earth's effective temperature varies both spatially and temporally. However, a simplifying assumption is often made that the planetary body is of constant temperature in the infrared spectrum. Under this assumption, the heat input from the planet is governed by the Stefan-Boltzmann Equation introduced later in this section. Assuming the planet's radiation is isotropic, let Q_{planet} be the total heat flux of a planetary body originating from a point source located at the planet's origin. Then, the total heat incident on a spacecraft system is given by Q_{IR} in Equation 2.5.

$$Q_{IR} = Q_{planet} \frac{r_{planet}^2}{r_{orbit}^2} A_{inc} \quad (2.5)$$

In Equation 2.5, r_{planet} is the equivalent spherical radius of the planetary body and r_{orbit} is the radius of the orbit (assumed circular). Intuitively, as the spacecraft radius becomes larger, the Q_{IR}

decreases. Equations 2.3-5 form the basis of the external heat inputs to a spacecraft system in the general space environment as defined by Figure 12 and Equation 2.2.

2.2.3 Methods of Heat Transfer

The following sections discuss the heat transfer mechanisms of conduction and radiation within a spacecraft system. Conduction, governed by the $\nabla \cdot (K \cdot \nabla T)$ term, and radiation, captured by the $Q(T,t)$ term, form the basis of heat transfer mechanisms that occur *within* the system for Equation 2.1. In space, there is no free convection because there is no atmosphere, i.e., a fluid medium through which heat transfer can occur. There are applications of convection in space such as forced convection through a heat loop pipe or free convection that occurs on manned flight when an atmosphere must be created to support human life. These examples are outside the scope of this thesis, so the physics of convection are not addressed.

2.2.3.1 Conduction

Conduction is the flow of heat, or energy, from a high temperature body to a low temperature body. In 1-D where the body is homogeneous and isotropic, conduction is governed by the Fourier's Law, shown in Equation 2.6.

$$Q_{cond} = -kA_c \frac{dT}{dx} \quad (2.6)$$

In Equation 2.6, Q_{cond} is the heat transferred via conduction, k is the conductivity of the material, A_c is the cross-sectional area of the material perpendicular to the heat flow, and $\frac{dT}{dx}$ is the spatial temperature gradient across the material. If the two endpoints of the 1-D problem are at constant temperatures, the equation becomes the discrete analog of Fourier's Law as shown in Equation 2.7. In the discrete case, $\Delta T = T_1 - T_2$.

$$Q_{cond} = (T_1 - T_2) \frac{kA}{\Delta x} \quad (2.7)$$

Figure 13 shows a diagram of the discrete 1-D conduction equation which can be used to relate the temperatures between two objects connected by a uniform material. The temperature profile through a material conducting in 1-D is linear. There is a direct analogy between the discrete heat conduction equation and Ohm's law for electrical circuits. In practice, finite differencing codes use nodes, isothermal subspaces whose properties are constant, connected via 1-D conductance resistors on a 3-D mesh to approximate the solution to the general heat transfer equation [16].

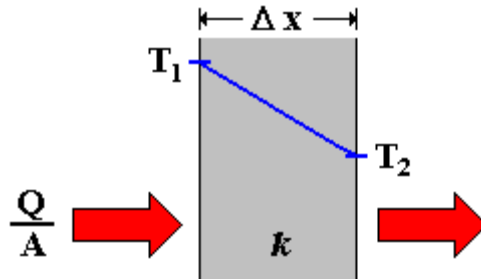


Figure 13: 1-D conduction through a homogenous material [18]

2.2.3.2 Radiation

Radiation is the primary method of heat transfer in space [17]. The Stefan-Boltzmann Equation [14], Equation 2.8, gives the amount of heat, Q_{rad} , leaving a surface of a temperature T to an external body with temperature T_{ext} .

$$Q_{rad} = \sigma \epsilon A F (T^4 - T_{ext}^4) \quad (2.8)$$

In Equation 2.8, σ is the Stefan-Boltzmann constant ($5.67 \times 10^{-8} \text{ W/m}^2/\text{K}^4$), ϵ is the emissivity of the radiating surface, A is the surface area, and F is the view factor to the external body. A view factor is a dimensionless expression, ranging from 0 to 1, representing the amount of radiation leaving one surface incident on another. The Stefan-Boltzmann Equation reveals that spacecraft system radiators perform better (i.e., reject more heat) at higher temperatures and with larger radiator surface areas.

2.2.4 Resistor Network Model

The general solution to the heat transfer equation shown in Equation 2.1 is spatial and temporal temperature distribution, $T(x,y,z,t)$, for the TCS. This problem is inherently nonlinear for objects in space due to the effects of radiation – which is a function of temperature to the fourth power, as shown by Equation 2.8. There are circumstances, however, where the problem can be linearized and an analogy between the TCS and a network of resistors is made. This thesis utilizes linear and nonlinear methods to solve the heat transfer equation. This section describes cases where the resistor analogy can be made and a linear system can be used to create a model of the heat transfer. Methods to the solution of the nonlinear heat transfer problem are well documented; Travis Smith’s Master’s thesis [19] is a good example of the method used in this thesis to model the system applied to the small satellite PANSAT. See Chapter 4 and Appendix B for the development of a nonlinear thermal model.

The resistor network analogy is an interdisciplinary relationship between Ohm’s Law in electrical circuits and other fields [17]. Table 3 shows the analogy between Ohm’s Law for circuits compared to heat transfer and forces and displacements in struts for 1-D flow. For 1-D flow, temperature is linearly dependent on the flow variable, Q , through the thermal resistance in conductive heat flow – a restatement of Fourier’s Law in 1-D (Equation 2.6).

Table 3: Resistor network analogy for multiple engineering disciplines for 1-D flow

Properties	Electrical	Heat Transfer	Forces/Displacements
Potential	V (Volt)	ΔT (K)	u (m)
Flow Variable	I (Amp)	Q (W)	F (N)
Resistance	R (Ohm)	$R = \Delta x/kA$ (K/W)	$R = L_0/EA_c$ (m/N)
Equation	$V = IR$	$\Delta T = QR$	$u = RF$

The analysis strategy is to physically represent a system as a network of 1-D resistors. The resistors are connected at nodes where the temperature is calculated. Heat, Q , flows between the nodes through the resistors. Boundary conditions are applied at the nodes in the form of

temperatures, which are analogous to voltage sources, and heat flows, which are analogous to current sources. Once the geometry and boundary conditions for the problem are set, Kirchhoff's Current Law (KCL) is written for each node. Equation 2.9 shows the KCL process for each node in the model.

$$I_Q + \sum_i Q_i = I_Q + \sum_i \frac{\Delta T_i}{R_i} = 0 \text{ for each node} \quad (2.9)$$

In Equation 2.9, I_Q is the net effect of the current sources on the node, and Q_i is the heat flowing to/from the node through the i^{th} resistor. Equation 2.9 is linear in T_i for each node, assuming I_Q is either constant or also linear in T_i . If linear, the problem can be written in the matrix form $Ax = b$. Matrix A is the nodal matrix containing the conductance values for the system, which are representations of the system's material properties and geometries. The right-hand side, vector b , is the list of heat flows, analogous to current sources, for the system. In the simple example of a 1-D string of resistors whose first and last nodes are held fixed at a constant potential, b is a vector of zeros. Finally, the solution vector x contains the temperature of each node.

The purpose of this section is not to rigorously introduce how to implement the resistor network methodology but instead how to solve practical heat transfer problems using these tools. Thus, a radiator plate example solved to provide context to the resistor network approach. Furthermore, the model developed is a candidate for the thermal model of the radiator in the Chapter 5 case study of the critical REXIS thermal path.

2.2.4.1 Resistor Network Analysis of Radiator Plate

Consider a flat rectangular plate made of a homogeneous material, such as aluminum, given by width, w , height, h , and thickness, t , as shown in Figure 14. Assume that the plate's thickness is sufficiently small so that heat transfer from its front to back surfaces is negligible – that is, the plate is isothermal in the z -direction. Figure 14 also shows the general case of discretizing a radiating plate into nodes where each node conducts to its neighbors and radiates to space. For this problem, the resistor analogy is a 2-D resistor grid model illustrated in Figure 14 with an example discretization of 100 nodes in the x -direction and 10 nodes in the y -direction.

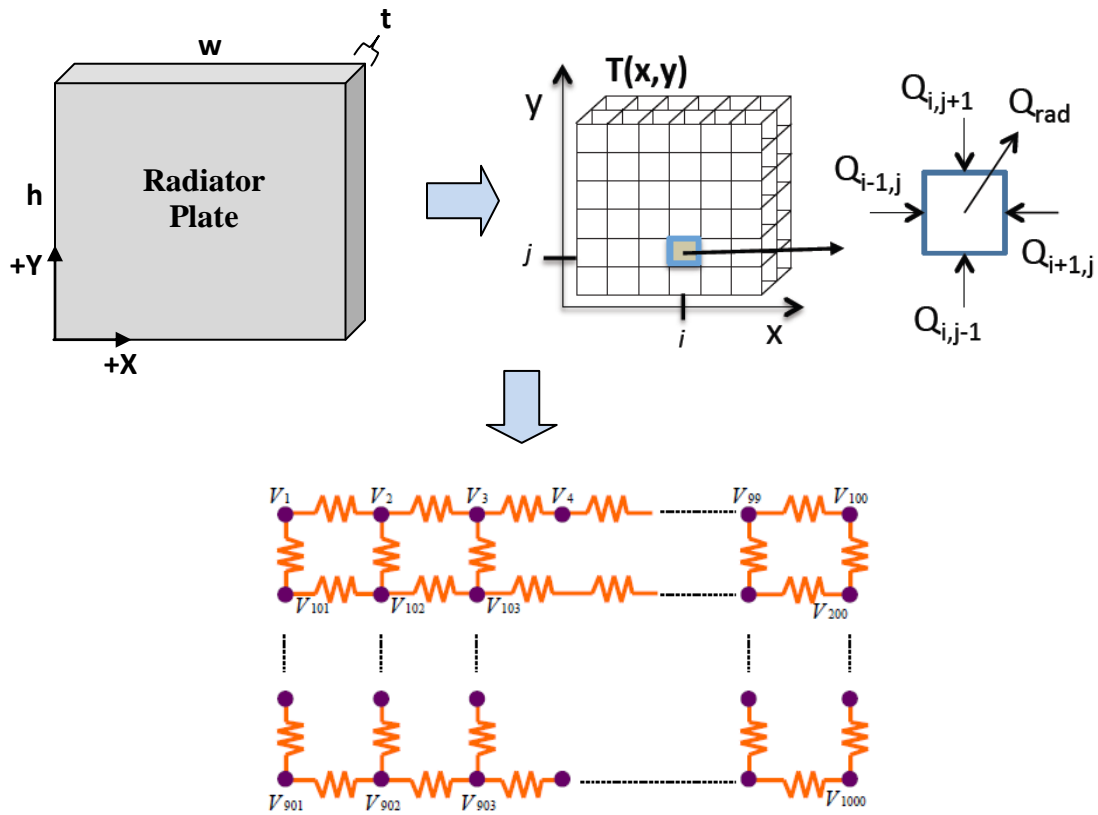


Figure 14: 2-D resistor grid representation of radiator plate

The following assumptions are used to formulate the problem:

- Heat enters the plate via a thermal strap that connects to the back surface.
- The remaining back surface and side areas are covered in MLI so that the heat escaping these surfaces via radiation is negligible.
- The plate is sufficiently isolated from the system so that no parasitic heat loads exist from the support structure of the plate.
- The front surface of the radiator is coated in a highly emissive paint so that the plate becomes an efficient radiator to deep space.

Figure 15 shows the resistor connectivity of each node on the radiating plate at a general location (i,j) on the plate. Each node has four neighboring nodes, unless it lies on an edge or corner of the plate. Heat transfer occurs both through conduction from neighboring nodes and radiation to

space (modeled as a current source). The only exception to the connectivity shown in Figure 15 are the nodes where the thermal strap, or heat source, is located on the radiator. At these point(s), there will be an additional current source capturing the heat flow into the radiator plate. Material properties of the radiator plate are captured in the emissivity (radiation) and thermal conductivity (resistance of conduction) parameters. Geometry is captured both in the structure of the resistor grid and the thermal resistance value – as the discretization values change, the thermal resistance between each node changes because resistance is a function of the distance between nodes. For a flat plate with a uniform discretization in both the width and height directions, the resistance values across the entire plate are identical.

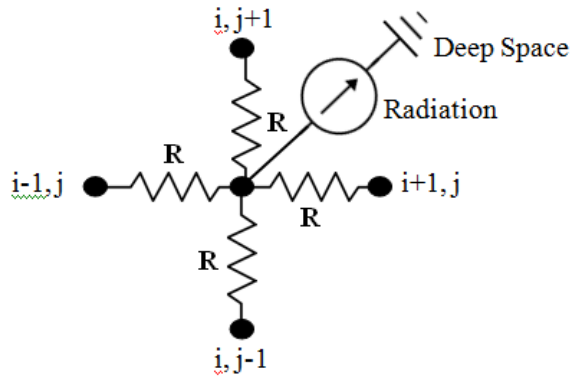


Figure 15: Resistor connectivity at arbitrary node location (i,j) of radiator

Now that a geometrical and material model of the radiator has been built with a resistor grid, it is necessary to examine the general heat transfer equation in the context of this problem. The goal is to reduce the heat transfer equation for this problem and formulate a stamping procedure to solve the system in the linear form $Ax=b$. In 2-D and in steady state, the general heat transfer equation from Equation 2.1 reduces to Equation 2.10 because the terms $\frac{\partial T}{\partial t} = \frac{d^2 T}{dz^2} = 0$ and the material is homogenous and isotropic.

$$\rho C_p \frac{\partial T}{\partial t} = 0 = \nabla \cdot (K \cdot \nabla T) + Q(T, t) = K \left(\frac{\partial^2 T}{\partial x^2} + \frac{\partial^2 T}{\partial y^2} \right) + Q(T) = 0 \quad (2.10)$$

In Equation 2.10, $\nabla = \left[\frac{\partial}{\partial x}, \frac{\partial}{\partial y}, \frac{\partial}{\partial z} \right]$ is the del operator. Using the definition of the second derivative, Equation 2.11 provides an approximation to the second derivative in the x-direction via finite differencing with the resistor construct. The derivatives in the y-direction are of identical form. For this derivation, the temperature of a node at station (i,j) is the temperature of the i^{th} node along the x-axis and the j^{th} node on along the y-axis. Let the i^{th} and j^{th} subscripts be defined as $T(x_i, y_i) = T_{i,j}$.

$$\frac{\partial^2 T_{i,j}}{dx^2} = \frac{T_{i+1,j} - 2T_{i,j} + T_{i-1,j}}{\Delta x^2} \quad (2.11)$$

Briefly ignoring $Q(T,t)$ and plugging Equation 2.11 into Equation 2.10, KCL can be written for each node in pure conduction mode. At this point, the problem is linear with respect to temperature. Therefore, the KCL for each node can be abstracted to a general stamping procedure to produce the nodal matrix, A, for the linear system $Ax = b$. The stamping formula for interior nodes on a 2-D resistor grid with uniform discretization in both the x- and y-directions is given by Equation 2.12. Because $Q(T,t)$ is temporarily assumed to be zero, the stamping procedure is not a function of the discretizations.

$$T_{i+1,j} + T_{i-1,j} + T_{i,j+1} + T_{i,j-1} - 4T_{i,j} = 0 \quad (2.12)$$

The stamping procedure in Equation 2.12 is of the same form as KCL in Equation 2.9 for the same 2-D resistor grid. Using the stamping procedure, a sparse nodal matrix, A, is constructed of the form shown in Figure 16. The example discretization chosen for the nodal matrix is 10 x 100 or 1000 nodes. The nodal matrix is sparse because of the low connectivity of the problem – each node is physically connected only to its neighbors. Identifying the structure of the nodal matrix for a particular problem allows for the fast and accurate solution to $Ax = b$. For example, sparse systems are solved efficiently via Gaussian elimination methods whereas

dense problems are aptly solved with iterative approaches such as conjugate gradient methods [20].

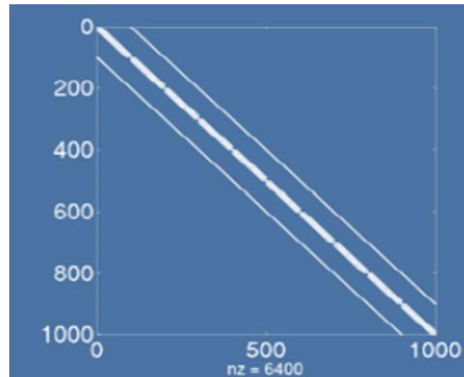


Figure 16: Sample nodal matrix structure for 2-D radiator with 10 x 10 discretization

To this point, the 2-D radiator problem has been linear because it operates in pure conduction. Radiation is captured by the source term, so $Q(T,t)$ in Equation 2.1 is non-zero in this problem. By introducing radiation governed by Equation 2.8, radiation out of the plate is nonlinear with respect to temperature (goes with temperature to the fourth power) so it cannot fit directly into the form $Ax = b$. By assuming a sufficiently small radiator plate (meaning small temperature gradients), a linearization of the Stefan-Boltzmann Equation can be used to retain the linear form to solve the system [21].

Assume the radiator has a full view factor to deep space and that the temperature of deep space is 0 K. To linearize, let T_o be the temperature of the radiator if it were completely isothermal as shown in Equation 2.13. For the same isothermal radiator, Q_o is the known heat load flowing into the radiator via the thermal strap and A_o is the area of the radiator. Equation 2.13 is a form of Equation 2.8 obtained by solving for T_o in terms of the known head load, Q_o . In this development, let the 'o' subscript indicate the physical quantities relating to the isothermal radiator solution, now referred to as the equilibrium solution. The linearization will assume small perturbations in temperature along the radiator surface about the equilibrium solution temperature.

$$T_o = \sqrt[4]{\frac{Q_o}{\sigma \varepsilon A_o}} \quad (2.13)$$

Let there be a small perturbation, dT , in the equilibrium solution such that the new temperature at an arbitrary (i,j) node in the 2-D resistor grid is given by $T_{i,j}$ in Equation 2.14. Equation 2.8 written for each node of radiator is then shown in Equation 2.15.

$$T_{i,j} = T_o + dT \quad (2.14)$$

$$Q_{i,j} = \sigma \varepsilon A_i (T_o + dT)^4 \quad (2.15)$$

Examining the high-order term in temperature and neglecting the dT terms of a larger order than one:

$$(T_o + dT)^4 = (T_o^2 + 2T_o dT + dT^2)^2 = T_o^4 + 2T_o^3 dT + T_o^2 dT^2 + 2T_o^3 dT + 4T_o^2 dT^2 + 2T_o dT^3 + T_o^2 dT^2 + 2T_o dT^3 + dT^4) \cong T_o^4 + 4T_o^3 dT \quad (2.16)$$

Substituting the result from the reduction in Equation 2.16 into Equation 2.15 yields Equation 2.17.

$$Q_{i,j} = \sigma \varepsilon A_i T_o^4 + 4\sigma \varepsilon A_i T_o^3 dT \quad (2.17)$$

Using Equation 2.14 and substituting into Equation 2.17:

$$Q_{i,j} = -3\sigma \varepsilon A_i T_o^4 + 4\sigma \varepsilon A_i T_o^3 T_{i,j} = -I_{rad} + R_{rad}^{-1} T_{i,j} \quad (2.18)$$

$$I_{rad} = 3\sigma\epsilon A_i T_o^4 \quad (2.19)$$

$$R_{rad}^{-1} = 4\sigma\epsilon A_i T_o^3 \quad (2.20)$$

Equation 2.18 is an expression for the Q(T) term in Equation 2.10 for the node located at station (i,j) on the radiator. Equation 2.19 and 2.20 are the contributions of radiation to the source term, b, and the nodal matrix, A, respectively. R_{rad} is included in each diagonal entry of A and I_{rad} is added to each element in b. Equation 2.21 shows the general stamping procedure into $Ax = b$ form for the radiator plate example with a uniform discretization, Δ , for the node of temperature $T_{i,j}$ located at (i,j).

$$K \left(\frac{T_{i+1,j} - 2T_{i,j} + T_{i-1,j}}{\Delta^2} + \frac{T_{i,j+1} - 2T_{i,j} + T_{i,j-1}}{\Delta^2} \right) + Q_{i,j} = 0 \quad (2.21)$$

The last step is to specify a boundary condition corresponding to where the thermal strap physically connects to the radiator. At these node(s), the source terms will be equivalent to the temperature of the thermal strap in contact with the radiator. Now that the Stefan-Boltzmann Equation has been linearized and is represented in the nodal matrix, the model is complete. The design variables for the radiator are geometrical and material: width, height, thickness, emissivity, and thermal conductivity. For a prescribed design, the resistor network analogy enables a solution of the system to be found using the linear representation of $Ax = b$, where A is the nodal matrix, x is the vector of temperatures at each node, and b is the vector of sources at each node. By solving for x, the predicted performance of the radiator plate, either in the form of max temperature or heat output, is obtained for a given design. Appendix D contains code to predict the maximum temperature for a 3-D radiator plate using this linearized thermal modeling construct. This model can be used for the case study developed in Chapter 5.

Chapter 3 – Methodology

The collective thermal design optimization process shown in Figure 17 is the central methodology of this thesis. The collective thermal design optimization of the REXIS critical thermal path in Chapter 5 is completed using this optimization process. The purpose of this chapter is to explain each element in the process. Each section details one of the four steps in this process: (1) generate the parameter file of the thermal path selected for study, (2) use the thermal path model(s) to predict performance, (3) establish the FOMs and formulate the optimization problem, and (4) select an optimization algorithm and iteratively update the design variables.

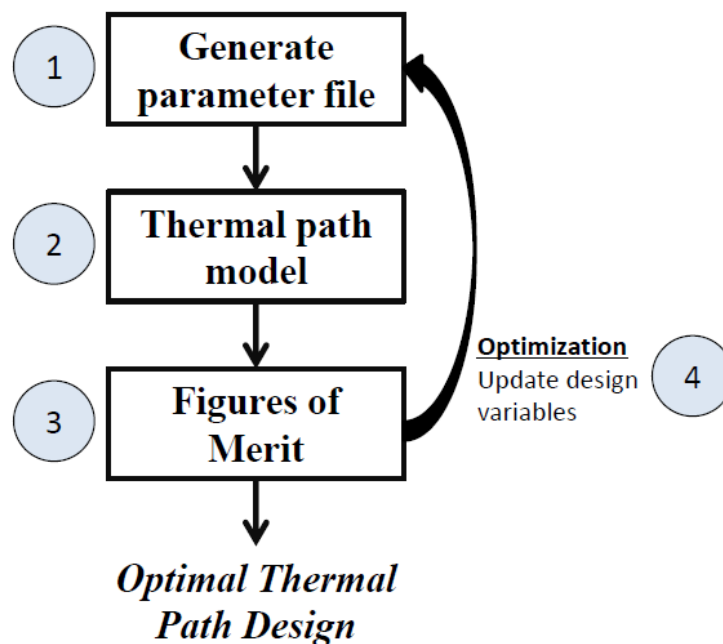


Figure 17: Collective thermal design optimization process

The first step is to generate a parameter file for the problem. The parameter file contains specified mathematical and physical characteristics of the system that are required to generate model predictions. Parameterization of the problem occurs only once: prior to the implementation of an optimization algorithm. Parameters include material properties and

geometries that capture the behavior of the components themselves, the component interactions with each other, and the component interactions with the system. Traditional thermal design will typically only capture the physical behavior of the components themselves and not include its interactions with other components and the system. The parameter file has two categories of parameters: (1) constants that do not change with each iteration of the optimization algorithm, and (2) design variables that do change with each optimizer iteration and are used to specify different candidate designs. The parameter file is functionally dependent on the physical system and is input into the thermal path model(s).

The second step is to call the thermal path model(s). The thermal path model(s) are also developed one time only – prior to the implementation of an optimization algorithm. Using the parameter file, the thermal path model(s) predict the performance of the candidate design. For example, a thermal model predicts component temperatures and a mass model returns the total thermal path mass. As the thermal path design optimization process iterates, the thermal path model(s) is used each time the design variables within the parameter file are updated.

The third step is to formulate critical FOMs for the collective thermal design optimization process. For each iteration of the optimizer, the predicted performance of a candidate design is evaluated against critical FOMs that are derived from TCS requirements. In the optimization problem formulation, the FOMs take the form of either objectives or constraints to the optimization. The example used in Chapter 5 of this thesis optimizes the mass of the thermal path subject to component temperature constraints.

The fourth and final step is the selection and formulation of the optimization algorithm. Selection of the optimization algorithm determines how the design variables in the parameter file are updated. How the parameter file is updated controls which candidate designs are evaluated. Formulating the optimization problem is the process by which the qualitative FOMs are written as mathematical expressions that must be satisfied by the algorithm. The final design is the optimal design with respect to the FOMs – it satisfies the constraints and has the optimal objective function value.

The methodology presented in this chapter differs from the traditional thermal design process in two major ways. First, traditional thermal design is often the result of point designs from experienced thermal professionals and occurs after the design of other subsystems, e.g.,

structural and payload design. Thus, the TCS, whose components are intimately tied to other subsystems, are not optimized with respect to performance or system resource consumption. Second, the literature (discussed in Chapter 1) primarily focuses on design optimization of thermal components in isolation from the spacecraft system. As a result, the design space for the thermal path is narrowed and the overall TCS has a suboptimal performance-to-mass ratio. The methodology of this thesis improves on traditional methods by specifying a parameterization that captures all components in a thermal path, broadening the design space and physically capturing functional interactions between components. Consequently, better design solutions that were previously unavailable are now achievable with the new parameter set.

In this chapter, the thermal design optimization process is presented in a general way as it might be applied to any spacecraft system, though examples are provided at each step to give context. Inputs to this process are an initial system architecture and design. At a minimum, a qualitative understanding of the critical thermal paths within the system is required because the most important thermal paths are selected for design optimization. Chapter 4 demonstrates this process for the REXIS TCS. The output of this process is a final design that satisfies requirements and achieves optimal performance, as defined by the FOMs.

3.1 Parameterization of Thermal Path

The objective of the parameterization process in collective thermal design optimization is to generate a parameter file that contains all physical quantities needed to solve the design problem. The parameter file contains four categorical elements:

- Material properties
- Geometries
- Component interactions
- Interaction with spacecraft system

Most of the quantities specified in the parameter file will be constant parameters for the design optimization. A reduced number of variables are chosen as design variables to iterate through candidate designs. Selection of the design variables is a critical step because it establishes the design space of feasible solutions for the optimization. Discussion in Chapter 5 of the thermal strap and radiator assembly illustrates this point. Material properties and geometries of the

components in the thermal path are physical quantities that drive the system performance and properties. Component interactions capture how the components within the thermal path physically and functionally relate to each other. Finally, the interaction with the spacecraft system is a set of boundary conditions included in the parameter file. An example boundary condition is the radiation from a thermal path component to an external surface of the spacecraft system.

The parameterization of the thermal path itself controls the feasible design space considered by the optimization algorithm. A general procedure for the parameterization of a thermal path is not the focus of this thesis. It will suffice to say that a parameterization is a strong function of the geometry and material component in a system. For example, a homogeneous, rectangular prism has geometry that is completely defined by three parameters: width, height, and length. As the component geometry becomes more complex, more variables are needed to accurately approximate the true shape and topology. Thus, selection of a parameterization for a component in the thermal path depends on the fidelity required in the model and the design solution. It is important to select a parameterization that does not exclude important regions of the design space. A design can be optimal for one parameterization and sub-optimal for another parameterization with the same objective and constraints. For example, consider the general problem of transferring heat from a source to a sink. A single heat transfer device, e.g., a copper strap, can be designed to have an optimal shape and topology for conduction between the source and sink. However, multiple copper straps may have a configuration that offers a better performance-to-mass ratio. In the case where only the single heat transfer device is considered, the single optimized copper strap is sub-optimal compared to the multiple copper strap design. Thus, it is important to fully capture the entire design space available when performing a parameterization of a thermal path.

As an example of how a thermal path can be parameterized, consider the simple 1-D heat conduction problem shown in Figure 18. The source, T_1 , is connected to the sink, T_2 , via a cylindrical rod. The rod has two sections of different length and cross-sectional area that are welded together. Heat transfer occurs conductively through the rod but not out of the rod, i.e., the rod is isolated so that it does not radiate. The goal of such a problem might be to maximize the heat flow to the sink so that T_2 is as large as possible while satisfying a mass requirement.

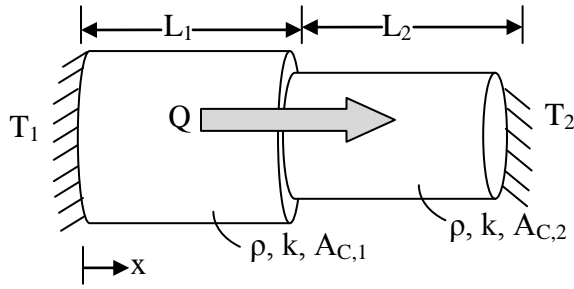


Figure 18: Example 1-D heat conduction problem

To create a parameter file for this example, the boundary conditions, geometry, and material properties for the problem must be completely specified. The parameter file for the 1-D heat conduction problem in Figure 18 is defined by Table 4. Only the variables pertaining to the mass, interaction between the two rod sections, and thermal performance are specified by the parameter file. In this example, each section of the rod is a component in the thermal path and both are concentrically aligned along the x -axis. Thus, the length of each section completely determines the interaction between the components. In the general case, however, the parameter file must also define the way the components within the thermal path interact in 3-D space as the design iterates.

Table 4: Parameter file for 1-D heat conduction problem

Parameter Type	Name	Units	Symbol
Design Variable	Rod cross-sectional area, first section	m^2	$A_{c,1}$
Design Variable	Rod cross-sectional area, second section	m^2	$A_{c,2}$
Design Variable	Rod length, first section	m	L_1
Design Variable	Rod length, second section	m	L_2
Constant	Rod density	kg/m^3	ρ
Constant	Rod thermal conductivity	W/m-K	k
Constant	Source temperature	K	T_1
Constant	Heat flow	W	Q

In Table 4, design variables were selected from the parameters that are continuous and

relate to the geometry of the rod. Design geometry is a natural choice as a design variable in thermal design because it directly controls the direction and magnitude of heat flows. The source temperature and heat flow are treated as boundary conditions to the problem and are accordingly labeled constant parameters. The rod thermal conductivity and density parameters are constants because they are discrete variables and material properties of the system. It is assumed that the material property has already been selected for the two-section rod. However, material properties for a discrete number of material choices could also be design variables. In this case, it is important to select an optimization routine that is well adapted to handle both continuous and discrete design variables.

To summarize, definition of the thermal path and a fundamental understanding of the system design are inputs to the parameterization process. Using this information, the parameter file specifies the geometry, material properties, boundary conditions, and component interactions for the thermal path. The parameter file is output from the parameterization step of the collective thermal design optimization process. Model(s) then use the parameter file to generate their predictions.

3.2 Creation of Thermal Path Model(s)

In the collective thermal design optimization process, the parameter file consisting of design variables and constant parameters is input to the thermal path model(s). Using this information, the model(s) outputs the performance or properties of the thermal path that become FOMs for the next step of the design optimization process. Examples of thermal models are provided below and in Chapters 4 and 5.

Thermal path performance, often measured by component temperatures, is predicted by capturing the relevant physics for the path. Modeling captures the conduction and radiation of each component using the tools discussed in Chapter 2. Furthermore, the model must capture appropriate boundary conditions for the system and the interaction between components. Additional models capture the system properties and performance of other subsystems, if desired. For example, a model that is functionally dependent on material and geometry is needed to return the expected mass of a thermal path. Tools for modeling thermal performance [17] [16] and the performance of other subsystems [14] at various levels of fidelity are available in the

literature.

Continuing the example problem introduced by Figure 18, two models can be constructed for the 1-D heat conduction problem: a mass model and a thermal model. Equation 3.1 gives the mass estimate of the rod as a function of the constant parameters and design variables specified in Table 4 in a density by volume calculation for the two-section rod.

$$m_{rod} = \rho L_1 A_{c,1} + \rho L_2 A_{c,2} \quad (3.1)$$

To create a model of the thermal performance, i.e., a predicted value for T_2 , Equation 2.7 is used. In this thermal model, there is no radiation from the bar to the environment so the Stefan-Boltzmann Equation is not used. Equation 3.2 is the simple thermal model for the 1-D heat conduction equation that predicts performance, T_2 , with the parameters given in Table 4.

$$T_2 = T_1 + Q \left(\frac{L_1}{kA_{c,1}} + \frac{L_2}{kA_{c,2}} \right) \quad (3.2)$$

3.3 Generation of Critical Figures of Merit and Optimization Formulation

This section summarizes the process of evaluating candidate designs and formulating an optimization routine. The process is first described in detail and then packaged into a three-step procedure for generating critical FOMs and formulating the optimization problem. Once a model(s) of the thermal path can predict performance for candidate designs, the performance is compared to critical FOMs. Critical FOMs are either system properties or performance parameters that map back to requirements of the TCS. Critical FOMs should either ensure satisfactory system performance or drive consumption of system resources as described by Chapter 1. For example, the temperature of a component is a performance parameter of a thermal path and the thermal path mass is a system property – both are critical FOMs.

Although this thesis primarily focuses on TCS performance FOMs, performance of a

thermal path is interdisciplinary. As a result, FOMs for other subsystems could also be considered, e.g., structures and power. Table 5 provides sample FOMs for a thermal path and the subsystem to which it pertains. Comparing the values of the FOMs enables quantitative evaluation of a thermal path design.

Table 5: Example FOMs for a thermal path

FOM	Units	Subsystem
Temperature	[°C]	Thermal
Max Plane Stress	[Pa]	Structures
Heater Power Consumption	[W]	Power
Mass	[kg]	System-level

The FOMs form the basis of the objectives and constraints of the thermal design optimization. Multi-objective system design optimization is the most general formulation for the problem of interdisciplinary FOMs [22]. However, this thesis uses a single-objective, constrained optimization formulation given by Equation 3.3. While the multi-objective formulation allows for the simultaneous optimization of multiple FOMs, the single-objective formulation focuses on a single FOM. Multi-objective optimization is advantageous because it facilitates the trading of one FOM for another along a Pareto-frontier of non-dominated design solutions [22]. Single-objective optimization is sufficient for the problem encountered in Chapter 5 because a minimum-mass thermal path is desired – thermal performance is a constraint to the optimization. This formulation follows the notion that many thermal requirements call for satisfaction of temperature limits with a minimal impact design. In this case, thermal performance becomes the constraint to the mass optimization problem.

$$\begin{aligned} \min J(\mathbf{x}, \mathbf{p}) \quad s. t. \quad & \mathbf{g}(\mathbf{x}, \mathbf{p}) \leq 0 \text{ and } \mathbf{h}(\mathbf{x}, \mathbf{p}) = 0 \\ & x_{i, LB} \leq x_i \leq x_{i, UB} \quad (i = 1, \dots, N) \quad \text{and} \quad \mathbf{x} \in S \end{aligned} \quad (3.3)$$

In Equation 3.3, \mathbf{x} is the vector of design variables belonging to the feasible domain S and \mathbf{p} is

the vector of fixed, or constant, parameters. The design variables, assumed to be continuous in this formulation, are specified within the upper and lower bounds, \mathbf{x}_{UB} and \mathbf{x}_{LB} , respectively. The variables $J(\mathbf{x},\mathbf{p})$, $\mathbf{g}(\mathbf{x},\mathbf{p})$, and $\mathbf{h}(\mathbf{x},\mathbf{p})$ comprise the complete set of FOMs. $J(\mathbf{x},\mathbf{p})$ is a scalar function and the FOM that should be minimized by a thermal path design. The inequality constraints, $\mathbf{g}(\mathbf{x},\mathbf{p})$, and the equality constraints, $\mathbf{h}(\mathbf{x},\mathbf{p})$, are not necessarily linear and must be satisfied by the design solution. The final design will represent the minimum value of $J(\mathbf{x},\mathbf{p})$ on S while satisfying $\mathbf{g}(\mathbf{x},\mathbf{p})$ and $\mathbf{h}(\mathbf{x},\mathbf{p})$.

In order to control how the thermal path attributes are traded against each other, each FOM is categorized as either an objective or constraint to the optimization. FOMs formulated as constraints to the optimization should trace back to TCS requirements that call for satisfaction but not optimization. An example of a constraint FOM is a survival, or non-operational, temperature of a component: as long as the component temperature is kept within prescribed limits, performance does not increase or decrease with temperature fluctuation. FOMs formulated as objectives to the optimization should trace back to TCS requirements that involve either the maximum or minimum values possible. A common objective of design optimization is to minimize the mass of the thermal path. Once the FOMs are categorized, the remainder of the optimization problem is formulated.

The following procedure is used to formulate the design optimization problem:

1. Generate list of critical FOMs that are traceable to TCS requirements and either drive system performance or resource consumption
2. Categorize FOMs based on whether they require optimization (objectives) or satisfaction (constraints)
3. Set the objective function, $J(\mathbf{x},\mathbf{p})$, inequality and equality constraints, $\mathbf{g}(\mathbf{x},\mathbf{p})$ and $\mathbf{h}(\mathbf{x},\mathbf{p})$, and bounds on the design variables, \mathbf{x}_{UB} and \mathbf{x}_{LB}

Once these steps are complete, design optimization can occur. Selection of the optimization routine that updates the design variables is dependent on the type of problem and what information is desired as part of the solution, e.g., desired slope values of the objective function at the design solution.

3.4 Survey of Optimization Routines

There are many optimization algorithms available to solve the thermal path design problem. Selection of an optimization algorithm will typically consider several factors that are unique attributes to each design optimization problem [23]. These factors include but are not limited to:

- Number of design variables
- Type of design variables (discrete vs. continuous)
- Linearity of problem
- Type of equality/inequality constraints
- Required code run time
- Feasibility of initial design solution

This section will survey the types of optimization routines and highlight those commonly used for design optimization in engineering. Most of the discussion in this section is qualitative, to simply introduce the reader to the types of algorithm trades typically seen in design optimization. If a formal algorithm selection process is needed, there is an abundance of literature that provides a structured algorithm selection method [23].

In general, optimization algorithms use an initial guess to establish a point in the design space and iteratively select new candidate solutions until the optimality criteria are satisfied. The specifics of how the algorithm guides the search through the design space vary with each type of algorithm. Algorithms can be divided into two major categories: (1) gradient-based methods and (2) heuristic methods. Gradient-based methods use gradient information at each point to guide the search. Heuristic methods use stochastic processes to find good solutions to the optimization problem – these solutions are not necessarily optimal. In any optimization problem, if the objective function is not convex on the domain of the design space, there is no guarantee that a global optimum exists.

Figure 19 illustrates the general structure of gradient-based optimization. To use gradient-based optimization, slope values with respect to the i^{th} design variable of the objective function, $\frac{\partial J}{\partial x_i}$, must be determined at each candidate design solution. Whether achieved through analytical expression or finite differencing, determining the slope values in the objective function requires a

functional relationship between the design variables and the objective function.

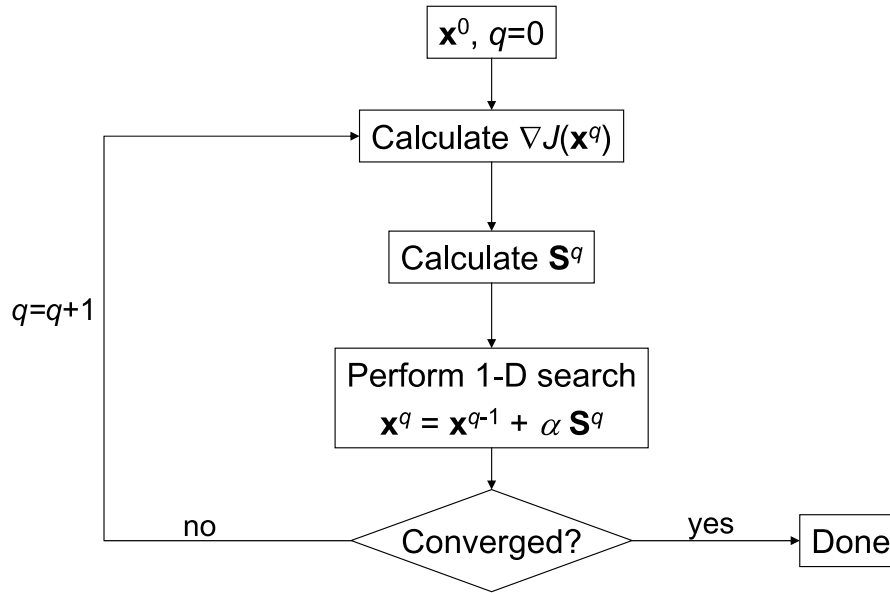


Figure 19: Gradient-based optimization process [24]

In Figure 19, \mathbf{S}^q is the search direction at iteration q and α is the optimal distance to move in the direction of \mathbf{S}^q . The search direction is determined from the gradient slope information and depends specifically on the selected algorithm. A common choice in engineering applications is to use Sequential Quadratic Programming (SQP) to solve for the search direction. SQP is also the algorithm selected for use in Chapter 5. An example SQP sub-problem formulation is given by Equation 3.4 [25].

$$\min Q(\mathbf{S}^q) = J(\mathbf{x}^q) + \nabla J(\mathbf{x}^q)^T \mathbf{S}^q + \frac{1}{2} \mathbf{S}^{qT} \mathbf{B} \mathbf{S}^q \quad (3.4)$$

$$s. t. \quad \nabla g_j(\mathbf{x}^q)^T \mathbf{S}^q + g_j(\mathbf{x}^q) \leq 0 \quad \text{for } j = 1, \dots, m_1$$

$$\nabla h_k(\mathbf{x}^q)^T \mathbf{S}^q + h_k(\mathbf{x}^q) = 0 \quad \text{for } k = 1, \dots, m_2$$

In Equation 3.4, SQP sets up the problem of solving for the optimal search direction as a sub-

problem to the optimization problem. The variable $J(\mathbf{x}^q)$ is the objective function and $\mathbf{g}(\mathbf{x}^q)$ and $\mathbf{h}(\mathbf{x}^q)$ are the linear constraints. For each iteration of the main optimization algorithm, SQP is run to find the optimal search direction in the search space for the candidate solution of the next iteration. For the first iteration, \mathbf{B} is the identity matrix; it then becomes the Hessian matrix of the objective function in subsequent iterations of the optimizer. The optimum search direction for the gradient-based optimization algorithm at iteration q is \mathbf{S}^q that minimizes Q in Equation 3.4. For more information on SQP please see [25].

Heuristic methods use stochastic processes to navigate the design space and find optimal or sub-optimal solutions. The advantage to heuristic methods is that no gradient information is necessary, and they are often used when there is little knowledge of the objective function over the design space. Because iteration between design points is random and specific to each method, there is no universal method for finding the search direction. Heuristic methods are not used in this thesis so qualitative detail is provided describing the structure of the algorithms in a less rigorous fashion. Table 6 introduces three commonly used classes of heuristic algorithms for design optimization: particle swarm [26], simulated annealing [27], and genetic algorithms [28]. Table 6 discusses each algorithm's structure qualitatively and the advantages and disadvantages to each. Knowledge of an algorithm's strengths and weaknesses is the first step in selecting a heuristic method for use.

Table 6: Commonly used heuristic optimization algorithms

Method	Structure	Advantages	Disadvantages
Particle Swarm	Each particle in swarm has position and velocity. Objective function determines which particle in swarm has best value.	<ul style="list-style-type: none"> • Shared “knowledge” among particles and particle “memory” • Handles discrete and continuous variables 	<ul style="list-style-type: none"> • High computation cost • More robust constraint handling methods are needed • Tuning of swarm size, inertia, and confidence
Simulated Annealing	Slowly converge to minimum “energy” state by perturbing design vector X_i	<ul style="list-style-type: none"> • Handles large design spaces • Handle discrete design variables well 	<ul style="list-style-type: none"> • Many iterations • Many function evaluations
Genetic Algorithms	Initialize population, select those for mating, crossover/mutation, insert into population	<ul style="list-style-type: none"> • Handles non-continuous design variables • Not susceptible to getting “stuck” 	<ul style="list-style-type: none"> • Must be well tuned • Must create penalty function for constraints to optimization

To summarize, selection of the optimization algorithm depends heavily on the problem to be solved. In general, an algorithm should be selected that can handle the structure of the optimization formulation (e.g., the presence of constraints) and efficiently and accurately achieve an optimal or near-optimal solution. Table 7 summarizes the advantages and disadvantages of each category of algorithms. Heuristic algorithms are a good choice, for example, if the problem has discrete design variables, is difficult to calculate slope values in the objective function with respect to the design variables, or if a global minimum is not required.

Table 7: Summary of gradient-based and heuristic algorithm advantages and disadvantages

Method	Advantages	Disadvantages
Gradient-Based	<ul style="list-style-type: none"> • Easy to apply constraints • Exploits gradient to approach solution • Can handle <u>many</u> design variables • SQP is widely used in engineering applications 	<ul style="list-style-type: none"> • Susceptible to getting “stuck” in local minima • Difficulty handling discrete design variables (constraint functions need be continuous and have continuous first derivatives)
Heuristic Algorithms	<ul style="list-style-type: none"> • Explore entire design space simultaneously • Translates well to multi-objective optimizations • No initial guess necessary 	<ul style="list-style-type: none"> • Computationally expensive • Must be well-tuned • Difficulty in handling constraints • Optimality not guaranteed

Chapter 4 – Preliminary REXIS Thermal Control System Design Evaluation

This chapter presents the REXIS TCS requirements, design, and predicted performance using a reduced-order model. The objective is to demonstrate understanding of the preliminary system design and modeling process necessary to carry out the collective thermal design optimization process shown in Figure 17. First, the thermal requirements for the REXIS instrument are presented. A passive TCS design that flows from the requirements is constructed. Then, a reduced-order model is used to evaluate design and predict performance of REXIS during primary operation. Identification of the critical thermal paths of REXIS is the final crucial step in this chapter. Once the thermal paths have been identified and their relationship with the spacecraft system understood, the collective thermal path design optimization in Chapter 5 can occur.

4.1 REXIS Thermal Control System Architecture and Design

4.1.1 Requirements

The driving REXIS TCS requirements are shown in Table 8. Both operational and non-operational temperature limits are specified. Prior to design, TCS requirements must be known so that all design elements, both functional and physical, are each traceable to a specific requirement. The primary temperature requirements for REXIS correspond to the electronics box and the CCDs. The electronics box houses all PCBs with components that manage the power regulation and command and data handling for REXIS. The CCDs are the X-ray detectors that record photon events for REXIS. Temperature requirements for both the electronics box and CCDs are critical to ensure that the instrument will meet its science requirements. Temperature requirements for each component should be satisfied across all mission phases.

Table 8: REXIS driving TCS requirements

Title	Statement	Type
Detector Assembly Operating Temperature Duration	The thermal system shall be able to continuously maintain the detector assembly at the operating temperature for 24 hours/day.	Functional/ Performance
Electronics Box Temperature Control Duration	The thermal system shall maintain the electronics box within operating limits for 24 hours/day during Phase 5B.	Functional/ Performance
CCD Survival Temperature Range	The temperature of the CCDs shall always be greater than -150°C and less than 75°C .	Functional/ Performance
CCD Operational Temperature Range	The temperature of the CCDs shall always be greater than -140°C and less than -55°C .	Functional/ Performance
MEB Survival Temperature	The temperature of the MEB shall always be greater than -20°C and less than 60°C .	Functional/ Performance
MEB Operating Temperature	The temperature of the MEB shall be greater than -10°C and less than 50°C while operating.	Functional/ Performance

4.1.2 Architecture

The REXIS TCS architecture flows from the requirements shown in Table 8. The architecture establishes the high-level system concepts including the general heat flow paths and boundary conditions for REXIS. The driving thermal requirements correspond to the electronics box, which is generally warm, and the detectors, which are much cooler. Given that the two elements must be physically connected through a mechanical interface, there is a need for a

thermal isolation layer (TIL) on REXIS. The TIL, shown in Figure 20, passively creates a temperature differential of at least 90 °C via low conductivity standoffs and MLI blankets. The detectors operate nominally at a temperature no greater than -60 °C – this provides 5 °C of margin to the detector operational temperature requirement of -55 °C. The nominal operating temperature of the electronics box is 30 °C. Conduction is the dominant mode of heat transfer in the TIL. Consequently, the temperature differential is particularly sensitive to the amount cross-sectional area used in the standoffs to isolate the electronics box from the telescope truss structure. The least low conductivity material that is structurally feasible is used for the TIL.

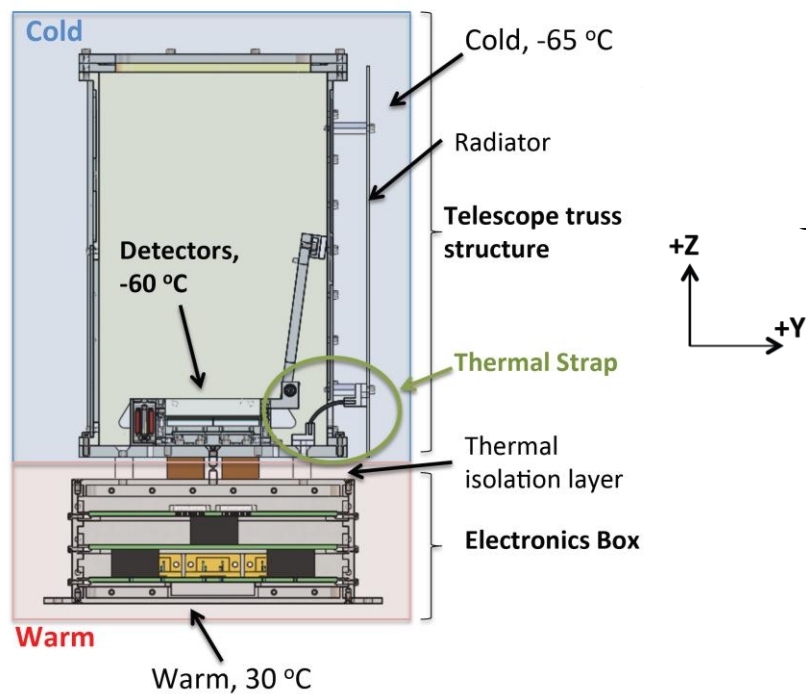


Figure 20: REXIS thermal architecture

A passive radiator and thermal strap are used to reject heat to deep space. Limiting the parasitic heat load to the telescope truss structure from the electronics box is not sufficient to meet the detector temperature requirement. There will be a heat load not only from the electronics box parasitic, undesired heat transfer, but from the power dissipation of the detectors themselves and the space environment, e.g., the asteroid and the radiative coupling with elements of the spacecraft deck. MLI is applied to all external truss structure surfaces of REXIS to limit heat transfer from the warm spacecraft deck to the cold REXIS telescope truss structure. The

thermal strap is physically mounted to the DASS, which is thermally coupled to the DAM and the detectors themselves. Heat flows through the thermal strap to the truss-mounted radiator plate that has a nearly complete view of deep space. The radiator is coated in a highly emissive white paint to efficiently reject its heat load to space.

Finally, the REXIS electronics box is thermally coupled to the spacecraft deck. In order to prevent excessive temperatures and heat load parasitic to the detector, there must be a sink for the heat load due to the power dissipation of the electronics. The REXIS design envelope is not large enough to accommodate a separate radiator specifically for the electronics box so the REXIS base plate has a good thermal connection with the spacecraft deck surface to ensure most of the heat load travels to OSIRIS-REx. To this point, the design of REXIS has been discussed at the architectural level. No quantitative component sizing information, detailed connectivity, or TCS performance information has been given. The REXIS TCS architecture is the understanding that a large temperature gradient exists between the telescope truss structure and the electronics box – a radiator dissipates the net heat load of the telescope truss structure and the spacecraft accepts the heat load from the electronics box.

4.1.3 Design Elements

The preliminary TCS design of REXIS consists of all instrument interfaces that facilitate heat transfer through conduction and radiation. Figure 21 is a N^2 diagram for the thermal system. The diagram is meant to show only interaction between components – not indicate a direction of heat flow. Thus, only one-half of the N^2 diagram is shown because it is symmetric. The components lie on the diagonal and the boxes indicating their connectivity are of the off-diagonals. Red boxes labeled ‘R’ designate a connection between components in radiation, and blue boxes labeled ‘C’ designate a connection between components in conduction. For example, there is a conductive connection between the CCDs and the DAM. The DAM is serially connected, in conduction, to the DASS, the thermal strap, and finally the radiator which emits heat to the space environment via radiation. The thermal N^2 diagram shown here is a reduced version of the entire system N^2 diagram shown in Appendix A. This section details the thermal design of REXIS, first by conduction and then in radiation, using the N^2 diagram. The objective is to provide the foundation to create a thermal model of the entire system.

DAM which is coupled to the DASS. From the DASS, there is serial conduction through the copper thermal strap to the aluminum radiator. The most significant contributor to the heat load dissipated by the radiator is the conduction from the electronics box to the DASS through the TIL. Conduction through the TIL, the dominant mode of heat transfer at this interface, occurs through a low conductivity standoff made from Torlon. Torlon has conductivity similar to G10/FR4 but can be machined and has stiffness on the same order of magnitude as steel. Thus, it is not only suitable to drive the large temperature gradient required in the TIL, but it can support the REXIS telescope truss structure in the launch vibration environment. Finally, the electronics box is conductively coupled to OSIRIS-REx – this will ensure that the majority of the power dissipated by the electronics flows in the $-z$ -direction into the spacecraft instead in the $+z$ -direction, through the TIL.

Thermal control in radiation is primarily achieved by selecting surface coatings that have the desired optical properties for heat transfer or isolation. All external surfaces of REXIS radiate to the environment. In Figure 21, the environment can either be deep space or the asteroid. For example, the mask receives a radiation heat load from the warm (roughly 50 °C) asteroid during operation. However, polished gold has a very low emissivity so that heat transfer to the thin mask is limited. Also thermally coupled to the environment, the radiator has nearly a complete view to deep space and is coated in a white paint with a high emissivity to efficiently reject heat to deep space. The external surfaces of the truss panels and the electronics box are covered in MLI to isolate REXIS thermally from the warm environment of the OSIRIS-REx instrument deck. MLI is also applied to both surfaces of the TIL to isolate the DASS and the top surface of the electronics box in radiation. Internal to REXIS, the side shields are coupled to the detectors and each other. They are gold electroplated so that the data gathered by the CCDs is not corrupted by lines from aluminum. The low emissivity gold electroplating means that each side shield emits very little heat via radiation – instead, each is primarily tied to the temperature of its corresponding truss panel in conduction.

4.2 Reduced-Order Thermal Model

The reduced-order model presented in this section is a mathematical approximation to the physical behavior of the preliminary REXIS TCS design. The objective is to create a model that is relatively quick to construct, sufficiently accurate to assess candidate designs, and quick to run

on a standard computer platform. For a complete set of input parameters, the model can predict temperatures of components that map back to the requirements of the TCS design. Input parameters include thermal environmental factors, geometry, material properties, and power settings. The thermal model presented in this chapter reflects the preliminary modeling efforts to evaluate early TCS concepts and critical sensitivities. Appendix E documents a higher fidelity preliminary design of REXIS using Thermal Desktop as the modeling software.

This reduced-order model follows the form of the REXIS TCS established in Figure 21: a single node in the model represents each component. Conduction and radiation linkages will be made between nodes which capture the geometry and material properties of the connections. A nonlinear model of the system is constructed that returns the temperature time history of each node as a function of time, as described by the formulation in Figure 22.

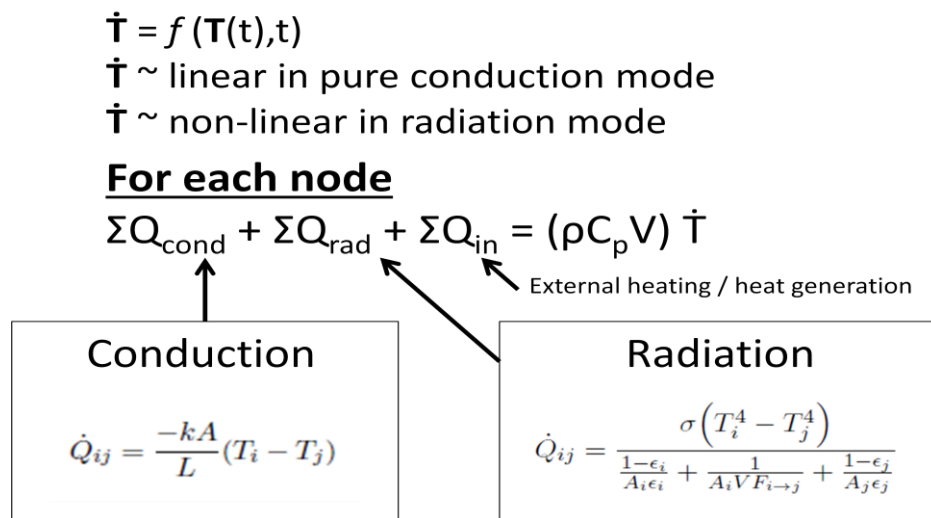


Figure 22: Reduced-order model formulation

In Figure 22, the heat transfer equation is solved for each node in the TCS. The solution is that of a nonlinear, first order ordinary differential equation in temperature. The conduction and radiation equations specify the heat load from the j^{th} to the i^{th} node. The sum of the radiation and external heating terms equals the source term in Equation 2.1. With knowledge of the heat capacity for each node, the temperature-time derivative, $\frac{dT}{dt}$, is known at each time step. The general expression for $\frac{dT}{dt}$ is given by Equation 4.1. Given an initial set of TCS temperatures, the

system temperatures are propagated forward in time using Equation 4.1 to update the TCS temperatures at each time step.

$$\frac{dT}{dt} = (\rho C_p V)^{-1} (\sum Q_{cond} + \sum Q_{rad} + \sum Q_{in}) \quad \text{for each node} \quad (4.1)$$

In Equation 4.1, ρ is the density, V is the volume, and C_p is the specific heat. Q_{cond} are the conductive heat flows, Q_{rad} are the radiative heat flows, and Q_{in} are the external heat loads defined in Figure 22. Using the nonlinear differential equations solver in MATLAB, the reduced-order thermal model is solved as a system of equations as show by the code flow structure in Figure 23.

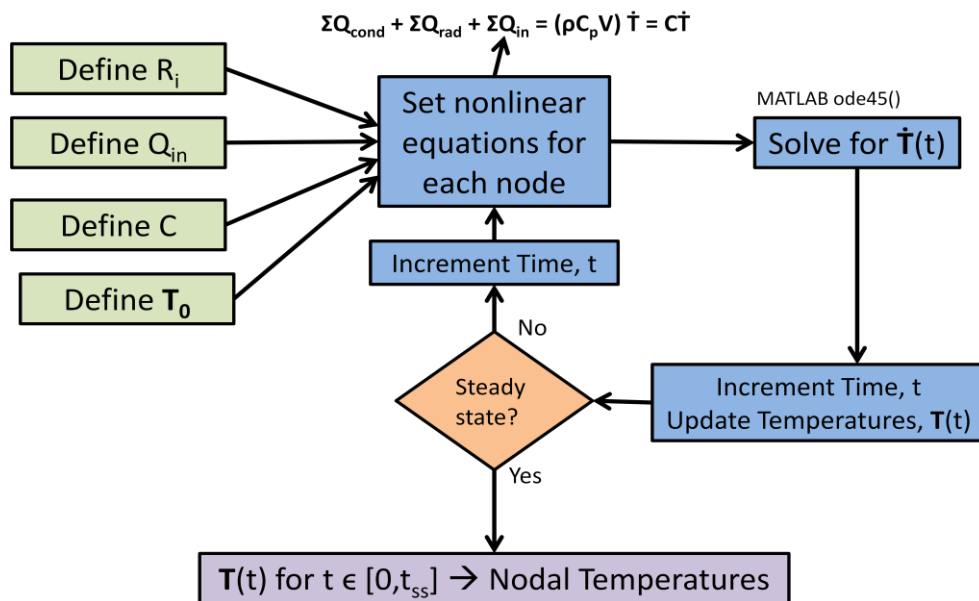


Figure 23: Reduced-order model code structure

In Figure 23, the heat capacity for each node, thermal resistances, input heat loads to the system, and initial temperatures are specified before the system is solved. For each time step, the formulation shown in Figure 22 and Equation 4.1 is used to calculate the temperature slope with

time to update the temperatures at each new time step. The MATLAB command ‘ode45’ is used as the algorithm to solve the first order heat equation. ‘ode45’ uses a variable step Runge-Kutta Method to solve the differential equations numerically using the temperature function handle, the time span, and the initial system temperatures. The 4th and 5th order Runge-Kutta Method is a common choice in engineering applications because it is both accurate and computationally fast for many systems. Once the system has reached steady state temperatures corresponding to t_{ss} , the algorithm terminates. In this case, steady state is defined as the max temperature difference between time steps not exceeding a threshold value. For more detail regarding the code structure and the input parameters used in the model, please see Appendix B.

4.3 Thermal Model Predictions

4.3.1 Mission scenarios

In order to generate thermal predictions for REXIS, the thermally bounding scenarios for each mission phase must be known. Each scenario presents a different thermal environment that will lead to different temperature predictions. Because OSIRIS-REx is an interplanetary mission performing science observations at the asteroid Bennu, the thermal environment is heavily dependent on the spacecraft’s heliocentric orbital radius and its proximity to the asteroid. Table 9 shows the nominal thermal environments for each phase of the mission. The case description column includes information as to the sun range, the direction of the sun in the spacecraft frame, and the surface temperatures of the Bennu, if present. The solar range and intensity columns are used to find the incident flux on the system due to direct sunlight. The altitude of the spacecraft is used to find the flux on the system due to the asteroid. Finally, the ‘REXIS State’ column refers to whether the instrument is off, in a survival mode, or on, in an operational mode.

Table 9: Thermally bounding nominal mission scenarios for REXIS

Case	Case Description	Sun Distance (AU)	Solar Intensity (W/m ²)	Sun Offpoint from +X (deg)	RQ36 Altitude	REXIS State
Cruise						
Cold	Cruise, max outbound range, sun +X	1.387	700.1	0	--	Off
Hot	Cruise, perihelion, sun +X	0.773	2322.1	0	--	Off
Orbital A						
Cold	Orbital A, max solar range, sun +X, no RQ36	1.387	700.1	0	--	On
Orbital B						
Cold	Orbital B, max solar range, sun +X, min RQ36 temperature profile	0.897	1724.4	0	750 m	On
Hot	Orbital B, min solar range, sun +X, max RQ36 temperature profile	1.387	700.1	0	750 m	On

In Table 9, Cruise Phase is the case where OSIRIS-REx is in an interplanetary orbit about the sun. In this case, the asteroid is not present and REXIS is off. During this phase of the mission, it is only necessary that REXIS survive – every few months turning on to calibrate the instrument. Once the spacecraft arrives at the asteroid, science activities for the payload instruments begin. REXIS calibrates during Orbit Phase A and operates during Orbit Phase B. Throughout the entire mission, the Cruise Phase cold case is the coldest environment and Orbit Phase B hot case is the hottest environment. The geometry of REXIS during Orbit Phase B is shown in Figure 24 for reference. In this orientation, REXIS is nadir-pointed at the asteroid surface in a circular, terminator orbit with an altitude of approximately 750 m. A notional platform is shown in Figure 24 to represent the spacecraft instrument deck. The direction of the sunlight in all cases comes from +X in the spacecraft frame, as shown in Figure 24.

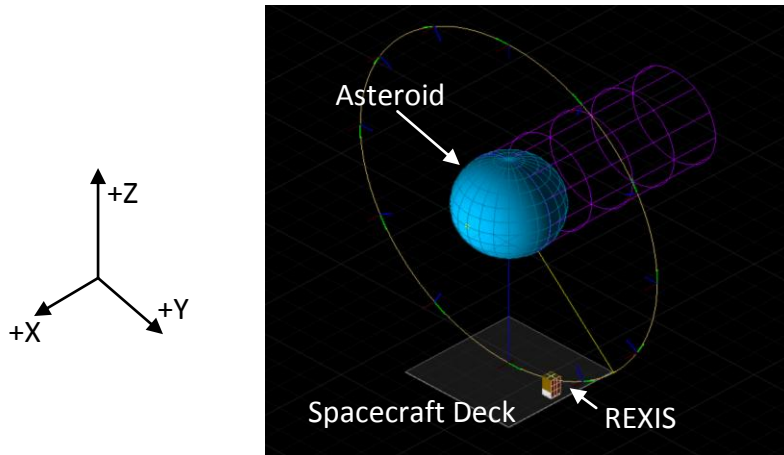


Figure 24: Notional geometry for REXIS during Orbit Phase B

As an instrument that needs to operate at cold temperatures in a warm environment, the primary TCS challenge is meeting operational requirements during Orbit Phase B. The Orbit Phase B hot case drives the design of the REXIS radiator, thermal strap, and TIL because environmental heat loads are the largest in this scenario. In this phase, the spacecraft is nearest to the sun, the asteroid is closer than any other mission phase, and REXIS is on and operating. Consequently, results are presented for the Orbit Phase B hot case to evaluate the preliminary design of REXIS for the hot bounding case.

4.3.2 Model Predictions

The reduced-order model developed in section 4.2 was run for the Orbit Phase B hot case. Figure 25 shows the temperature predictions made by the reduced-order model for the Orbit Phase B hot case. The initial temperatures were generically set to 0 °C because no initial system temperatures are known. The model was run until the temperature of all the components reached a steady state value. In this case, the steady state temperatures are of primary interest so the initial conditions do not affect the determination of the critical REXIS thermal paths.

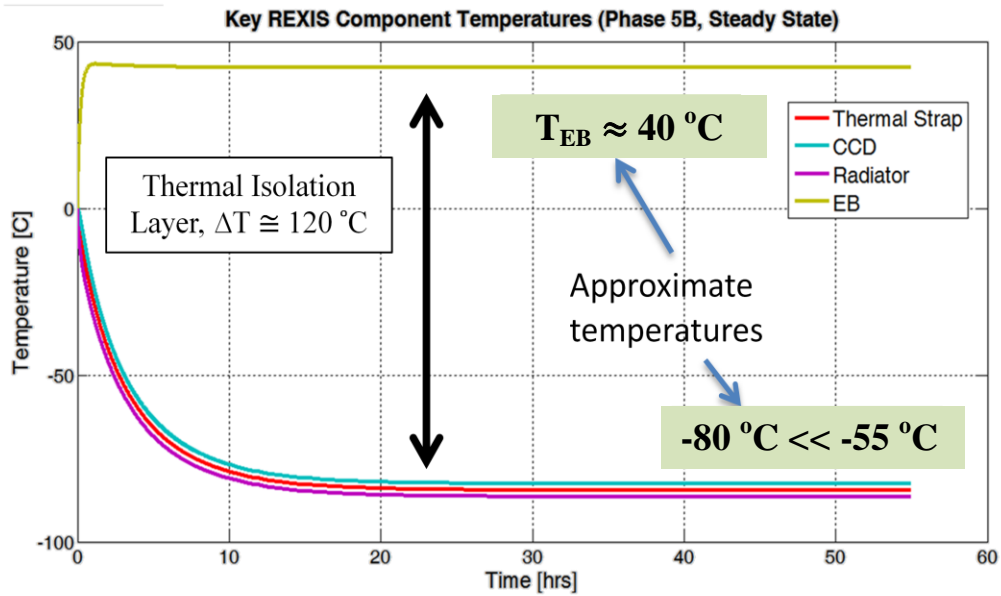


Figure 25: Reduced-order model predictions for Orbit Phase B

In Figure 25, the TIL is driving a temperature differential of approximately 120 °C – well above the nominal 90 °C difference. Thus, there is a 30 °C of margin for this interface. Table 10 displays the steady state temperatures predicted by the model, as well as the component rise times and operational requirements for the components from Table 8. At the prescribed initial conditions, the rise time for the electronics box is much shorter because it is thermally coupled to the spacecraft deck which is at constant temperature. The telescope truss structure, including the radiator and the detectors, has a much longer rise time because it has a significant thermal inertia and is relatively isolated from the electronics box.

Table 10: Summary of reduced-order model predictions

Component	Steady State Temperature (°C)	Operational Temperature Requirement (°C)	Rise Time (10% to 90% the step size, in hours)
CCDs	-83	Less than -60 °C	8.1
Electronics Box	42	Less than 45 °C	0.4
Radiator	-87	--	8.1

In Table 10, driving requirements on the electronics box and the CCDs are satisfied. The temperature requirement for the CCDs is met with greater than 25 °C of margin. Physically, this

means that there is excess margin in the TCS design – in general, excess margin is good for the thermal engineer but it often indicates that components are using system resources inefficiently. In this case, the margin could be reduced by decreasing the radiator size or thermal strap cross-sectional area, for example. These results lead to two important conclusions:

- The preliminary TCS design is feasible and meets driving thermal requirements
- There is sufficient margin to warrant design optimization of REXIS thermal components

Before additional design efforts are made, it is important to verify the reduced-order thermal model. Verification will ensure that conclusions made based on the reduced-order model are justified because the model captures the physical behavior of the TCS. Once verified, the critical thermal paths within REXIS are identified.

4.4 Model Verification

Evaluating a design with a thermal model is only meaningful if the model can be trusted. Model verification is the process by which the predictions of an unverified model are compared to a trusted source – it can be experimental data or a verified model. While model-data correlation to actual experimental data of REXIS in a flight-like thermal mission scenario is the preferred method of verification, an engineering test unit thermal mockup of the current REXIS TCS tested in a thermal vacuum chamber did not fit into the program schedule. Thus, the thermal model predictions are compared to predictions from Thermal Desktop, an industry standard modeling tool, to verify its output.

In his Master’s thesis [17], John Richmond performed model-model correlation between his thermal model developed in a MATLAB application and Thermal Desktop. He outlined two criteria that are used in this thesis to perform model verification:

- Max temperature error of less than 11 K
- Average percent error in temperature of less than 5% for all time

The max temperature error correlation requirement was derived from the JPL/NASA standard [16] for applying thermal margin to account for system parameter and environment uncertainties. The 5% average error correlation requirement was a standard enforced in his thesis to ensure satisfactory correlation over the entire time domain. If predictions between the two models agree

within these acceptance criteria, the models are deemed correlated.

The process for model-model verification is shown in Figure 26. With the preliminary model of REXIS in place, a Thermal Desktop version of the model is constructed to be mathematically and physically identical, i.e., all input parameters are the same. Using bounding hot and cold cases, both models are run for the same environmental conditions. If the correlation acceptance criteria are met, the models are in agreement and the reduced-order model of REXIS is verified. In the event that the models do not agree within the prescribed correlation criteria, the reduced-order model is adjusted. How to change the model is critical to preserving the physical relevance in its predictions. Correlation requires the answer to two questions: Are all of the meaningful physics modeled? Are the physics modeled correctly? If the models do not at first correlate, the engineer should ensure all the physics are modeled correctly before adding new physics to the model. New physics, e.g., radiation from a surface that was previously unaccounted for, should be added in order of influence to the temperature predictions.

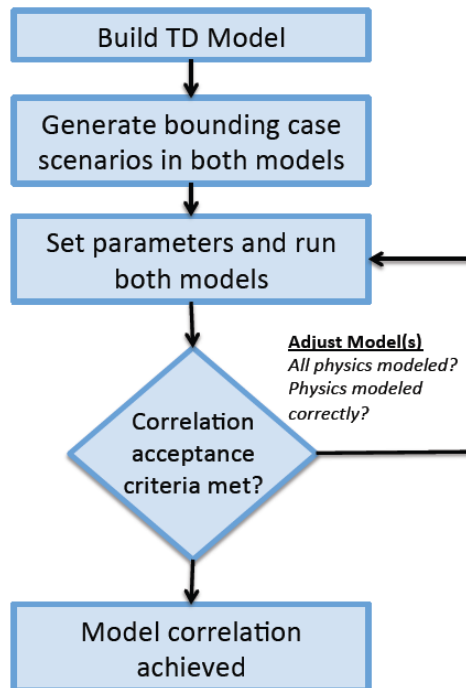


Figure 26: Model verification process

The model verification process shown in Figure 26 was completed for the reduced-order

model of REXIS. Figure 27 shows a Thermal Desktop model of REXIS. Effort was taken to maintain the same level of component detail between the reduced-order model and the Thermal Desktop model. The electronics box is modeled as a six-sided box mounted to the spacecraft deck. The truss panels and side shields are modeled as aluminum plates that support the mask and radiator. Finally, the DAM is represented with an aluminum block with the same heat capacity as the DAM and detectors. Using the hot and cold bounding cases provided in Table 9 of section 4.3.2, predictions from the Thermal Desktop model were compared to the predictions given in section 4.3.3.

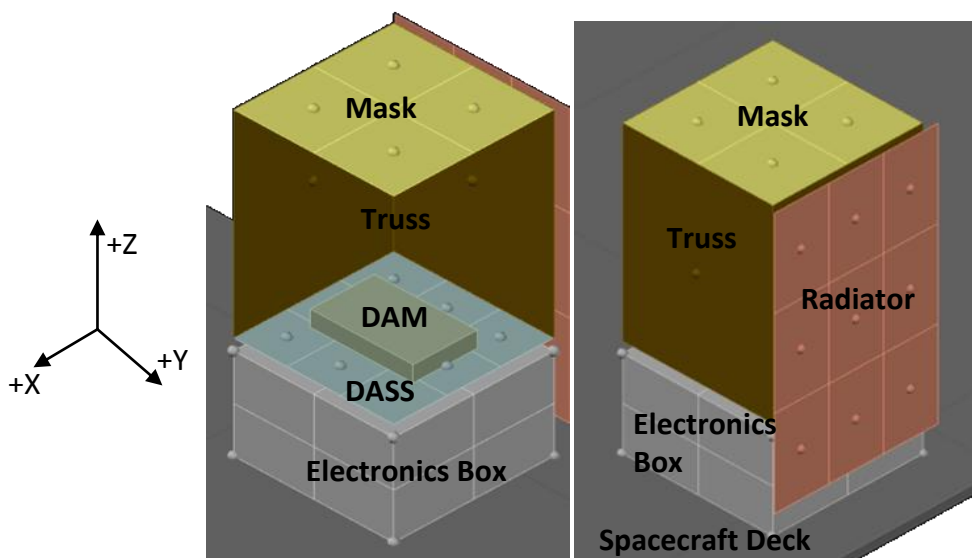


Figure 27: Thermal Desktop model of REXIS

While the models closely agreed, they did not at first meet both correlation acceptance criteria. Comparative analysis showed that by adding radiation from the external surface of the truss panels to deep space in the reduced order model, the models were correlated. Table 11 shows the correlation criteria for each model for the hot and cold bounding cases. Each node of both models meet the average error and max temperature error criteria.

Table 11: Model verification results of reduced-order model with Thermal Desktop model

Cold Case	EB	Mask	Truss +Y	Truss +X	Truss -X	Truss +Y	DASS	DAM	Radiator
<i>Avg % Error</i>	-0.3	-3.0	-3.2	-3.0	-3.1	-3.0	-1.9	-1.9	-2.6
<i>Max Temp. Error (K)</i>	2.1	7.3	7.6	7.2	7.4	7.2	5.0	5.2	6.3

Hot Case	EB	Mask	Truss +Y	Truss +X	Truss -X	Truss +Y	DASS	DAM	Radiator
<i>Avg % Error</i>	-0.1	-1.8	-2.7	-1.7	-2.4	-2.0	-2.0	-2.1	-2.6
<i>Max Temp. Error (K)</i>	1.6	4.9	6.7	4.7	6.1	5.1	5.4	5.6	6.5

In Table 11, the average error and max temperature error consistently show that the reduced-order model predicts warmer temperatures than the Thermal Desktop model. The warmer temperatures are primarily because in Thermal Desktop, each node radiates to deep space. Furthermore, the view factor calculation is a ray tracing method that captures reflections. The reduced-order model does not capture radiation from each surface – only critical surfaces such as the radiator. Additionally, the analytical view factors used in the reduced-order model do not account for reflections of light. The net effect is that more heat is rejected to space in the Thermal Desktop model, resulting in lower temperatures on average. However, the correlation criteria are met and the reduced-order model was deemed sufficiently verified.

4.5 Identification of Critical Thermal Paths

The reduced-order model of the preliminary TCS design has been used to generate predictions for the thermally bounding Orbit Phase B hot case and the model is verified. The model is conservative because the maximum expected value for the power dissipation of the electronics was used as the heat load input instead of the current best estimates. Additionally, the radiator was sized to a detector temperature of -60°C which provides 5°C of margin to the operating requirement. Thus, the margin in the point TCS design developed in this chapter is held in the heat load values and the radiator size. The final step presented in this chapter is to

identify the critical thermal path within the REXIS TCS. In general, knowledge of which thermal paths drive thermal performance and resource consumption determines the areas of the system that should be optimized. The critical thermal path of the REXIS system is the input information to the collective thermal design optimization process shown in Figure 17.

The identification of critical thermal paths is both a qualitative and quantitative process. On one hand, the TCS model can be used to derive quantitative information about the margin and system sensitivities – on the other hand, the engineer must understand that models are incomplete. For example, subjecting a component to design optimization could mean that the design solution is not machine-able, violates requirements for other sub-system requirements, is too risky or costly, or has less flight heritage. For the REXIS TCS, a temperature sensitivity analysis shown is in Figure 28. A 5% forward difference perturbation in the thermal resistance of various connections illustrates the sensitivity of the electronics box and CCDs to changes in thermal path conductance. The sensitivity analysis of the driving requirements expresses which thermal paths most heavily impact thermal performance.

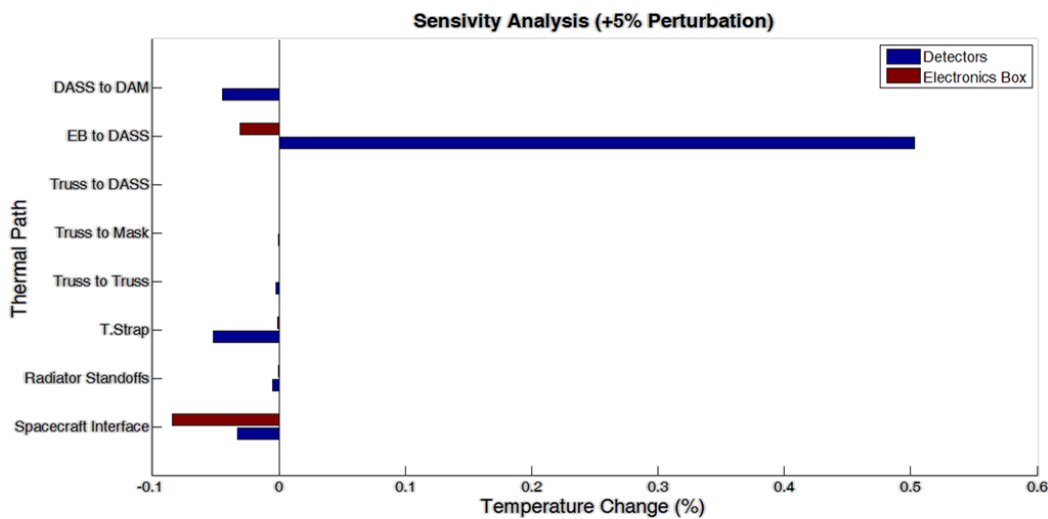


Figure 28: Sensitivity Analysis of REXIS thermal paths using reduced-order model

In Figure 28, the most performance-critical thermal path is shown to be the EB to DASS connection (this is the thermal path through the TIL). The temperature of the CCDs during operation is particularly sensitive to the resistance values of the REXIS interface with the spacecraft deck, the thermal strap, the TIL, and the DASS to DAM connection. The electronics

box temperature is primarily affected by the TIL and the spacecraft interface. The single most impactful thermal path affecting performance is the TIL – an intuitive result because the design of the TIL controls the magnitude of the gradient between the warm EB and the cold telescope truss structure of REXIS. While the TIL is the most performance-critical thermal path, it does not drive the mass of the TCS.

Upon examination of the REXIS mass budget, the thermal strap and radiator assembly sums to approximately 80% of the REXIS TCS mass. The remaining TCS elements – trim heaters, temperature sensors, MLI, surface coatings, and TIL standoffs – are low in mass compared to the thermal strap and radiator thermal path. As a performance- and mass-critical thermal path, it is a critical thermal path for design optimization. In addition to the information from Figure 28, the reduced-order model output confirms that most of the heat is either dissipated through the electronics to spacecraft deck interface or emitted from the surface of the radiator to deep space. That the thermal strap drives the detector temperature the second most in Figure 28, and that the thermal radiator assembly primarily drive the total TCS mass leads to the conclusion that the thermal strap and radiator assembly is the single-most important thermal path in REXIS. Chapter 5 will implement the collective thermal design optimization process on this thermal path.

4.6 Summary

This chapter identified the critical thermal path of REXIS as the thermal strap and radiator to be subjected to design optimization in Chapters 5. Stemming from the driving TCS requirements, the REXIS thermal architecture and design was presented. A reduced-order model with one node allocated for each component was used to predict the performance of the preliminary REXIS TCS design. The preliminary REXIS design meets requirements with over 25 °C of margin to the detector temperature requirement, suggesting design optimization to reduce resource consumption and increase performance efficiency. Once verified, the model was used to perform a sensitivity analysis of the thermal paths within REXIS. The most critical REXIS thermal path is the thermal strap and radiator assembly because it drives both thermal performance and mass of the TCS.

Chapter 5 – Design Optimization of the REXIS Thermal Strap and Radiator Thermal Path

This chapter uses the REXIS thermal strap and radiator assembly as a case study to demonstrate the collective thermal design optimization process shown in Chapter 3. Chapter 4 introduced a REXIS TCS point design and a preliminary thermal model that was used to predict nominal thermal performance of the design in Orbit Phase B, the bounding hot case for REXIS. The TCS point design has excess margin to the detector requirement, indicating that design optimization would maximize the performance-to-mass ratio. Using a temperature sensitivity analysis and the TCS mass budget, the thermal strap and radiator assembly were identified as the critical thermal path of REXIS. This thermal path both drives performance – the detector operating temperature – and the total mass of the TCS. In this case, the optimal design of the thermal path is a minimum mass radiator and thermal path configuration that satisfies the steady-state detector operating temperature requirement in Table 8. This chapter devotes a section to each step of the collective thermal design optimization process shown in Figure 17. Once an optimal design is achieved, results are presented and conclusions are summarized. The key reason for implementing the collective thermal design optimization process is that it offers a design solution with a better performance-to-mass ratio than design solutions achieved with a traditional thermal design process. The thermal strap and radiator design solution in this chapter are shown and the performance-to-mass improvement as a result of implementing this methodology is discussed.

5.1 Parameterization of Thermal Path

The first step of the collective thermal design optimization process is to generate a system diagram of the thermal path, including boundary conditions to the system. The thermal path diagram represents the components – the thermal strap and the radiator – as nodes and shows the heat flows through the thermal path. The diagram is a high-level snapshot of what is included in the optimization and how it interacts with the rest of the TCS. From the diagram, a parameterization of the thermal path is chosen that completely characterizes the physical behavior of the system. The parameterization captures the geometry and material properties of the components, the component interactions with each other, component interactions with the

system, and environmental boundary conditions. The output of this step is a parameter file that completely describes the thermal strap and radiator assembly. To create a thermal path diagram, the thermal path must be isolated from the REXIS TCS design shown in the N^2 diagram of Figure 21.

Figure 29 shows a picture of the REXIS TCS concept to provide context to the N^2 diagram. The thermal strap and radiator are physically connected to the telescope truss structure of REXIS. By removing the truss panels and side shields, the DAM is visible in the side view of Figure 29. The thermal strap, connected to the DASS, draws the heat flow from the detectors to the radiator to be emitted to deep space. Arrows indicate the general direction of heat flow. The thermal strap and radiator are sized to dissipate the total telescope truss structure heat load. Thus, the radiator is sized for the maximum heat load. The thermal path diagram follows directly from this system concept.

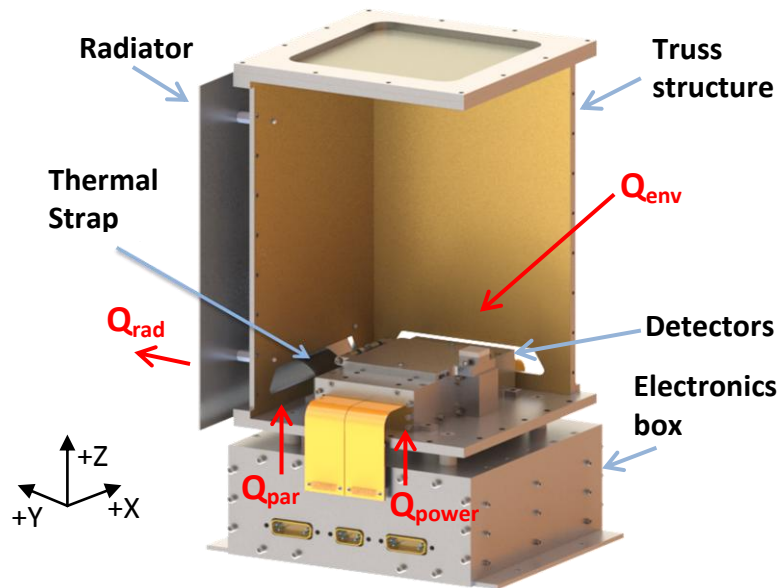


Figure 29: REXIS TCS Concept

The four heat flows shown in Figure 29 are a complete set for the thermal strap and radiator thermal path. Q_{env} is the net effect of the environment on the telescope truss structure, including radiation from direct sunlight, the warm instrument deck environment, and the

asteroid. Q_{par} is the parasitic heat load on the detectors from the wiring that extends from the electronics box to the telescope truss structure. The final heat loading term Q_{power} captures the power dissipation of components in the telescope truss structure that require electricity for operation, such as temperature sensors and the CCDs. The sum of the Q_{env} , Q_{par} , and Q_{power} equals the total heat load that must be dissipated by the radiator, Q_{rad} .

Using the thermal model developed in Chapter 4 and the 1-D conduction equation (Equation 2.7), it is estimated that the total heat load is equivalent to 1 W. In this case, the temperature difference between the maximum radiator temperature and the DASS and the thermal resistance of the thermal strap are used to find the total heat flow through the thermal strap. However, the 1-D conduction approximation assumes that the thermal strap and backside of the radiator are perfectly insulated from radiative parasitic heat loads. Furthermore, the assumption that the entire heat load enters the radiator through the thermal strap neglects the heat load to the radiator entering from the radiator standoffs. Because the 1 W total heat load assumption is optimistic, 100% margin is applied to the heat load for this case study. The total heat load is constant and $Q_{\text{total}} = Q_{\text{rad}} = 2 \text{ W}$.

Using the heat flows and system concept introduced in Figure 29, the thermal path diagram is shown in Figure 30. To construct the thermal path diagram, the 1-D conduction assumption is applied to the thermal strap, in which heat transfers in one direction through the strap via conduction only. The detectors and DAM are treated as isothermal because their temperatures are strongly coupled. Finally, the backside of the radiator and radiator standoffs are treated as perfect isolation from the REXIS structure. The entire heat load of $Q_{\text{total}} = Q_{\text{rad}} = 2 \text{ W}$ flows through the DAM. Assuming that the entire 2 W transfers through the DAM is conservative because there are thermal paths, from the truss panels to the thermal strap for example, that do not require heat to flow through the DAM. Thus, by assuming the entire heat load is through the DAM, the modeled temperature of the DAM will be bounding.

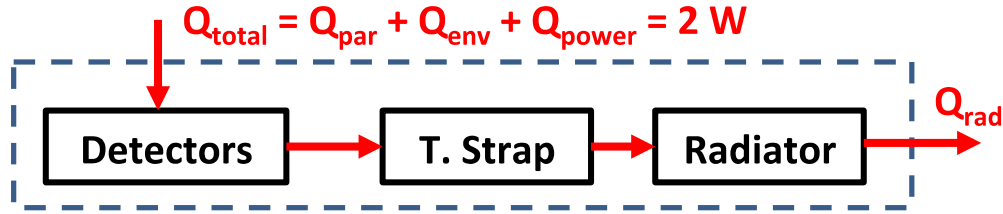


Figure 30: Thermal strap and radiator thermal path diagram

The thermal strap is thermally coupled to the DAM via the DASS. The thermal coupling between the DAM and DASS results from a large surface area attachment, both components are aluminum which has a relatively high thermal conductivity, high joint pressure applied with fasteners, and a thermal gap filler used to reduce microscopic voids in contact. The thermal strap channels heat to the radiator which is body-mounted to the +Y truss panel, as shown in Figure 29. The thermal strap is wrapped in MLI on all exterior surfaces and is not thermally coupled to other parts of the REXIS TCS. The radiator is mounted via low conductivity standoffs to the +Y panel. Furthermore, its backside is covered in MLI to minimize the radiative coupling to the +Y truss panel. Given that the temperature of the truss panel is predicted to be only a few degrees warmer than the radiator in the point TCS design in Chapter 4, it is assumed that the radiator is thermally isolated from other parts of the REXIS TCS system, except for its physical connection with the thermal strap. While isolated radiator assumption is an assumption based on the point design and not the optimal design, the radiator size is restricted by the 20 x 40 cm (in the xz-plane) REXIS design envelope. No radiator within the design space could drive a large enough temperature difference between the radiator and +Y truss panel to invalidate the isolated radiator assumption. The resulting thermal path in Figure 30 is a serial connection of the detectors, thermal strap, and radiator because the components in the assembly are isolated. The dotted line in Figure 30 represents the boundary to the thermal path. The design solution to the thermal path satisfies $Q_{total} = Q_{rad} = 2 \text{ W}$.

Given the thermal path diagram in Figure 30, a parameter file is generated that completely specifies the physical behavior of the problem. The parameter file captures two components – the thermal strap and the radiator. The thermal strap consists of gauge copper wire and two end fittings that are assumed to have zero thermal resistance. In practice, end fittings

have been designed to have over 95% thermal efficiency. The primary control over the design of the thermal strap is in its length and the total cross-sectional area of the wires. The radiator is a rectangular prism made of aluminum. The thermal strap connects to the backside of the radiator and the front side rejects heat to deep space in the form of radiation. Because the radiator is mounted to REXIS above the instrument deck, the radiator has non-zero view factors to both deep space and the warm instrument deck of the spacecraft. Table 12 shows the design variables for the thermal strap and radiator thermal path and their initial values from the point design in Chapter 4. Figure 31 depicts the parameterization of the design variables, defines the coordinate system for the design variables, and provides examples of several constant parameters for the design optimization. Continuous design variables were chosen that control the geometry of the components to explore the spatial configuration of the thermal path.

Table 12: Design variables in parameter file for thermal strap and radiator thermal path

Design Variable	Symbol	Initial Value	Units
Height of radiator above instrument deck	h_0	5	cm
Radiator width	w	15	cm
Radiator height	h	30	cm
Radiator thickness	t	0.3175	cm
X-coordinate location of thermal strap on radiator	x_{TS}	0	cm
Y-coordinate location of thermal strap on radiator	y_{TS}	5	cm
Cross-sectional area of thermal strap	A_{TS}	0.785	cm ²

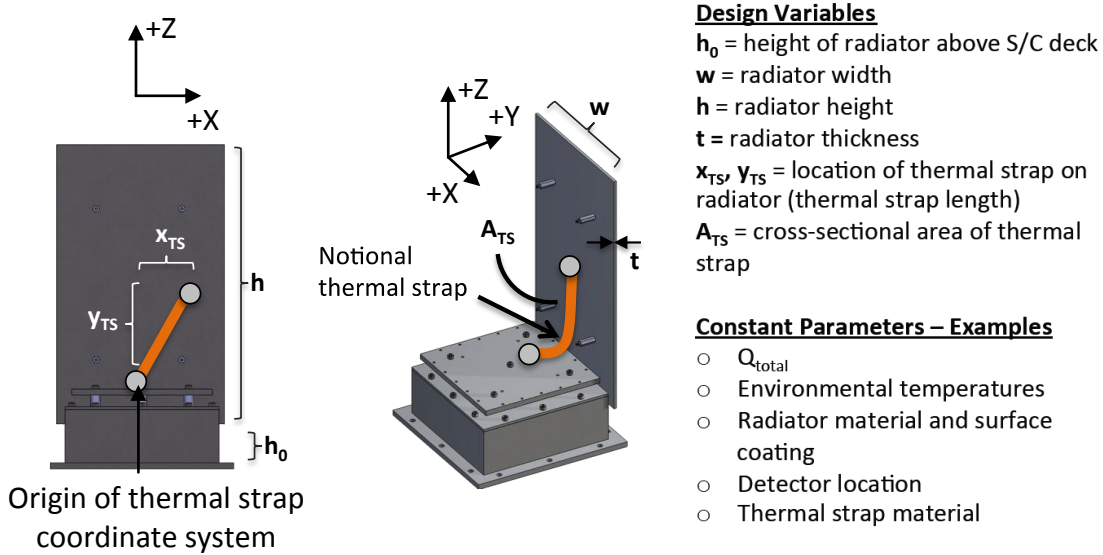


Figure 31: Thermal strap and radiator thermal path parameterization

In Table 12 and Figure 31, the radiator topology is parameterized by width, w , height, h , and thickness, t , and the height above the instrument deck is controlled by the variable h_0 . The thermal strap length is parameterized by the mounting location on the radiator, given by x_{TS} and y_{TS} in the coordinate system defined by Figure 31. The cross-sectional area is specified by the variable A_{TS} . Given values for each design variable, the geometry of the thermal strap and radiator is completely specified. There are many constant parameters in the parameter file. These include, but are not limited to: $Q_{total} = Q_{rad} = 2 \text{ W}$, view factors to the instrument deck and to deep space, and material properties. The complete set of constant parameters can be found in a table provided in Appendix C. From Figure 31, there is now a parameter file that captures the design variables for this thermal path and the constant parameters required to model the system. The parameter file is input into the thermal path model to generate predictions for candidate designs.

5.2 Models of Thermal Path

The models for the thermal strap and radiator thermal path produce both the mass of the assembly and the predicted detector temperature. The primary input to the model is the

parameter file which contains the design variables. The mass calculation uses each component's volume and density to find the total thermal path mass shown by Equation 5.1. In this design optimization, a design that minimizes the radiator mass, m_{rad} , and thermal strap mass, m_{TS} , is desired.

$$m_{total} = m_{rad} + m_{TS} = \rho_{rad}wht + \rho_{TS}L_{TS}A_{TS} \quad (5.1)$$

In Equation 5.1, m_{total} is the total mass of the thermal path, and Table 12 defines the design variable parameters. The terms ρ_{rad} and ρ_{TS} are the densities of the radiator and thermal strap, respectively. The length of the thermal strap, L_{TS} , is found using the distance formula with the design variables x_{TS} and y_{TS} such that $L_{TS} = \sqrt{x_{TS}^2 + y_{TS}^2}$.

The thermal model output is the temperature of the detectors. Because the thermal strap is coupled to the DAM, the base of the thermal strap is assumed to be isothermal with the detector temperature. The heat path through the thermal path is serial as shown in Figure 30. The thermal strap operates in pure conduction, and the radiator operates in both conduction and radiation. The model of each component is shown graphically in Figure 32.

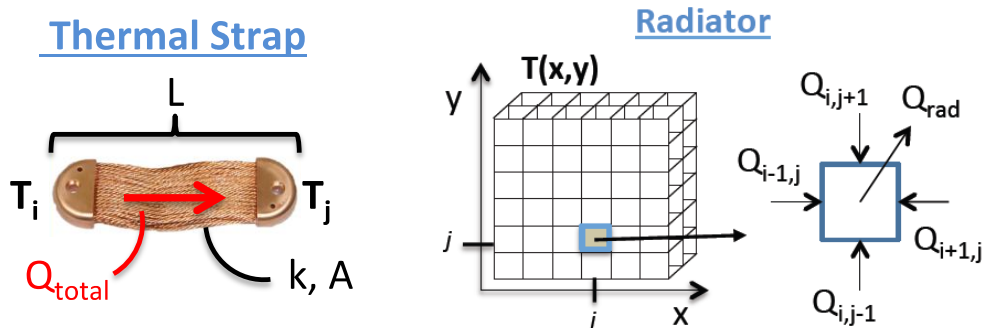


Figure 32: Thermal strap and radiator thermal model

To model the physics of the thermal strap, a 1-D conduction approximation is used as shown in Figure 32. Two nodes, one on the DASS (which is assumed to be the same temperature as the detectors) and one at the radiator, are placed to measure the thermal strap temperature

between the nodes. The thermal resistance between the nodes is equivalent to the thermal resistance developed in Chapter 2 using the 1-D conduction equation. The thermal resistance is a function of the thermal strap length, cross-sectional area, thermal conductivity, and thickness, as shown by Figure 33.

The radiator is uniformly discretized into nodes to capture conduction through the surface of the plate perpendicular to the radiating surface and radiation from the outer surface of the radiator to deep space. Each node, or discretization, conducts to neighboring nodes and emits heat to space. Figure 32 notionally illustrates the process of uniformly dividing a radiator into nodes and examining the heat flow contributions for each node. The conduction between nodes is governed by the 1-D heat conduction equation (Equation 2.7), and the radiation to space is governed by the Stefan-Boltzmann Equation (Equation 2.8). Both governing equations are shown in Figure 33.

Conduction	Radiation
$Q_{\text{cond}} = (T_i - T_j) / R$ <p>where $R = L/kA$</p> <p>$R \sim$ resistance $L \sim$ length of flow $k \sim$ thermal conductivity $A \sim$ cross-sectional area</p>	$Q_{\text{rad}} = \sigma \epsilon A F_{i-j} (T_i^4 - T_j^4)$ <p>$\sigma \sim$ Stefan-Boltzmann constant $\epsilon \sim$ emissivity $A \sim$ surface area $F_{i-j} \sim$ view factor</p>

Figure 33: Thermal model governing equations definition

Equation 5.2 shows the output for the thermal model of the thermal strap and radiator assembly – the detector temperature. The maximum temperature value on the radiator corresponds to the back surface where the thermal strap is mounted. From this maximum temperature, the temperature of the detectors is derived using the 1-D conduction model of the thermal strap.

$$T_{\text{detectors}} = T_{\text{rad,max}} + Q_{\text{total}} R_{TS} = T_{\text{rad,max}} + Q_{\text{total}} \left(\frac{L_{TS}}{k_{TS} A_{TS}} \right) \quad (5.2)$$

In Equation 5.2, R_{TS} is the thermal resistance of the thermal strap. L_{TS} is the thermal strap length first defined in Equation 5.1, k_{TS} is the thermal strap conductivity, and A_{TS} is the thermal strap cross-sectional area which is a design variable defined in Table 12. Q_{total} is the total heat load to be dissipated by the radiator where $Q_{total} = Q_{rad} = 2$ W. The maximum radiator temperature, $T_{rad,max}$, is located where the thermal strap mounts to the radiator. In order to predict the temperature of the detectors, $T_{detectors}$, for a prescribed design, a radiator thermal model is used to find $T_{rad,max}$.

By summing the conduction, radiation, and thermal strap loading terms for each radiator node, a system of nonlinear equations is formulated to model the thermal behavior of the radiator. The solution to the system of equations is the steady state temperature distribution of the radiator. Equation 5.3 shows the summation of heat transfer terms for each node of the radiator. The state vector for the thermal radiator model is the vector of node temperatures, \mathbf{T}_{rad} . For the simulations in this chapter, each node was initially set to 300 K. The i^{th} and j^{th} temperatures in Equation 5.3 are members of the temperature vector, \mathbf{T}_{rad} , where Equation 5.3 is written for the i^{th} node with neighbors $j = 1-4$. The solution to the system of nonlinear equations determines the steady state temperatures of each node on the radiator, \mathbf{T}_{rad} . Equation 5.4 shows that the maximum radiator temperature value is recorded as $T_{rad,max}$ once Equation 5.3 is solved.

$$\sum Q_{cond} + Q_{rad} + Q_{TS} = \sum_{j=1}^4 \frac{T_i - T_j}{R} + \sigma \varepsilon A F_{deck} (T_i^4 - T_{deck}^4) = 0 \quad (5.3)$$

for each i^{th} node, where

$$Q_{TS} = Q_{total} / N_{TS}$$

$$T_{rad,max} = \max(\mathbf{T}_{rad}) \quad (5.4)$$

In Equation 5.3, Q_{cond} and Q_{rad} are defined by Figure 33. Q_{TS} is the thermal strap heat loading term for each node if the node is collocated with the thermal strap mounting location on the

radiator. Because the thermal strap end fitting spans multiple radiator nodes, Q_{TS} is a fraction of the total heat load, Q_{total} , where N_{TS} is the number of radiator nodes that are in contact with the thermal strap end fitting. Equation 5.3 is the thermal model of the radiator – the conductive and radiative heat flows are captured and functionally dependent on the design variables and constant parameters. To find the final node temperatures on the radiator, T_{rad} , in Equation 5.3, the MATLAB command ‘fsolve’ was implemented to solve the system of nonlinear equations using the default Trust-Region Dogleg Method [29]. The goal of ‘fsolve’ is to find a set of T_{rad} such that the system equations are zero. With T_{rad} known and Equation 5.4 to find $T_{rad,max}$, the temperature of the detectors can be calculated from Equation 5.2.

To solve the system, a similar code structure was developed to that of Figure 23 for a nonlinear system in steady state conditions. The system of equations corresponding to each node is solved exactly once. A linear model using the resistor network framework established in Chapter 2 was also constructed to predict temperatures for the radiator. However, the linearized framework does not explicitly allow for view factors to other warm objects such as the spacecraft deck because the radiation to deep space assumption (where deep space is assumed 0 K) was used during the linearization. The choice to include the height of the radiator above the instrument deck precluded the use of the linearized model in producing the final results in this chapter. The 3-D resistor network model for the radiator is provided in Appendix D. The nonlinear model was selected as the model to generate results in this case study because it enables view factors to the spacecraft deck. The radiator view factors impact the Q_{rad} term in Equation 5.3 because they are part of the Stefan-Boltzmann Equation as shown in Figure 33. The view factor is a statement of how much radiation leaving one geometrical surface is incident on another. In the nonlinear model, each node in the 20 x 40 cm radiator design envelope is assigned a view factor based on the discretization size and field of view to the instrument deck. The view factors are computed once prior to running the model using the known radiator design envelope and instrument deck geometry [17]. The radiator nodes are assigned view factors based on where the node is located in the radiator design envelope. For more information on the code for the nonlinear model and its code structure, see Appendix C.

To summarize, each time the parameter files is updated in the collective thermal design optimization process, the models are used to generate a mass estimate, m_{total} , and temperature

prediction, $T_{\text{detectors}}$, for the thermal path. In this study, the mass of the thermal strap and radiator are approximated using the densities and volumes of the components. The temperature of the detectors is predicted using a nonlinear model of the thermal strap in conduction and the radiator in both conduction and radiation. The corresponding linearized model following the development in Chapter 2 is given in Appendix D.

5.3 Definition of Figures of Merit

The FOMs are used to evaluate a candidate design using the predictions from the mass model and thermal model. This case study features a thermal path with the REXIS thermal strap and radiator that comprises 80% of the TCS mass and drives the steady-state detector temperature, as discussed in Chapter 4. The two FOMs for the collective design optimization of this thermal path are shown in Table 13.

Table 13: Thermal strap and radiator FOMs

FOM	Symbol	Units	Type
Mass	m_{total}	kg	Objective
Detector Temperature	$T_{\text{detectors}}$	$^{\circ}\text{C}$	Constraint

Because there is a requirement specifying the upper temperature limit on the detector operating temperature, the thermal performance criteria must be satisfied – not optimized – in the context of the REXIS system. The design optimization requirement is preset with 5 $^{\circ}\text{C}$ of margin to the actual REXIS detector operational requirement shown in Table 8. The optimizer must select a design where the detector operates at less than or equal to -60 $^{\circ}\text{C}$. The minimum mass design required to satisfy the detector temperature requirement is desired. Qualitatively, the mass of the thermal path is the objective of the design subject to the constraint that the detector temperature requirement must be satisfied.

5.4 Optimization Problem Formulation

Formulation of the optimization problem is the last step before the design optimization process is implemented. The optimization is formulated as a single objective constrained optimization problem. Chapter 3 outlines common optimization algorithm selection criteria. The selection criteria for this case study are shown in Table 14.

Table 14: Optimization algorithm selection criteria

Criteria	Value
Number of Design Variables	7
Type of Design Variables	Continuous
Linearity of Problem	Nonlinear
Constraints	Inequality, side bounds
Initial Solution	Provided, feasible

In Table 14, all design variables are documented as continuous and the problem is nonlinear with both constraints and bounds to the design variables. SQP is selected as the gradient-based optimization algorithm to solve the single objective problem. The formulation for the optimization algorithm for the thermal strap and radiator case study is shown in Equation 5.5. The objective function seeks to minimize the total mass of the radiator and thermal strap assembly (Equation 5.1), and the primary constraint to the optimization is the detector temperature (Equation 5.2), $T_{detectors} \leq -60$ °C. For the structure of the optimization formulation within the code, see Appendix C. The nonlinear inequality constraint is given by $g(\mathbf{x}, \mathbf{p})$, and there are do not exist any nonlinear equality constraints in this problem so $h(\mathbf{x}, \mathbf{p}) = 0$.

$$\min J(\mathbf{x}, \mathbf{p}) \quad s. t. \quad \mathbf{g}(\mathbf{x}, \mathbf{p}) \leq 0 \text{ and } \mathbf{h}(\mathbf{x}, \mathbf{p}) = 0 \quad (5.5)$$

$$x_{i, LB} \leq x_i \leq x_{i, UB} \quad (i = 1, \dots, N) \quad \text{and} \quad \mathbf{x} \in S \quad \text{where}$$

$$J(\mathbf{x}, \mathbf{p}) = m_{total} = m_{TS} + m_{rad}$$

$$g(\mathbf{x}, \mathbf{p}) = T_{detectors} + 60 \leq 0$$

$$h(\mathbf{x}, \mathbf{p}) = 0$$

5.5 Results

The collective thermal design optimization process was implemented for the REXIS thermal strap and radiator thermal path. First, results are presented that explain the design solution, including its mass and performance characteristics. Second, a comparison is made between results from the collective thermal design optimization process and results from implementing the design of this thermal path where components are considered in isolation. The former is shown to have a significantly lower mass design solution. Finally, a Pareto frontier for the thermal path is constructed that allows for easy visualization for how mass directly trades with detector temperature.

An optimal design solution was found, and its mass properties are given in Table 15. The small REXIS total heat load and good radiator view factors to deep space led to a total mass much less than half a kilogram. The total thermal path mass is comprised approximately of 1/3 thermal strap mass and 2/3 radiator mass. That the optimal radiator is more massive than the thermal strap is an intuitive result because the radiator physically removes heat from the REXIS TCS while the thermal strap only serves to transfer heat from one component to another. While the heat transfer through the thermal strap must be done efficiently, there are diminishing returns once it reaches a certain cross-sectional area. By examining Equation 5.2, as the thermal strap resistance, R_{TS} , approaches zero, the detector temperature approaches the maximum radiator temperature. Thus, continuing to increase the cross-sectional area of a thermally efficient strap will only marginally decrease the detector temperature.

Table 15: Design solution thermal strap and radiator masses

Component	Mass (g)
<i>Thermal strap</i>	76.3
<i>Radiator</i>	138.2
<i>Total</i>	214.5

The design variables values that yield the design solution in Table 15 are shown in Figure 34 and Table 16. In Figure 34, the values are shown graphically, relative to their bounds in the optimization, because it is a more intuitive way of drawing conclusions from the information. The same coordinate system definition shown in Figure 31 of the design variables is also shown in Figure 34 for completeness.

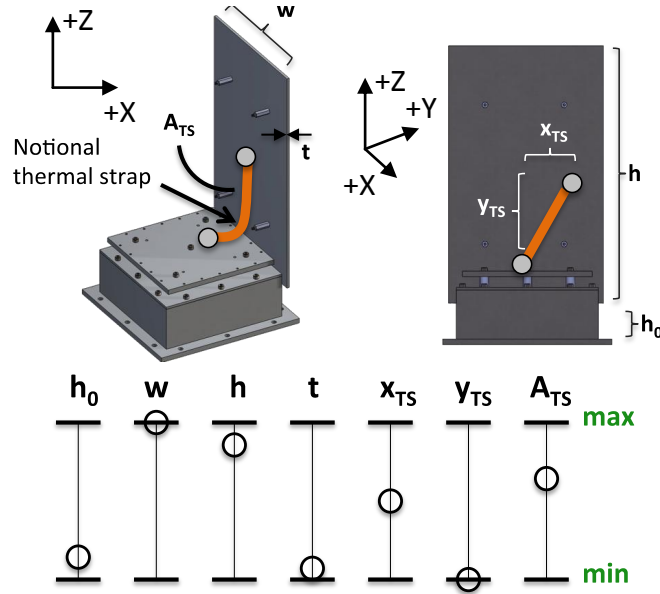


Figure 34: Design variable values for design solution of thermal strap and radiator thermal path (numerical values in Table 16)

Table 16: Numerical design variable values for optimal thermal path solution

Design Variable	Symbol	Optimal Value	Lower Bound	Upper Bound	Units
Height of radiator above instrument deck	h_0	3	0	20	cm
Radiator width	w	20	10	20	cm
Radiator height	h	33	20	40	cm
Radiator thickness	t	0.08	0.05	1	cm
X-coordinate location of thermal strap on radiator	x_{TS}	0	-10	10	cm
Y-coordinate location of thermal strap on radiator	y_{TS}	0	0	20	cm
Cross-sectional area of thermal strap	A_{TS}	1.35	0.00785	3.89	cm ²

An important advantage to the collective thermal design optimization process is that key design trades are implicitly considered by the optimizer. Three key design trades for the thermal strap and radiator assembly are shown below:

- Radiator thickness versus surface area
- Thermal strap mounting location on the radiator versus thermal strap length
- Radiator height above the instrument deck versus thermal strap length

Each of these design trades uses the physics of the model to decide the best way to allocate mass in the geometry of the components. These three design trades are important examples of design trades implicitly captured by the collective thermal design optimization process that are not necessarily straightforward in the traditional, manual thermal design process discussed in Chapter 1.

From Figure 34 and Table 16, conclusions may be drawn about key design trades. The first trade considers the thickness of the radiator versus the surface area used to reject heat to space. The width was right at and the height was very near the maximum allowable value, but the thickness of the radiator was very near its minimum allowable value. Thus, the design

solution radiator is a large, thin plate. This result means that it is more important to have a large surface area to reject heat to space instead of having a thicker, more isothermal radiator. If the emissivity of the radiating plate were substantially lower, the radiator thickness would be a more dominating trend.

The second trade captures the effect that a centrally mounted thermal strap on the radiator will make the radiator more isothermal. However, the central mounting location requires a longer thermal strap that increases both mass and thermal resistance. The optimal solution balances these two competing effects. The solution thermal strap is mounted along the y-axis, the centerline of the radiator, at the minimum displacement from the x-axis. This result is intuitive because the radiator view factors are symmetric. If the view factors were significantly asymmetric, the optimal mounting position of the thermal strap would likely be displaced from the y-axis. The mounting location of the thermal strap on the x-axis means that a very short thermal strap is physically preferred. The increased thermal resistance and mass of the thermal strap required for a central radiator mounting location was too costly to offset the performance benefit gained by have a more isothermal radiator.

The third example design trade captures the competing effects between the increased radiator height above the instrument deck that offers better view factors to space and the increased thermal strap length required to accommodate the change. The optimizer implicitly balances the view factor improvements with the decreased conduction through the performance strap to optimize the performance-to-mass ratio in this design trade. The height of the radiator above the instrument deck was very near the minimum value. The small h_0 value indicates that the increased radiator performance achieved by moving the radiator further from the instrument deck was offset by the increase in thermal strap length necessary to accommodate the change. The qualitative evaluation of key design trades such as these three is an important analysis step in understanding the physical behavior of the design solution.

Using the coordinate system established in Figure 31 for the thermal strap mounting location on the radiator, Figure 35 shows the temperature distribution of the optimal radiator. The temperature map is a visual snapshot of the design during operation in Orbit Phase B. The warmest region of the radiator is where the thermal strap is mounted. Heat spreads radially across the entire radiator. As a result, the top portion of the radiator furthest from the thermal

strap is the coldest, least efficient area of the radiator with respect to heat rejection. For the optimal thermal strap and radiator design, the temperature of the detectors is $-60\text{ }^{\circ}\text{C}$. Because the system, operating in a warmer thermal environment, has been mass-optimized to meet the detector temperature requirement, it follows that the design solution *just* satisfies the requirement so that no excess mass is used inefficiently in the design.

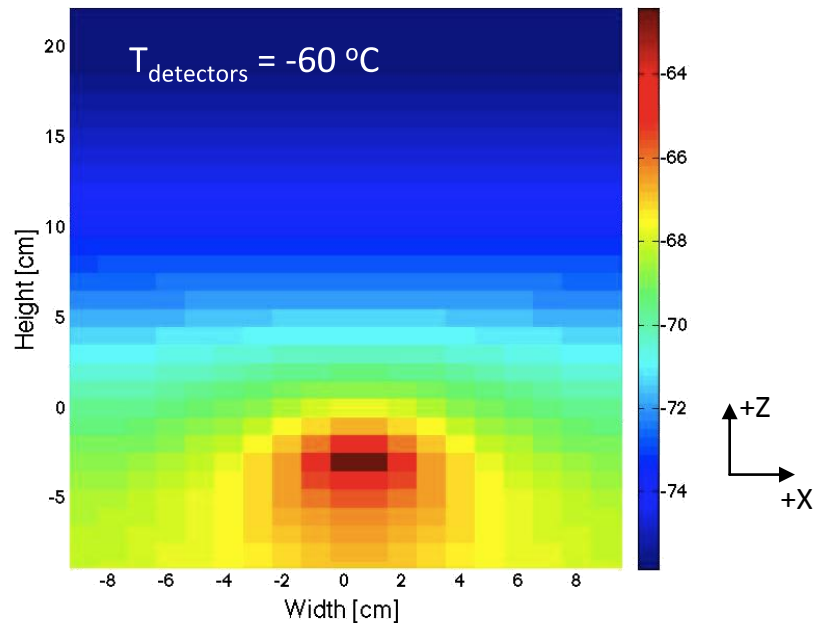


Figure 35: Radiator temperature distribution [$^{\circ}\text{C}$]

The sensitivity of the thermal path mass to small changes in the design variables shows the slope of the objective function in each design variable direction. A mass sensitivity analysis for the design solution of the thermal strap and radiator thermal path is shown in Figure 36. Using a small forward difference in the nominal value of the design variables and normalizing, the impact to the total thermal path mass is observed. In Figure 36, the temperature constraint is not captured in the sensitivities shown.

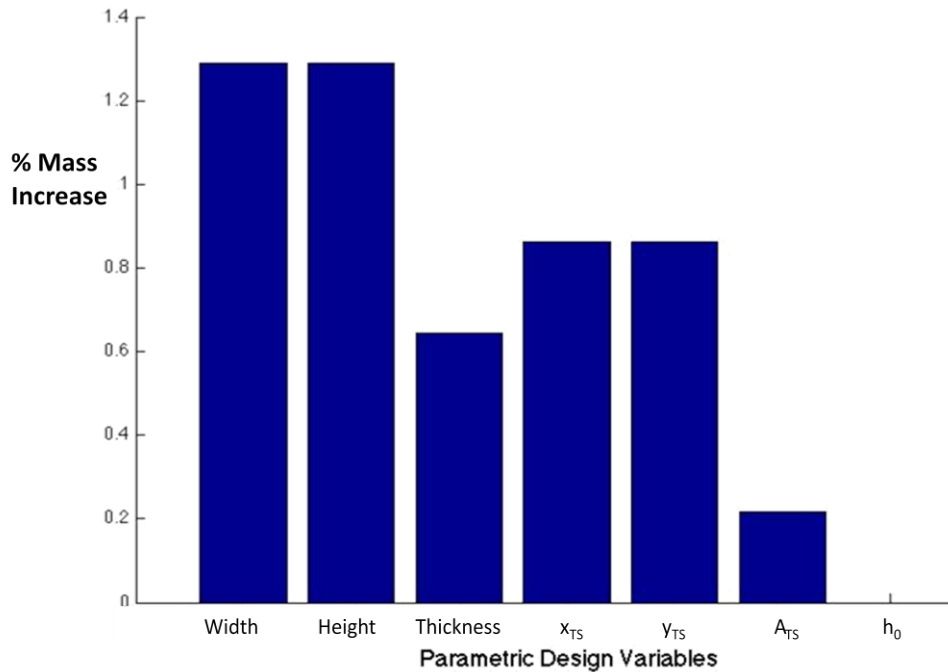


Figure 36: Mass sensitivity analysis at optimal design

Figure 36 verifies that the design solution is at least locally optimal: all of the slopes with respect to mass are greater than or equal to zero, meaning any small change to the design variables increases mass. In order of significance to a mass increase, the radiator width and height, thermal strap mounting locations, radiator thickness, and thermal strap cross-sectional area all increase the mass of the thermal path with a small positive perturbation in their values. Shrinking the width or height of the radiator is the best option if less mass (at the cost of decreased performance) is desired. The mass sensitivity to the height above the radiator deck is zero because the variable h_0 does not control component geometry – only the spatial location of the radiator above the instrument deck.

Figure 37 shows the detector temperature sensitivity analysis at the optimal design. Using a small forward difference in the nominal value of the design variables and normalizing, the impact to the detector temperature is observed. The results for the radiator thickness and height are intuitive – increasing the thickness makes the radiator maximum temperature decrease because the radiator becomes more isothermal and increasing the height increases the total surface area. While the thickness provides the best performance improvement, the design

solution shown in Figure 34 suggests that the radiator with the largest performance-to-mass ratio is still relatively thin. The temperature sensitivity to the radiator width shows that if width increases, the detector temperature increases. The temperature increase is due to the radiative coupling between the radiator and the instrument deck. In general, the portions of the radiator surface closer to the instrument deck are less efficient than portions further from the instrument deck because their view factor to the warm deck is larger. Thus, increasing the width of the radiator increases the amount of radiator surface area closely exposed to the instrument deck.

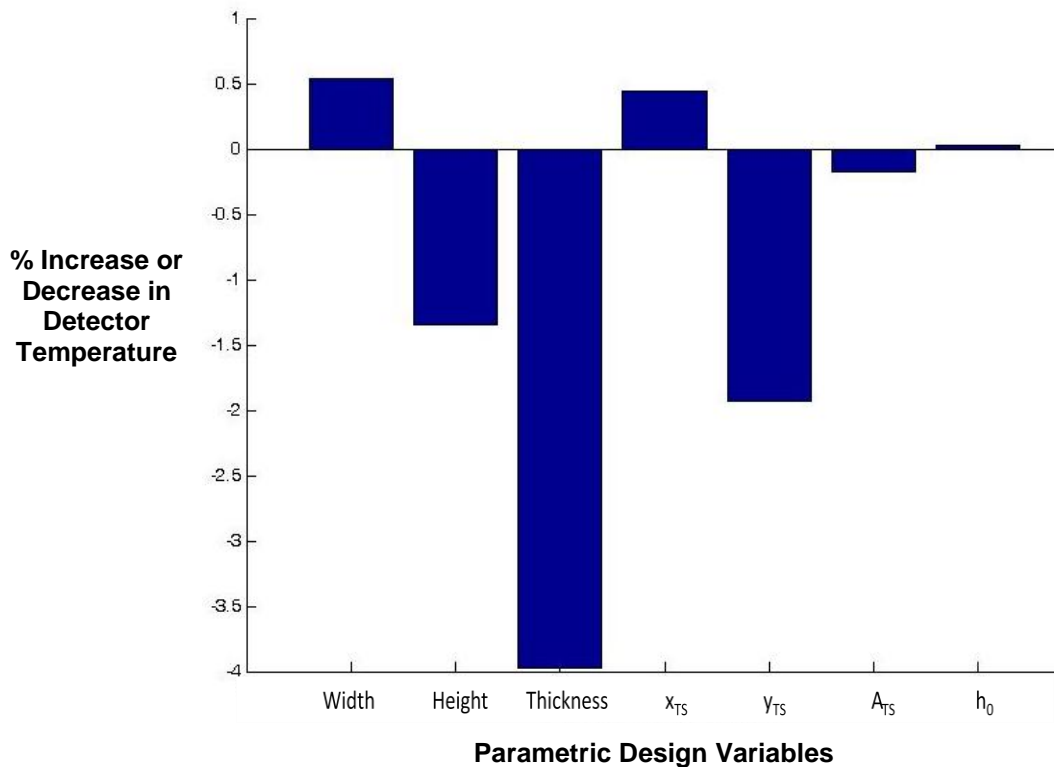


Figure 37: Detector temperature sensitivity analysis at optimal design

In Figure 37, the detector temperature sensitivities of the thermal strap suggest that its mounting location dictated by y_{TS} is the most critical thermal strap variable. The cross-sectional area marginally lowers the detector temperature. Increasing the x_{TS} coordinate to displace the end fitting of the thermal strap from the centerline raises the temperature because the temperature distribution becomes asymmetric. Examining the temperature sensitivity to the height above the instrument deck, h_0 , the detector slightly increases for a small increase in h_0 . At first this is counterintuitive – if the radiator view factors improve, the detector temperature should decrease.

However, the increase in detector temperature is due to the relative shift in the thermal strap mounting location as a result of increasing the height of the radiator above the instrument deck. The radiator is less isothermal because of the increase in h_0 .

The key point of this research is to demonstrate that mass savings is available using this methodology over the traditional thermal design process. A common feature of the traditional thermal design process and current research focuses on design optimization at the component level. That is, a component is often design-optimized in isolation from the rest of the TCS. A component-level optimization was performed in similar fashion to Hull, et al. [4]. Mass results from this traditional thermal design procedure are compared to this thesis' methodology in Table 17. In both cases, the detector temperature is $-60\text{ }^\circ\text{C}$ because $T_{\text{detectors}} \leq -60\text{ }^\circ\text{C}$ is a constraint to the optimization that must be satisfied by each optimal design.

Table 12: Comparison of collective to component-level thermal design optimization

	Component Optimization	Collective Optimization
<i>Thermal Strap</i>	241.4 g	76.3 g
<i>Radiator</i>	99.1 g	138.2 g
Total	340.5 g	214.5 g

37% mass reduction

To perform the design optimization at the component level shown in Table 17, the radiator was optimized first, as in Hull, et al. [4]. Radiators are often sized early in thermal design because their size drives TCS performance and mass. It was assumed that the thermal strap was mounted in the center of the radiator and a nominal cross-sectional area for the thermal strap was selected. Once the radiator was optimized, the thermal strap was also optimized in isolation – both its cross-sectional area and mounting location on the radiator were design variables in the second optimization. Equation 5.6 shows the optimization problem formulation for the component optimization in Table 17. The optimization is run twice to optimize the design of each component individually – first for the radiator and second for the thermal strap. As in

collective optimization, SQP was selected as the gradient-based optimization algorithm to solve both single objective problems.

$$\min J(\mathbf{x}, \mathbf{p}) \quad s. t. \quad \mathbf{g}(\mathbf{x}, \mathbf{p}) \leq 0 \text{ and } \mathbf{h}(\mathbf{x}, \mathbf{p}) = 0 \quad (5.6)$$

$$x_{i, LB} \leq x_i \leq x_{i, UB} \quad (i = 1, \dots, N) \quad \text{and} \quad \mathbf{x} \in S \quad \text{where}$$

$$J(\mathbf{x}, \mathbf{p}) = m = \begin{cases} m_{rad} \\ m_{TS} \end{cases}$$

$$g(\mathbf{x}, \mathbf{p}) = T_{detectors} + 60 \leq 0$$

$$h(\mathbf{x}, \mathbf{p}) = 0$$

In Equation 5.6, $J(\mathbf{x}, \mathbf{p})$ is the objective function of the component optimization where mass minimization is desired. $J(\mathbf{x}, \mathbf{p})$ is equal to the radiator mass for the first component-level optimization and the thermal strap mass for the second component-level optimization. The nonlinear inequality constraint, $g(\mathbf{x}, \mathbf{p})$, is identical to collective optimization because the detector temperature requirement must be satisfied by the design. The net effect of performing the collective thermal design optimization process is a 37% mass reduction over the component-level optimization of the same thermal path.

The traditional, component-level optimized design is more massive because the interaction between the components is not physically represented in the design process. Not capturing the spatial and functional relationship between components introduces inefficiencies into the design of the thermal path. Because the radiator is designed first under an optimistic assumption that the thermal strap is mounted in the center, the solution radiator is thinner than its counterpart from collective optimization. Consequently, a performance burden is placed on the thermal strap design to meet the detector temperature requirement and results in a thermal strap with substantially larger cross-sectional area. Collective optimization of an entire thermal path captures component interactions and expands the design space.

In the collective thermal design optimization process, performance is traded with mass to find the best design with respect to the FOMs. In this case study, a single-objective constrained

optimization problem formulation was used to find the optimal mass system subject to a performance constraint. However, in many cases it is practical to formulate the optimization as a multi-objective problem that directly trades performance with mass. Pareto frontiers allow engineers to visualize how allocations between FOMs are traded in the system design. By discretely changing the value of the detector temperature in this case study, a Pareto frontier for the design of the thermal strap and radiator thermal path was constructed and is shown in Figure 38.

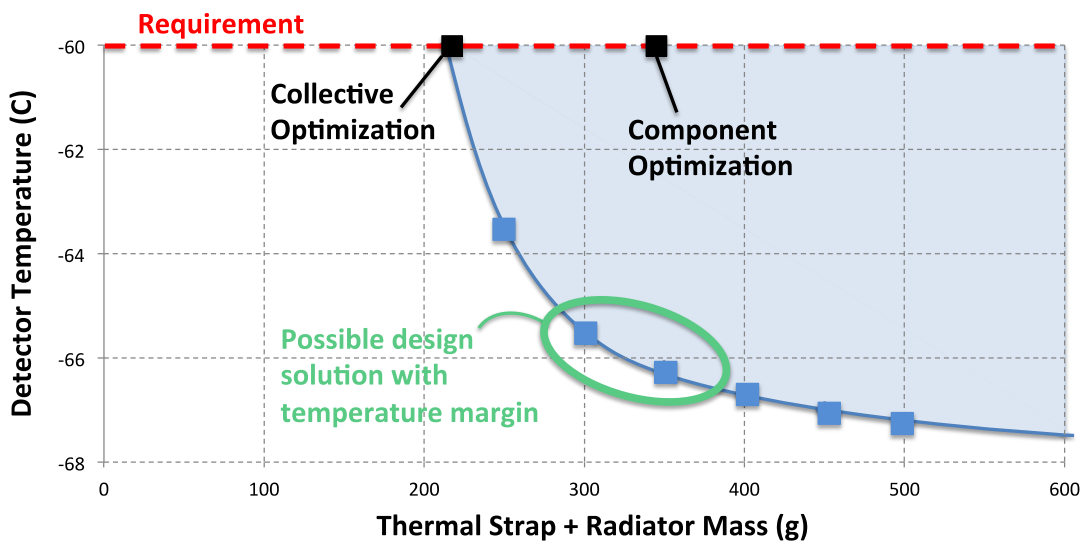


Figure 38: Pareto frontier of thermal strap and radiator thermal path of total mass versus detector temperature

In Figure 38, the detector temperature requirement with margin is shown at -60°C . The total thermal path mass is plotted against the detector temperature, and the results from Table 15 are identified on the diagram. The component-level optimization is inside the efficiency curve for this thermal path. This Pareto frontier guides the evaluation of non-dominated designs created by the collective optimization process. Figure 38 is a tool that can be used to intelligently allocate margin for the system. For the thermal path in this case study, there is a pronounced *knee* in the curve of Figure 38. The knee suggests a possible design solution with additional margin to the requirement that is relatively cheap with respect to mass. At the knee in the Pareto front, there is a significant change in the slope of the detector temperature as the total thermal

path mass increases. For example, by increasing the mass of the thermal path about 100 grams to the knee of the curve, approximately 6 °C of margin is gained to the -60 °C optimization requirement while remaining Pareto-efficient. An additional 100 grams will yield only 1 °C more margin to the detector temperature requirement. Ultimately, this Pareto frontier demonstrates that the methodology introduced in Chapter 3 yields design solutions with higher performance-to-mass ratios and practical means for understanding the physical behavior and performance of the thermal path.

5.6 Summary

The collective thermal design process was implemented on the REXIS thermal strap and radiator thermal path. The objective of the optimization was to find the minimum mass design subject to the REXIS detector temperature constraint. Compared to the design solution found using the traditional component-level design optimization, the collective thermal design optimization offered a 37% mass reduction of the total thermal path mass for this case study. This chapter demonstrates that collective thermal design optimization can improve the performance-to-mass ratio of a thermal path when compared to traditional thermal design methods.

Chapter 6 – Conclusion

6.1 Thesis Summary

TCS design optimization is critical to maximize the performance or minimize the resource consumption of a system. The traditional notion of the TCS is that it does not significantly drive system performance or resource consumption. There are several factors relevant in many spacecraft systems that invalidate this assumption. In these systems, the performance and resource consumption are driven by the TCS. Examples of such systems are JWST and REXIS. TCS design optimization ensures that system resources, including mass, volume, and power, are used efficiently.

This thesis introduces an approach to improve the thermal design process. Traditional methods involve experts making key component selection and sizing decisions for a system that is largely pre-determined by other subsystems, such as structures and payload. The net effect is that TCS are point designs that are neither performance- nor resource-optimal. The collective thermal design optimization process introduced in this thesis provides a methodology for optimizing the design of critical thermal paths. Important procedural elements of the collective thermal optimization process include a parameterization of a thermal path that captures component interactions with each other and the spacecraft, thermal path model(s) that accurately predict performance and properties for a candidate design, and a properly formulated optimization algorithm that updates the design variables in the parameter file. Output of the collective thermal design optimization process is the final thermal path design that is optimal with respect to the FOMs.

Chapters 4 and 5 use REXIS as a case study for the implementation of the collective thermal design optimization process. To implement the process, a point design, thermal model, and identification of the thermal paths within the TCS are required. Chapter 4 demonstrates this process to identify the critical thermal path for REXIS. Sensitivity analysis was used to assist in identifying the thermal strap and radiator assembly within the telescope truss structure as the critical REXIS thermal path. The focus of Chapter 5 was to use this critical REXIS thermal path as a case study for the collective thermal design optimization process. Mass was the objective

function and the REXIS detector operational temperature was the thermal performance constraint. The results show a 37% reduction in mass of the thermal strap and radiator assembly over the component-level optimization method. Using a Pareto frontier to visualize the improvement for this case study, the collective thermal design optimization process was shown to generate more Pareto-efficient design solutions than component-level optimization when trading mass and thermal performance. The primary reason for this improvement is that capturing component interactions with each other and the system broadens the design space for feasible solutions considered by the optimizer.

6.2 Contributions

This thesis introduces the collective thermal design optimization process, which is an improvement to point designs and designs achieved via component-level optimizations. The improvement lies in capturing a larger design space of feasible solutions and the process allows the optimizer to implicitly evaluate key physical design trades within the system. The net effect is a thermal path solution that is either performance- or resource-optimal.

In addition to improving the thermal design process, this thesis documents the efforts of REXIS thermal modeling. The preliminary modeling and design in Chapter 4 and the Thermal Desktop model documented in Appendix E are snapshots in time of REXIS thermal analysis. Chapter 4 demonstrates the modeling work done in preparation for the System Definition Review of REXIS, and Appendix E documents the thermal model presented at the REXIS Preliminary Design Review.

6.3 Future Work

Preliminary results in implementing the collective thermal design optimization process on spacecraft systems shows the potential for increasing a system's overall performance or decreasing its reliance on resources. Using the outcome of the REXIS thermal strap and radiator thermal path case study presented in Chapter 5, future work that will advance the methodology includes:

- Multi-objective design optimization that captures multiple FOMs in the objective function

- Optimize to satisfy not only thermal but interdisciplinary requirements, e.g., structural requirements
- Generalize the parameterization framework to be extensible for any thermal path
- Implement on multiple thermal paths simultaneously
- Implement on a thermal path that uses active thermal control components
- Implement in the context of high fidelity thermal design

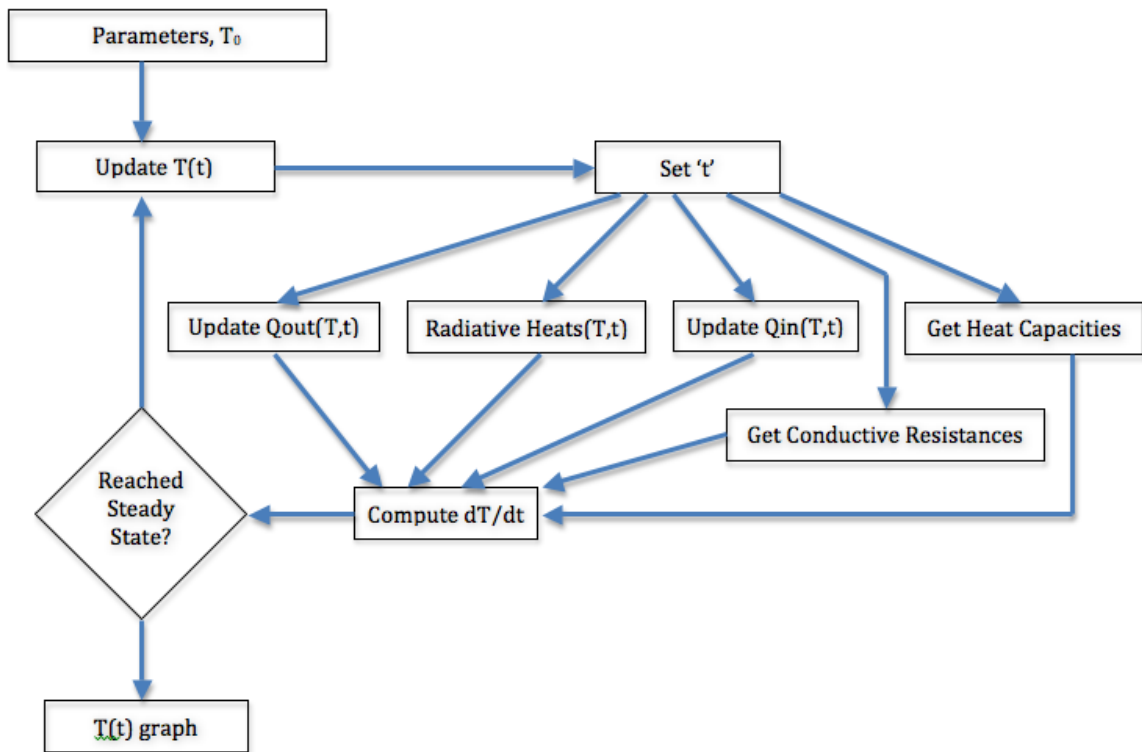
The case study presented in Chapter 5 reflects efforts of preliminary thermal design of a passive system under a single temperature requirement. However, thermal design is inherently interdisciplinary. The design of a thermal component is tightly coupled with other subsystems – particularly those who share ownership of the component, i.e., a spacecraft structure. Inclusion of interdisciplinary requirements will ensure all system requirements are satisfied by a thermal path design. The future work items presented here will demonstrate the extensibility of the collective thermal design optimization process to any spacecraft system and the robustness of its processes. The TCS is often an understated important piece to a system’s performance and consumption of resources. The design optimization technique presented in this thesis improves design efficiency with respect to performance and resource consumption.

Chapter 7 – References

- [1] "Space transportation costs: Trends in price per pound to orbit 1990 - 2000," Futron Corporation, 2006.
- [2] J. Saleh, D. Hastings and D. Newman, "Spacecraft design lifetime," *Journal of Spacecraft and Rockets*, vol. 39(2), pp. 244-257, 2002.
- [3] J. Gardner and e. al., "The James Webb Space Telescope," in *Springer*, 2006.
- [4] P. Hull, K. Kittredge, M. Tinker and M. SanSoucie, "In-space radiator shape optimization using genetic algorithms," *NASA Marshall Space Flight Center*.
- [5] A. Cuco, F. de Sousa, V. Vlassov and A. da Silva Neto, "Multi-objective design optimization of a new space radiator," *International Conference on Engineering*, 2008.
- [6] R. Naumann, "Optimizing the design of space radiators," *International Journal of Thermophysics*, vol. 25, pp. 1929-1940, 2004.
- [7] L. Sousa, V. Vlassov and F. Ramos, "Generalized extremal optimization: An application in heat pipe design," *Applied Mathematical Modeling*, vol. 28, pp. 911-931, 2004.
- [8] S. Mukundan, "Structural design and analysis of a lightweight composite sandwich space radiator panel," Vols. Unpublished master's thesis, Texas A&M University, 2003.
- [9] E. Escobar, M. Diaz and J. Zagal, "Design automation for satellite passive thermal control," *The 4S Symposium*, pp. 1-10, 2012.
- [10] R. Galski, F. de Sousa, F. Ramos and I. Muraoka, "Spacecraft thermal design with the generalized extremal optimization algorithm. Inverse Problems," *Design and Optimization Symposium*, 2004.
- [11] I. Muraoka, R. Galski, F. de Sousa and F. Ramos, "Stochastic spacecraft thermal design optimization with low computational costs," *Journal of Spacecraft and Rockets*, vol. 43, 2006.
- [12] N. Chari, "Spacecraft thermal design optimization," Vols. Unpublished master's thesis, University of Toronto, 2009.
- [13] V. Vlassov, F. de Sousa and W. Takahashi, "Comprehensive of a heat pipe radiator assembly filled with ammonia or acetone," *International Journal of Heat and Mass Transfer*, vol. 49, pp. 4584-4959, 2006.
- [14] J. Wertz, *Space Mission Engineering: The New SMAD*, Microcosm Press, 2011.
- [15] M. Drake, D. Lauretta and O. Team, "OSIRIS-REx Asteroid Sample Return Mission," in *American Geophysical Union*, 2011.

- [16] D. Gilmore, *Spacecraft Thermal Control Handbook*, El Segundo: The Aerospace Press, 2002.
- [17] J. Richmond, "Adaptive Thermal Modeling Architecture for Small Satellite Applications," MIT, Cambridge, 2010.
- [18] "Manufacturing Research Laboratory Nontraditional Manufacturing," Columbia University, 2012. [Online]. Available: <http://www.mrl.columbia.edu/ntm/level2/ch03/html/l2c03s04.html>.
- [19] T. Smith, "Thermal Analysis of PANSAT," Naval Postgraduate School, Monterey, 1997.
- [20] A. B. Alves, "Critical evaluation of direct and iterative methods for solving $Ax=b$ systems in power flow calculations and contingency analysis," *Power Industry Computer Applications*, pp. 15-21, 1999.
- [21] "Radiative Heat Transfer Coefficient," Biber Thermal Design, [Online]. Available: http://www.biberthermal.com/Reference_Links/Thermal_Design_Info/Radiative_heat_transfer_coeffi/radiative_heat_transfer_coeffi.html. [Accessed 2013].
- [22] O. de Weck, "Multiobjective Optimization: History and Promise," *The 3rd China-Japan-Korea Joint Symposium on Optim. of Structural and Mechanical Systems*, 2004.
- [23] R. Marler and J. Arora, "Survey of multi-objective optimization methods for engineering," in *Struct. Multidisciplinary Optimization*, 2004.
- [24] O. de Weck and K. Willcox, "Multidisciplinary System Design Optimization, MIT Open Courseware," Massachusetts Institute of Technology, Cambridge, 2010.
- [25] R. Fletcher, "Practical Methods of Optimization," in *John Wiley and Sons*, 1987.
- [26] J. Kennedy, "Particle Swarm Optimization," *IEEE Conference on Neural Networks*, vol. 4, pp. 1942-1948, 1995.
- [27] S. Kirkpatrick, M. Vecchi and C. Gelatt, "Optimization by simulated annealing," in *Science*, 1983.
- [28] J. Holland, "Adaptation in Natural and Artificial Systems," The University of Michigan Press, Ann Arbor, 1975.
- [29] N. Conn, N. Gould and P. Toint, "Trust-Region Methods," in *MPS/SIAM Series on Optimization*, 2000.

Appendix B: REXIS Reduced-order Model Code



Reduced-order nonlinear model code structure

** Note: this thermal model was used in the context of a REXIS integrated model. Consequently, many of the input parameters are pulled from structures that contain the entire parameter set for REXIS.

Functions

Odefun.m ~ call all input files and contains model to return dT/dt

getMass.m ~ get masses of nodes

getSpecificHeats.m ~ get specific heats of nodes

getInputs.m ~ get parameteric inputs to model

getQin.m ~ get input heats

getQout ~ solve for output heats of model

getRadiativeHeats.m ~ solve for radiative heat transfers in system

getConductiveResistances.m ~ set conductances for system


```

function [Tdot] = odefun(t,T)

% Mass in kg with corresponding node #
[m,rexis] = getMass(rexis);

% Specific Heat Capacities [J/kg-K] with corresponding node #
[Cp,rexis] = getSpecificHeats(rexis);

% Get Resistances
[R,rexis] = getConductiveResistances(rexis);

% Get Qout
[Qout] = getQout(T(2),T(1),T(15),R(23),T(13),T(11),T(9));

%get Qin
[Qin,rexis] = getQin(rexis);

% Define heat outputs [W]
Q_deck = Qout(1); % Heat out from Electronics Box to Deck
Q_rad = Qout(2); % Net Heat radiated out from Radiator to Space, and in from
deck
Q_mask = Qout(3); % Heat radiated out to space from the Mask
Q_tARad = Qout(4); % Truss to Space
Q_tSun = Qout(5); % Truss to Space
Q_tASun = Qout(6); % Truss to Space

% Define heat inputs [W]
Q_CCDin = Qin(1); % Heat dissipated by CCDs
Q_IR_CCD = Qin(2); % Heat in from Asteroid IR Radiation to CCDs
Q_Albedo_CCD = Qin(3); % Heat in from Asteroid Albedo to CCDs
Q_Deck_TrussASun = Qin(4); % Heat in from Deck Radiation to Truss
Q_Sun_TrussSun = Qin(5); % Direct Solar Heat to Sun Truss
Q_Deck_TrussSun = Qin(6); % Heat in from Deck Radiation to Truss
Q_Deck_TrussARad = Qin(7); % Heat in from Deck Radiation to Truss
Q_IR_Mask = Qin(8); % Heat in from Asteroid IR Radiation to Mask
Q_Albedo_Mask = Qin(9); % Heat in from Asteroid Albedo to Mask
Q_EB = Qin(10); % Heat dissipated by Electronics Box

%-----
% Nodes:
% 1- EB
% 2- Radiator
% 3- CCD Package
% 4- DASS
% 5- Thermal Strap
% 6- CCD
% 7- Truss Radiator
% 8- Truss Rad Shield
% 9- Truss Anti-Sun
% 10- Truss ASun Shield
% 11- Truss Sun
% 12- Truss Sun Shield
% 13- Truss Anti-Rad
% 14- Truss ARad Shield
% 15- Mask

```

```

% Define Conductive Paths
Q_EB_DASS = (T(1)-T(4))/R(1);
Q_EB_CCD = (T(1)-T(6))/R(22);
Q_CCD_CCDPack = (T(6)-T(3))/R(2);
Q_CCDPack_DASS = (T(3)-T(4))/R(3);
Q_TStrap_Radiator = (T(5)-T(2))/R(5);
Q_DASS_TStrap = (T(4)-T(5))/R(4);
Q_DASS_TrussASun = (T(4)-T(9))/R(6);
Q_DASS_TrussRad = (T(4)-T(7))/R(7);
Q_DASS_TrussSun = (T(4)-T(11))/R(13);
Q_DASS_TrussARad = (T(4)-T(13))/R(14);
Q_TrussRad_TRadSShield = (T(7)-T(8))/R(9);
Q_TrussRad_TrussASun = (T(7)-T(9))/R(10);
Q_TrussRad_Mask = (T(7)-T(15))/R(11);
Q_TrussRad_Radiator = (T(7)-T(2))/R(8);
Q_TrussRad_TrussSun = (T(7)-T(11))/R(12);
Q_TrussASun_TrussASunSShield = (T(9)-T(10))/R(15);
Q_TrussASun_TrussARad = (T(9)-T(13))/R(17);
Q_TrussASun_Mask = (T(9)-T(15))/R(19);
Q_TrussSun_TrussSunSShield = (T(11)-T(12))/R(16);
Q_TrussSun_TrussARad = (T(11)-T(13))/R(18);
Q_TrussSun_Mask = (T(11)-T(15))/R(21);
Q_TrussARad_TrussARadSShield = (T(13)-T(14))/R(24);
Q_TrussARad_Mask = (T(13)-T(15))/R(20);

% Define Radiative Paths
[radiativeHeats] =
getRadiativeHeats(T(1),T(4),T(6),T(8),T(10),T(12),T(14),T(15));

QR_EB_DASS = radiativeHeats(1);
QR_SunSShield_CCD = radiativeHeats(2);
QR_Mask_CCD = radiativeHeats(3);
QR_ARadSShield_CCD = radiativeHeats(4);
QR_ASunSShield_CCD = radiativeHeats(5);
QR_RadSShield_CCD = radiativeHeats(6);
QR_RadSShield_ASunShield = radiativeHeats(7);
QR_RadSShield_ARadSShield = radiativeHeats(8);
QR_RadSShield_SunSShield = radiativeHeats(9);
QR_RadSShield_Mask = radiativeHeats(10);
QR_ASunSShield_Mask = radiativeHeats(11);
QR_ASunSShield_ARadSShield = radiativeHeats(12);
QR_ASunSShield_SunSShield = radiativeHeats(13);
QR_SunSShield_ARadSShield = radiativeHeats(14);
QR_SunSShield_Mask = radiativeHeats(15);
QR_ARadSShield_Mask = radiativeHeats(16);

%EB
Tdot1 = (- Q_EB_CCD - Q_EB_DASS - QR_EB_DASS + Q_EB - Q_deck)/(m(1)*Cp(1));

%Radiator
Tdot2 = (Q_TStrap_Radiator + Q_TrussRad_Radiator - Q_rad)/(m(2)*Cp(2));

%CCD Package

```

```

Tdot3 = (Q_CCD_CCDPack - Q_CCDPack_DASS) / (m(3)*Cp(3));

%DASS
Tdot4 = (Q_EB_DASS + Q_CCDPack_DASS - Q_DASS_TStrap + QR_EB_DASS -
Q_DASS_TrussRad - Q_DASS_TrussASun - Q_DASS_TrussSun -
Q_DASS_TrussARad) / (m(4)*Cp(4));

%Thermal Strap
Tdot5 = (Q_DASS_TStrap - Q_TStrap_Radiator) / (m(5)*Cp(5));

%CCD
Tdot6 = (Q_EB_CCD - Q_CCD_CCDPack + QR_RadSShield_CCD + QR_SunSShield_CCD
+QR_ARadSShield_CCD + QR_ASunSShield_CCD + QR_Mask_CCD + Q_Albedo_CCD +
Q_IR_CCD + Q_CCDin) / (m(6)*Cp(6));

%Truss Radiator
Tdot7 = (Q_DASS_TrussRad - Q_TrussRad_TRadSShield - Q_TrussRad_Radiator -
Q_TrussRad_TrussASun - Q_TrussRad_TrussSun - Q_TrussRad_Mask) / (m(7)*Cp(7));

%Side Shield Truss Rad
Tdot8 = (Q_TrussRad_TRadSShield - QR_RadSShield_CCD -
QR_RadSShield_ASunShield - QR_RadSShield_ARadSShield -
QR_RadSShield_SunSShield - QR_RadSShield_Mask) / (m(8)*Cp(8));

%Truss Anti-Sun
Tdot9 = (-Q_tASun + Q_DASS_TrussASun + Q_TrussRad_TrussASun -
Q_TrussASun_TrussARad - Q_TrussASun_TrussASunSShield - Q_TrussASun_Mask +
Q_Deck_TrussASun) / (m(9)*Cp(9));

%Truss ASun Side Shield
Tdot10 = (Q_TrussASun_TrussASunSShield - QR_ASunSShield_CCD +
QR_RadSShield_ASunShield - QR_ASunSShield_Mask - QR_ASunSShield_ARadSShield -
QR_ASunSShield_SunSShield) / (m(10)*Cp(10));

%Truss Sun
Tdot11 = (-Q_tSun - Q_TrussSun_TrussSunSShield + Q_DASS_TrussSun +
Q_TrussRad_TrussSun - Q_TrussSun_TrussARad - Q_TrussSun_Mask +
Q_Deck_TrussSun + Q_Sun_TrussSun) / (m(11)*Cp(11));

%Truss Sun Side Shield
Tdot12 = (Q_TrussSun_TrussSunSShield - QR_SunSShield_CCD +
QR_RadSShield_SunSShield + QR_ASunSShield_SunSShield -
QR_SunSShield_ARadSShield - QR_SunSShield_Mask) / (m(12)*Cp(12));

%Truss Anti Rad
Tdot13 = (-Q_tARad - Q_TrussARad_TrussARadSShield + Q_TrussASun_TrussARad -
Q_TrussARad_Mask + Q_TrussSun_TrussARad + Q_DASS_TrussARad +
Q_Deck_TrussARad) / (m(13)*Cp(13));

%Truss ARad Side Shield
Tdot14 = (Q_TrussARad_TrussARadSShield - QR_ARadSShield_CCD +
QR_RadSShield_ARadSShield + QR_ASunSShield_ARadSShield +
QR_SunSShield_ARadSShield - QR_ARadSShield_Mask) / (m(14)*Cp(14));

```

```

%Mask
Tdot15 = (Q_TrussARad_Mask + Q_TrussSun_Mask - QR_Mask_CCD + Q_TrussASun_Mask
+ Q_TrussRad_Mask + Q_Albedo_Mask + Q_IR_Mask - Q_mask + QR_RadSShield_Mask +
QR_ASunSShield_Mask + QR_SunSShield_Mask +
QR_ARadSShield_Mask) / (m(15) * Cp(15));

Tdot =
[Tdot1;Tdot2;Tdot3;Tdot4;Tdot5;Tdot6;Tdot7;Tdot8;Tdot9;Tdot10;Tdot11;Tdot12;T
dot13;Tdot14;Tdot15];

```

```

function [inputs,rexis] = getInputs(rexis)

%-----
inputs(5) = rexis.dv.orex.thermal.decktemperature(1); % Temperature of the
deck [K] Nom = 300
inputs(6) = rexis.dv.environment.thermal.spacetemperature(1); % Temperature
of space [K] Nom = 2.7
%-----
inputs(7) = rexis.dv.radiator.structure.radiatorarea(1); % Area of the
radiator [m^2] Nom = .054
inputs(8) = rexis.dv.mask.structure.maskarea(1); % Area Mask [m^2] Nom =
.027225
inputs(9) = rexis.dv.ccd.structure.ccdarea(1); % Area CCD [m^2] Nom =
0.027225
inputs(10) = rexis.dv.dass.structure.dassarea(1); % Area DASS [m^2] Nom =
0.027225
inputs(11) = rexis.dv.eb.structure.ebarea(1); % Area EB [m^2] Nom = 0.027225
inputs(12) = rexis.dv.sideshield.structure.ssarea(1); % Area Shield [m^2] Nom
= .0379
%-----
inputs(13) = rexis.dv.radiator.thermal.radiatoreps(1); % Emissivity of the
Radiator Nom = .9
inputs(14) = rexis.dv.mask.thermal.maskeps(1); % Emissivity of the Mask Nom =
.05
inputs(15) = rexis.dv.sideshield.thermal.sseps(1); % Emissivity of the Side
Shield Nom = .03
inputs(16) = rexis.dv.eb.thermal.ebeps(1); % Emissivity of the EB Nom = .03
inputs(17) = rexis.dv.dass.thermal.dasseps(1); % Emissivity of the DASS Nom =
.03
inputs(18) = rexis.dv.ccd.thermal.ccdeps(1); % Emissivity of the CCD Nom =
.03
inputs(1) = rexis.dv.orex.thermal.deckeps(1); % Emissivity of deck surface
Nom = 0.05
inputs(2) = rexis.dv.mli.thermal.trusseps(1); % Emissivity of MLI on truss
surface Nom = 0.05
%-----
inputs(19) = rexis.pv.radiator.thermal.rad2deckvf(1); % View Factor from
Radiator to Deck Nom = .10254
inputs(20) = rexis.pv.radiator.thermal.rad2spacevf(1); % View Factor from
Radiator to Space Nom = .89746
inputs(21) = rexis.pv.sideshield.thermal.ss2ccdvf(1); % View Factor from Side
Shield to CCD Nom = .1422
inputs(22) = rexis.pv.eb.thermal.eb2dassvf(1); % View Factor from EB to DASS
Nom = .8511
inputs(23) = rexis.pv.mask.thermal.mask2ccdvf(1); % View Factor from Mask to
CCD Nom = .1016
inputs(24) = rexis.pv.mask.thermal.mask2spacevf(1); % View Factor from Mask
To Space Nom = .8621
inputs(25) = rexis.pv.sideshield.thermal.ss2ossvf(1); % View Factor from Side
Shield to Opposite Side Shield Nom = .2583
inputs(26) = rexis.pv.sideshield.thermal.ss2assvf(1); % View Factor from Side
Shield to Adjacent Side Shield Nom = .2284
inputs(27) = rexis.pv.sideshield.thermal.ss2maskvf(1); % View Factor from
Side Shield to Mask Nom = .1424
inputs(4) = rexis.pv.trussarad.thermal.truss2spacevf(1); % View factor from
truss to space on truss arad face

```

```

inputs(28) = rexis.pv.trussarad.thermal.truss2deckvf(1); % View factor from
truss to deck on truss arad face
inputs(29) = rexis.pv.trussasun.thermal.truss2spacevf(1); % View factor from
truss to space on truss asun face
inputs(30) = rexis.pv.trussasun.thermal.truss2deckvf(1); % View factor from
truss to deck on truss arad face
inputs(31) = rexis.pv.trusssun.thermal.truss2spacevf(1); % View factor from
truss to space on truss sun face
inputs(3) = rexis.pv.trusssun.thermal.truss2deckvf(1); % View factor from
truss to deck on truss arad face
%-----
% Update 'rexis' structure with view factors
rexis.pv.radiator.thermal.rad2deckvf(1) = inputs(19); % View Factor from
Radiator to Deck Nom = .10254
rexis.pv.radiator.thermal.rad2spacevf(1) = inputs(20); % View Factor from
Radiator to Space Nom = .89746
rexis.pv.sideshield.thermal.ss2ccdvf(1) = inputs(21); % View Factor from Side
Shield to CCD Nom = .1422
rexis.pv.eb.thermal.eb2dassvf(1) = inputs(22); % View Factor from EB to DASS
Nom = .8511
rexis.pv.mask.thermal.mask2ccdvf(1) = inputs(23); % View Factor from Mask to
CCD Nom = .1016
rexis.pv.mask.thermal.mask2spacevf(1) = inputs(24); % View Factor from Mask
To Space Nom = .8621
rexis.pv.sideshield.thermal.ss2ossvf(1) = inputs(25); % View Factor from Side
Shield to Opposite Side Shield Nom = .2583
rexis.pv.sideshield.thermal.ss2assvf(1) = inputs(26); % View Factor from Side
Shield to Adjacent Side Shield Nom = .2284
rexis.pv.sideshield.thermal.ss2maskvf(1) = inputs(27); % View Factor from
Side Shield to Mask Nom = .1424
rexis.pv.trussarad.thermal.truss2spacevf = inputs(4); % View factor from
truss to space on truss arad face
rexis.pv.trussarad.thermal.truss2deckvf = inputs(28); % View factor from
truss to deck on truss arad face
rexis.pv.trussasun.thermal.truss2spacevf = inputs(29); % View factor from
truss to space on truss asun face
rexis.pv.trussasun.thermal.truss2deckvf = inputs(30); % View factor from
truss to deck on truss arad face
rexis.pv.trusssun.thermal.truss2spacevf = inputs(31); % View factor from
truss to space on truss sun face
rexis.pv.trusssun.thermal.truss2deckvf = inputs(3); % View factor from truss
to deck on truss arad face

```

```

function [Q_in] = getQin(rexis)

% Define all heat inputs to REXIS
boltz = 5.670373e-8; % Stefan-Boltzman Constant
emCCD = rexis.dv.ccd.thermal.ccdeps(1);
areaCCD = rexis.dv.ccd.structure.ccdarea(1);
emtruss = rexis.dv.truss.thermal.trusseps(1);
areatruss = rexis.dv.truss.structure.trussarea(1);
emmask = rexis.dv.mask.thermal.maskeps(1);
areamask = rexis.dv.mask.structure.maskarea(1);
VFccd = rexis.pv.ccd.thermal.ccd2spacevf(1);
VFtruss = rexis.pv.truss.thermal.truss2deckvf(1);
VFmask = rexis.pv.mask.thermal.mask2spacevf(1);
Tenv = rexis.sv.environment.thermal.envtemp(end);
Tccd = rexis.sv.ccd.thermal.ccdtemp(end);
Ttrussasun = rexis.sv.trussasun.thermal.trussasuntemp(end);
Tdeck = rexis.sv.deck.thermal.decktemp(end);
Tmask = rexis.sv.mask.thermal.masktemp(end);

Q_in(1) = .82; % CCD dissipation, need to discuss with Marcus
Q_in(2) = emCCD*boltz*areaCCD*(1-VFccd)*(Tenv-Tccd); % Asteroid IR to the
CCDs
Q_in(3) = 0.05*(1367/(0.897*149.6*10^9)^2)*0.08*areaCCD; % Asteroid Albedo to
the CCDs
Q_in(4) = emtruss*boltz*areatruss*VFtruss*(Tdeck-Ttrussasun); % Deck IR to
the Anti-Sun Truss
Q_in(5) = (1367/(0.897*149.6*10^9)^2)*0.08*areatruss; % Direct Solar to Sun
Truss
Q_in(6) = emtruss*boltz*areatruss*VFtruss*(Tdeck-Ttrussasun); % Deck IR to
the Sun Truss
Q_in(7) = emtruss*boltz*areatruss*VFtruss*(Tdeck-Ttrussasun); % Deck IR to
the Anti-Sun Truss
Q_in(8) = emmask*boltz*areamask*(1-VFmask)*(Tenv-Tmask); % Asteroid IR to the
Mask
Q_in(9) = 0.05*(1367/(0.897*149.6*10^9)^2)*0.08*areamask; % Asteroid Albedo
to the Mask
Q_in(10) = 15; % Electronics Box dissipation, need to discuss with Marcus

% % Define all heat inputs to REXIS
% Q_in(1) = .82; % CCD dissipation, need to discuss with Marcus
% Q_in(2) = 0; % Asteroid IR to the CCDs
% Q_in(3) = 0; % Asteroid Albedo to the CCDs
% Q_in(4) = .00; % Deck IR to the Anti-Sun Truss
% Q_in(5) = 1.96; % Direct Solar to Sun Truss
% Q_in(6) = .00; % Deck IR to the Sun Truss
% Q_in(7) = .00; % Deck IR to the Anti-Sun Truss
% Q_in(8) = .29; % Asteroid IR to the Mask
% Q_in(9) = 0; % Asteroid Albedo to the Mask
% Q_in(10) = 15; % Electronics Box dissipation, need to discuss with Marcus

```

```

function [Qout] =
getQout (Trad, Teb, Tmask, Reb2deck, TtrussARad, TtrussSun, TtrussASun)

boltz = 5.670373e-8; % Stefan-Boltzmann constant in [W/m^2 K^4]

[inputs, rexis] = getInputs(rexis);

Tdeck = inputs(5); % Temperature of the Deck
Tspace = inputs(6); % Temperature of Space
Arad = inputs(7); % Area of the Radiator
Amask = inputs(8); % Area of the Mask
emrad = inputs(13); % Emissivity of the Radiator
emmask = inputs(14); % Emissivity of the Mask
VFspace = inputs(20); % View Factor from the Radiator to Space
VFdeck = inputs(19); % View Factor from the Radiator to the Deck
VF_Mask_Space = inputs(24); % View Factor from the Mask to Space
emdeck = inputs(1); % Emissivity of deck surface
emtruss = inputs(2); % Emissivity of truss MLI
Atruss = inputs(12); % Projected outer area of truss MLI covering
VF_truss2space_arad = inputs(4); % View factor from truss to space on truss
arad face
VF_truss2deck_arad = inputs(28); % View factor from truss to deck on truss
arad face
VF_truss2space_asun = inputs(29); % View factor from truss to space on truss
asun face
VF_truss2deck_asun = inputs(30); % View factor from truss to deck on truss
arad face
VF_truss2space_sun = inputs(31); % View factor from truss to space on truss
sun face
VF_truss2deck_sun = inputs(3); % View factor from truss to deck on truss arad
face

% Electronics Box to S/C Deck
Qout(1) = (Teb-Tdeck)/Reb2deck; % Watts

% Radiator to S/C and space
Qdeck = boltz*emrad*emdeck*Arad*VFdeck*(Trad^4 - Tdeck^4);
Qspace = boltz*emrad*Arad*VFspace*(Trad^4 - Tspace^4);
Qout(2) = Qdeck + Qspace;

% Mask to Space
Qout(3) = boltz*emmask*Amask*VF_Mask_Space*(Tmask^4 - Tspace^4);

% Truss to Space
Qout(4) = boltz*emtruss*Atruss*VF_truss2space_arad*(TtrussARad^4 - Tspace^4)
- boltz*emtruss*emdeck*Atruss*VF_truss2deck_arad*(TtrussARad^4 - Tdeck^4);
Qout(5) = boltz*emtruss*Atruss*VF_truss2space_sun*(TtrussSun^4 - Tspace^4) -
boltz*emtruss*emdeck*Atruss*VF_truss2deck_sun*(TtrussSun^4 - Tdeck^4);
Qout(6) = boltz*emtruss*Atruss*VF_truss2space_asun*(TtrussASun^4 - Tspace^4)
- boltz*emtruss*emdeck*Atruss*VF_truss2deck_asun*(TtrussASun^4 - Tdeck^4);

```



```

function [R,rexis] = getConductiveResistances(rexis)

% See the nodal map for reference [K/W]

R(1) =
rexis.dv.til.structure.length(1)/(rexis.dv.til.structure.number(1)*rexis.dv.til.thermal.cond(1)*rexis.dv.til.structure.wallthickness(1)*rexis.dv.til.structure.outerradiuscond(1)*2*pi); % TIL: EB to DASS
R(2) = .1; % CCD to CCD Package
R(3) = 3.03; % CCD Package to DASS
R(4) = 0.5; % DASS to Thermal Strap
R(5) = 0.5; % Thermal Strap to Radiator
R(6) = 5; % DASS to Anti Sun Truss
R(7) = 5; % DASS to Radiator Truss
R(8) =
rexis.dv.radstandoffs.structure.length(1)/(rexis.dv.radstandoffs.structure.number(1)*rexis.dv.radstandoffs.thermal.cond(1)*(pi/4)*rexis.dv.radstandoffs.structure.diameter(1)^4); % Radiator Standoffs: Radiator Truss to Radiator
R(9) = .1; % Radiator Truss to Radiator Truss Side Shield
R(10) = 5; % Radiator Truss to Anti Sun Truss
R(11) = 9.09; % Radiator Truss to Mask
R(12) = 5; % Radiator Truss to Sun Truss
R(13) = 5; % DASS to Sun Truss
R(14) = 5; % DASS to Anti Radiator Truss
R(15) = .1; % Anti Sun Truss to Anti Sun Truss Side Shield
R(16) = .1; % Sun Truss to Sun Truss Side Shield
R(17) = 5; % Anti Sun Truss to Anti Radiator Truss
R(18) = 5; % Sun Truss to Anti Radiator Truss
R(19) = 9.09; % Anti Sun Truss to Mask
R(20) = 9.09; % Anti Radiator Truss to Mask
R(21) = 9.09; % Sun Truss to Mask
R(22) = inv(
inv(rexis.dv.ccd.structure.flexprintlength(1)/(rexis.dv.ccd.structure.flexprintnumber(1)*rexis.dv.ccd.thermal.flexprintcond(1)*rexis.dv.ccd.structure.flexprintside(1)^2)) +
inv(rexis.dv.ccd.structure.kaptonlength(1)/(rexis.dv.ccd.structure.kaptonnumber(1)*rexis.dv.ccd.thermal.kaptoncond(1)*rexis.dv.ccd.structure.kaptonarea(1))) ); % Electronics Box to CCD
R(23) = rexis.dv.eb.thermal.eb2deck(1); % Electronics Box to Deck
R(24) = .1; % Anti Radiator Truss to Anti Radiator Truss Side Shield

```

```
function [Mass,rexis] = getMass(rexis)

% Masses in kilograms

Mass(1) = rexis.pv.eb.structure.mass(1); % EB
Mass(2) = rexis.pv.radiator.structure.mass(1); % Radiator
Mass(3) = rexis.pv.dam.structure.mass(1); % DAM
Mass(4) = rexis.pv.dass.structure.mass(1); % DASS
Mass(5) = rexis.pv.thermalstrap.structure.mass(1); % Thermal Strap
Mass(6) = rexis.pv.ccd.structure.mass(1); % CCD
Mass(7) = rexis.pv.trussrad.structure.mass(1); % Truss Radiator
Mass(8) = rexis.pv.sideshield.structure.mass(1); % Truss Rad Shield
Mass(9) = rexis.pv.trussasun.structure.mass(1); % Truss Anti Sun
Mass(10) = rexis.pv.sideshield.structure.mass(1); % Truss ASun Shield
Mass(11) = rexis.pv.trusssun.structure.mass(1); % Truss Sun
Mass(12) = rexis.pv.sideshield.structure.mass(1); % Truss Sun Shield
Mass(13) = rexis.pv.trussarad.structure.mass(1); % Truss Anti-Rad
Mass(14) = rexis.pv.sideshield.structure.mass(1); % Truss ARad Shield
Mass(15) = rexis.pv.mask.structure.mass(1); % Mask
```

```

function [radiativeHeats] = getRadiativeHeats(T1, T4, T6, T8, T10, T12, T14,
T15)

[inputs, rexis] = getInputs(rexis);

%Return heats [W]

boltz = 5.670373e-8; % Stefan-Boltzman Constant

emmask = inputs(14); % Emissivity of the Mask
emshield = inputs(15); % Emissivity of the Side Shield
emCCD = inputs(18); % Emissivity of the CCDs
emEB = inputs(16); % Emissivity of the Electronics Box
emDASS = inputs(17); % Emissivity of the DASS
areaCCD = inputs(9); % Area of the CCDs
areaDASS = inputs(10); % Area of the DASS
areaMask = inputs(8); % Area of the Mask
areaShield = inputs(12); % Area of the Side Shields
areaEB = inputs(11); % Area of the Electronics Box
VFMaskToCCD = inputs(23); % View Factor from the Mask to the CCD
VFShieldToCCD = inputs(21); % View Factor from the Side Shield to the CCD
VFEBToDASS = inputs(22); % View Factor from the Electronics Box to the DASS
VFShieldToOppShield = inputs(25); % View Factor from the Side Shield to the
Opposite Side Shield
VFShieldToAdjShield = inputs(26); % View Factor from the Side Shield to the
Adjacent Side Shield
VFShieldToMask = inputs(27); % View Factor from the Side Shield to the Mask

radiativeHeats(1) = (boltz*(T1^4 - T4^4))/((1-emEB)/(areaEB*emEB) +
1/(areaEB*VFEBToDASS) + (1-emDASS)/(areaDASS*emDASS)); % Electronics Box to
DASS
radiativeHeats(2) = (boltz*(T12^4 - T6^4))/((1-
emshield)/(areaShield*emshield) + 1/(areaShield*VFShieldToCCD) + (1-
emCCD)/(areaCCD*emCCD)); % Sun Truss Shield to CCD
radiativeHeats(3) = (boltz*(T15^4 - T6^4))/((1-emmask)/(areaMask*emmask) +
1/(areaMask*VFMaskToCCD) + (1-emCCD)/(areaCCD*emCCD)); % Heat from the Mask
to the CCD
radiativeHeats(4) = (boltz*(T14^4 - T6^4))/((1-
emshield)/(areaShield*emshield) + 1/(areaShield*VFShieldToCCD) + (1-
emCCD)/(areaCCD*emCCD)); % Anti Radiator Truss To CCD
radiativeHeats(5) = (boltz*(T10^4 - T6^4))/((1-
emshield)/(areaShield*emshield) + 1/(areaShield*VFShieldToCCD) + (1-
emCCD)/(areaCCD*emCCD)); % Anti Sun Truss Shield
radiativeHeats(6) = (boltz*(T8^4 - T6^4))/((1-emshield)/(areaShield*emshield)
+ 1/(areaShield*VFShieldToCCD) + (1-emCCD)/(areaCCD*emCCD)); % Radiator Truss
Shield to CCD
radiativeHeats(7) = (boltz*(T8^4 - T10^4))/((1-
emshield)/(areaShield*emshield) + 1/(areaShield*VFShieldToAdjShield) + (1-
emshield)/(areaShield*emshield)); % Radiator Side Shield to Anti Sun Side
Shield
radiativeHeats(8) = (boltz*(T8^4 - T14^4))/((1-
emshield)/(areaShield*emshield) + 1/(areaShield*VFShieldToOppShield) + (1-
emshield)/(areaShield*emshield)); % Radiator Side Shield to Anti Rad Side
Shield

```

```

radiativeHeats(9) = (boltz*(T8^4 - T12^4))/((1-
emshield)/(areaShield*emshield) + 1/(areaShield*VFShieldToAdjShield) + (1-
emshield)/(areaShield*emshield)); % Radiator Side Shield to Sun Side Shield
radiativeHeats(10) = (boltz*(T8^4 - T15^4))/((1-
emshield)/(areaShield*emshield) + 1/(areaShield*VFShieldToMask) + (1-
emmask)/(areaMask*emmask)); % Radiator Side Shield to Mask
radiativeHeats(11) = (boltz*(T10^4 - T15^4))/((1-
emshield)/(areaShield*emshield) + 1/(areaShield*VFShieldToMask) + (1-
emmask)/(areaMask*emmask)); % Anti Sun Side Shield to Mask
radiativeHeats(12) = (boltz*(T10^4 - T14^4))/((1-
emshield)/(areaShield*emshield) + 1/(areaShield*VFShieldToAdjShield) + (1-
emshield)/(areaShield*emshield)); % Anti Sun Side Shield to Anti Rad Side
Shield
radiativeHeats(13) = (boltz*(T10^4 - T12^4))/((1-
emshield)/(areaShield*emshield) + 1/(areaShield*VFShieldToOppShield) + (1-
emshield)/(areaShield*emshield)); % Anti Sun Side Shield to Sun Side Shield
radiativeHeats(14) = (boltz*(T12^4 - T14^4))/((1-
emshield)/(areaShield*emshield) + 1/(areaShield*VFShieldToAdjShield) + (1-
emshield)/(areaShield*emshield)); % Sun Side Shield to Anti Rad Side Shield
radiativeHeats(15) = (boltz*(T12^4 - T15^4))/((1-
emshield)/(areaShield*emshield) + 1/(areaShield*VFShieldToMask) + (1-
emmask)/(areaMask*emmask)); % Sun Side Shield to Mask
radiativeHeats(16) = (boltz*(T14^4 - T15^4))/((1-
emshield)/(areaShield*emshield) + 1/(areaShield*VFShieldToMask) + (1-
emmask)/(areaMask*emmask)); % Anti Rad Side Shield to Mask

%-----
% 1- EB to DASS
% 2- Sun Side Shield to the CDD
% 3- Mask to CCD
% 4- Anti Rad Side Shield to CCD
% 5- Anti Sun Side Shield to CCD
% 6- Rad Side Shield to CCD
% 7- Rad Side Shield to Anti Sun Side Shield
% 8- Rad Side Shield to Anti Rad Side Shield
% 9- Rad Side Shield to Sun Side Shield
% 10- Rad Side Shield to Mask
% 11- Anti Sun Side Shield to Mask
% 12- Anti Sun Side Shield to Anti Rad Side Shield
% 13- Anti Sun Side Shield to Sun Side Shield
% 14- Sun Side Shield to Anti Rad Side Shield
% 15- Sun Side Shield to Mask
% 16- Anti Rad Side Shield to Mask
%-----

```

```

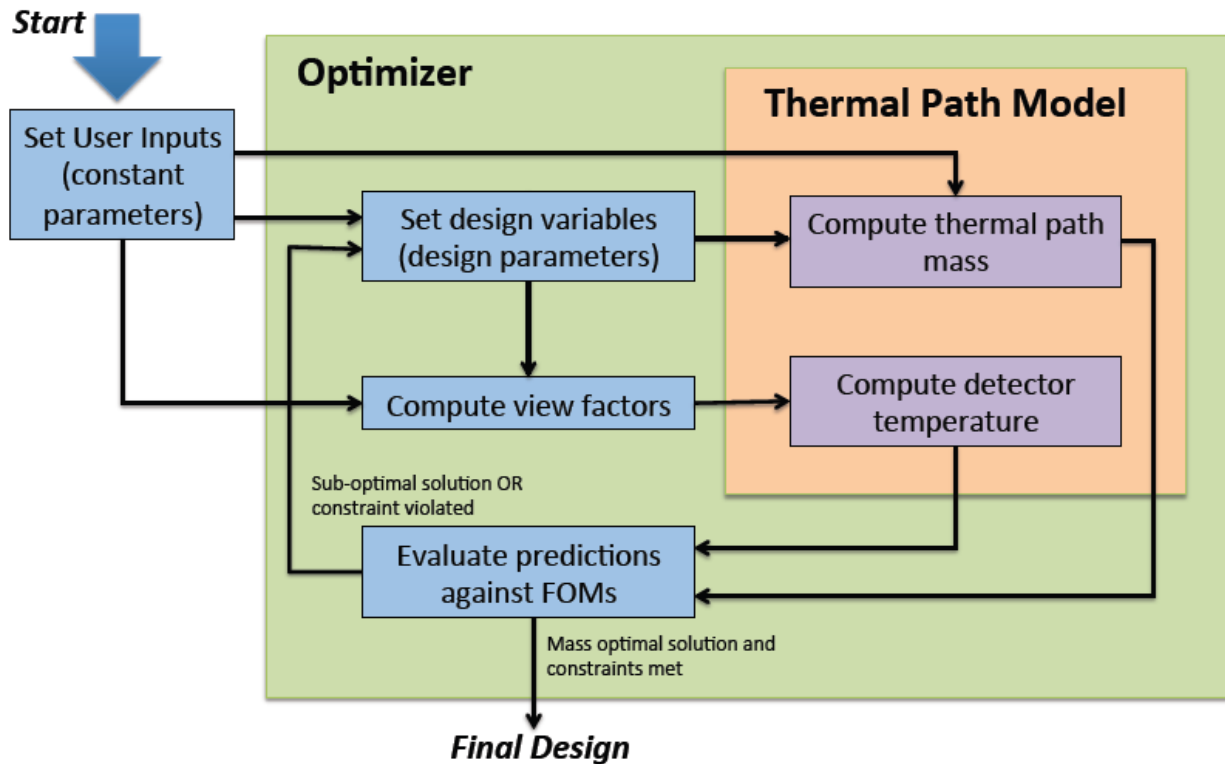
function [Cp,rexis] = getSpecificHeats(rexis)

% Specific Heat Capacities [J/kg-K]

Cp(1) = rexis.dv.eb.thermal.specheat(1); % EB Nom = 961
Cp(2) = rexis.dv.radiator.thermal.specheat(1); % Radiator Nom = 961
Cp(3) = rexis.dv.dam.thermal.specheat(1); % DAM Nom = 961
Cp(4) = rexis.dv.dass.thermal.specheat(1); % DASS Nom = 961
Cp(5) = rexis.dv.thermalstrap.thermal.specheat(1); % Thermal Strap Nom = 961
Cp(6) = rexis.dv.ccd.thermal.specheat(1); % CCD Nom = 1882.8
Cp(7) = rexis.dv.trussrad.thermal.specheat(1); % Truss Radiator Nom = 961
Cp(8) = rexis.dv.sideshield.thermal.specheat(1); % Truss Rad Shield Nom = 144
Cp(9) = rexis.dv.trussasun.thermal.specheat(1); % Truss Anti Sun Nom = 961
Cp(10) = rexis.dv.sideshield.thermal.specheat(1); % Truss ASun Shield Nom =
144
Cp(11) = rexis.dv.trusssun.thermal.specheat(1); % Truss Sun Nom = 961
Cp(12) = rexis.dv.sideshield.thermal.specheat(1); % Truss Sun Shield Nom =
144
Cp(13) = rexis.dv.trussarad.thermal.specheat(1); % Truss Anti-Rad Nom = 961
Cp(14) = rexis.dv.sideshield.thermal.specheat(1); % Truss ARad Shield Nom =
144
Cp(15) = rexis.dv.mask.thermal.specheat(1); % Mask Nom = 129

```

Appendix C: Thermal Strap and Radiator Nonlinear Model Code



Thermal Strap and Radiator Thermal Path Code Structure

Functions

optimizeRad.m ~ optimizer

getinputs.m ~ input file with design variables and parameters

funRad.m ~ compute mass of thermal strap and radiator assembly

radSolver.m ~ call radiator model and thermal strap/view factor locations

radPerfModel.m ~ radiator thermal model; non-linear

getParVals.m ~ store view factor and thermal strap mount locations

processResults.m ~ perform mass sensitivity analysis

Table of Constant Parameters for Design Optimization of Thermal Strap and Radiator Thermal Path

Parameter	Symbol in code	Value	Units
Emissivity of radiator	eps	0.9	--
Conductivity of radiator	k	167	W/m-K
Total heat load	Qi	2	W
Thermal strap end fitting size in x-direction	dxlugsize	2	cm
Thermal strap end fitting size in y-direction	dylugsize	1	cm
Discretization size	pixres	1	cm
Radiator density	densRad	2.7	g/cm ³
Conductivity of thermal strap	kTS	400	W/m-K
Mass of one end fitting of thermal strap	masslug	15	g
Density of thermal strap	densTS	8.94	g/cm ³
Nominal thermal strap length	nominalTSlength	5	cm
Height of DASS above instrument deck	DASSheight	10	cm
DASS centerline in radiator design envelope	DASScenterline	10	cm

```

function [x,fval,exitflag,output,lambda,grad] = optimizeRad

format long g
format compact
global VFfull eps k Qi Q_TS dxlugsize dylugsize pixres densRad densTS
masslugs nominalTSlength DASSheight DASScenterline mdesign kTS

% Retrieve non-parametric inputs
[VFfull] = sampleVF;
[eps,k,Qi,Q_TS,dxlugsize,dylugsize,pixres,densRad,densTS,masslugs,nominalTSleng
ngth,DASSheight,DASScenterline,mdesign,kTS] = getinputs();

% Define initial design variables
w = .10;% Width of radiator in 'm'
h = .20;% Height of radiator in 'm'
t = .001;% Thickness of radiator in 'm'
xTS = .10;% X-coord of bottom-left corner of thermal strap lug in envelope
space in 'm'
yTS = .15;% Y-coord of bottom-left corner of thermal strap lug in envelope
space in 'm'
ATS = .1;% Cross-sectional area of thermal strap in 'cm^2'
hradmin = .05;% Min height of radiator above deck in 'm'
x0 = [w h t xTS yTS ATS hradmin]';

% Define upper/lower bounds on design variables
wmin = .01;
wmax = .20;
hmin = .01;
hmax = .40;
tmin = .0001;
tmax = .01;
xTSmin = 0.03;
xTSmax = 0.10;
yTSmin = 0.10;
yTSmax = 0.30;
ATSmin = 0.00785;% Area corresponds to 1mm diameter strap in 'cm^2'
ATSmax = 3.1415926;% Area corresponds to 2cm diamter strap in 'cm^2'
hradminmin = 0.01;
hradminmax = 0.20;

% Define lb and ub
lb = [wmin hmin tmin xTSmin yTSmin ATSmin hradminmin]';
ub = [wmax hmax tmax xTSmax yTSmax ATSmax hradminmax]';

% Complete filler matrices
Aeq = [];
beq = [];
A = [-.3 0 0 -1 0 0 0; ...
     -.3 0 0 1 0 0 0; ...
     0 0 0 0 -1 0 1; ...
     0 -1 0 0 1 0 -1; ...
     0 1 0 0 0 0 1];
b = [-DASScenterline*1e-2; ...
     DASScenterline*1e-2; ...
     0; ...
     0; ...

```



```
0.39];

% Call optimizer
tic;
xstep = [0.005 0.005 0.00005 0.005 0.005 0.003 .005]';
options = optimset('AlwaysHonorConstraints','bounds','Algorithm','active-
set','FinDiffRelStep',xstep,'TolX',1e-5,'TolFun',1e-3,'MaxFunEvals',10000);
[x,fval,exitflag,output,lambda,grad] =
fmincon(@funRad,x0,A,b,Aeq,beq,lb,ub,@RadSolver,options);
toc;
```

```

function
[eps,k,Qi,Q_TS,dxlugsize,dylugsize,pixres,densRad,densTS,massslugs,nominalTSlength,DASSheight,DASScenterline,mdesign,kTS] = getinputs()

format long g
format compact

%-----
% Define non-parametric input variables
% Radiator
eps = 0.9;% Emissivity of radiator coating in phase 5B (M.Choi Recommendation)
k = 167;% Conductivity of core radiator in 'W/m/K' (6061-T6 Aluminum)
Qi = 2;% Total input heat in 'W' (Calculated input heat with margin)
dxlugsize = 2;% TS lug size in x-direction in 'cm' (3 cm)
dylugsize = 1;% TS lug size in y-direction in 'cm' (1 cm)
pixres = .01;% Spatial distance between the center of each pixel in 'm' (1 cm, dont' change!)
densRad = 2.7;% Density of core radiator material in 'g/cm^3' (6061-T6 Aluminum)
mdesign = 400;% Design threshold mass of radiator and thermal strap in 'g'
% Thermal Strap
%R_TS = 2.0;% Absolute thermal resistance of thermal strap in 'W/m/k' (Guess)
kTS = 400;% Conductivity of thermal strap in 'W/m-K' (Cu)
masslug = 15;% Mass of one lug of thermal strap in 'g' (Guess)
densTS = 8.940;% Density of thermal strap material in 'g/cm^3' (Pure Cu)
nominalTSlength = 5;% Length of nominal thermal strap in 'cm' (Guess)
DASSheight = 10;% Y-coord of top surface of DASS at centerline edge in envelope space in 'cm' (Guess)
DASScenterline = 10;% X-coord of DASS centerline in envelope space in 'cm' (Guess)
%TScrossarea = .75^2;% Cross-sectional area of thermal straps in 'cm^2' (Guess)

% Determine values of interest
Q_TS = Qi/(dxlugsize*dylugsize);% Height flow to radiator through thermal strap to each pixel in 'W'
massslugs = 2*masslug;% Total mass of lugs in 'g'
%-----

```

```

function [massRadTS] = funRad(x)

format long g
format compact
global densRad densTS masslugs nominalTSlength DASSheight DASScenterline

% Unpack design variables into 'cm'
wRad = roundn(x(1),-2)*100;
hRad = roundn(x(2),-2)*100;
tRad = x(3)*100;
xTS = roundn(x(4),-2)*100;
yTS = roundn(x(5),-2)*100;
ATS = roundn(x(6),-4);

% Determine mass of radiator
massRad = densRad*wRad*hRad*tRad;

% Determine mass of thermal strap
radTSlength = sqrt( (xTS-DASScenterline)^2 + (yTS-DASSheight)^2 );% Length of
thermal strap running up radiator to mounting position in 'cm'
TSlength = nominalTSlength + radTSlength;% Total length of thermal strap in
'cm'
volumeTS = TSlength*ATS;% Volume of thermal strap in 'cm^3'
massTS = masslugs + densTS*volumeTS;

% Determine total mass of both thermal strap and radiator in 'g'
massRadTS = massTS + massRad;

%{
% Output in c and ceq format
c = massRadTS - mdesign;
ceq = [];
%}

```

```

function [c,ce] = RadSolver(x)

format long g
format compact
global Qi iTS jTS VF tRad DASSheight DASScenterline kTS nominalTSlength

% Get variables associated with parametric variables
[VF,iTS,jTS] = getParVals(x);
tRad = x(3);
xTS = roundn(x(4),-2)*100;
yTS = roundn(x(5),-2)*100;
ATS = roundn(x(6),-4)/1000;

imax = max(VF(:,1));
jmax = max(VF(:,2));
Trad0 = 273*ones(imax,jmax);
options=optimset('TolX',1e-4,'TolFun',1e-4);
[Trad,Func] = fsolve(@RadPerfModel,Trad0,options);

Trad_max = max(max(Trad));% Max radiator temperature

radTSlength = sqrt( (xTS-DASScenterline)^2 + (yTS-DASSheight)^2 );% Length of
thermal strap running up radiator to mounting position in 'cm'
TSlength = nominalTSlength + radTSlength;% Total length of thermal strap in
'cm'
R_TS = (TSlength/100)/(kTS*ATS);
TDASS = Qi*R_TS + Trad_max;% Determine temperature of DASS

c = TDASS - 213.15;
ce = [];

%figure;hold on;imagesc((Trad'-273.15));xlabel('Width [cm]');ylabel('Height
[cm]');title('Radiator Temperature Distribution [Celsius]');colorbar;axis([1
imax 1 jmax]);hold off;
end

```

```

function [Func] = RadPerfModel(Trad)

format long g
format compact
global VF eps k Q_TS pixres tRad iTS jTS

%-----%
% Define input parameters
sig = 5.670373e-8;
% Extract parameters
imax = max(VF(:,1));
jmax = max(VF(:,2));
Ai = pixres^2;
Lpix = sqrt(Ai);
Rcond = Lpix/(Lpix*tRad*k);
radCons = sig*eps*Ai;
% Initialize values
Func = [];
count = 1;
iTS = round(iTS);
jTS = round(jTS);
%-----%

%-----%
% Construct radiator equations
for i = 1:imax;
    for j = 1:jmax;

        % Find current pixel line in VF (gives temperature/FOV info)
        currVFrads = VF(count,3:end);
        count = count + 1;

        % Radiator pixel input: thermal strap
        if any(iTS == i) && any(jTS == j)
            Qin_TS = Q_TS;
        else
            Qin_TS = 0;
        end

        % Radiator pixel output: radiation out
        Qout_rad = 0;
        for p = 1:2:length(currVFrads);
            Qout_rad = Qout_rad + radCons*(Trad(i,j)^4-
currVFrads(p)^4)*currVFrads(p+1);
        end

        % Radiator pixel input: conduction between pixels
        if i == 1
            Qleft = 0;
        else
            Qleft = (Trad(i-1,j)-Trad(i,j))/Rcond;
        end
        if i == imax
            Qright = 0;
        else

```

```

        Qright = (Trad(i+1,j)-Trad(i,j))/Rcond;
    end
    if j == jmax
        Qup = 0;
    else
        Qup = (Trad(i,j+1)-Trad(i,j))/Rcond;
    end
    if j == 1
        Qdown = 0;
    else
        Qdown = (Trad(i,j-1)-Trad(i,j))/Rcond;
    end
    Qin_cond = Qleft + Qright + Qup + Qdown;

    % Store equation as function to be handled
    Func(i,j) = Qin_TS - Qout_rad + Qin_cond;

end
end
Func = reshape(Func,imax*jmax,1);

```

```

function [VF,iTS,jTS] = getParVals(x)

global VFfull dxlugsizedylugsizedASScenterline

% Unpack design variables into 'cm'
wRad = roundn(x(1),-2)*100;
hRad = roundn(x(2),-2)*100;
xTS = roundn(x(4),-2)*100;
yTS = roundn(x(5),-2)*100;
hradmin = roundn(x(7),-2)*100;

% Determine thermal strap plug-in location on radiator in radiator frame
iTSp = xTS - round( ASScenterline-wRad/2 );
jTSp = yTS - hradmin;
iTS = iTSp:1:(iTSp+dxlugsized-1);% Width-wise pixel value for thermal strap
insertion
jTS = jTSp:1:(jTSp+dylugsized-1);% Height-wise pixel value for thermal strap
insertion

% Determine relevant VF
xmin = round( ASScenterline-wRad/2 ) + 1;
xmax = round( ASScenterline+wRad/2 );
ymin = hradmin + 1;
ymax = hradmin+hRad;
idx = find( VFfull(:,1)<=xmax & VFfull(:,1)>=xmin & VFfull(:,2)<=ymax &
VFfull(:,2)>=ymin );
VF = VFfull(idx,:);
minw = min(VF(:,1))-1;
minh = min(VF(:,2))-1;
VF(:,1) = VF(:,1) - minw;
VF(:,2) = VF(:,2) - minh;

```

```

function processResults(x,Jx,gradJx)

format long g
format compact
numvar = length(x);

%-----
% Sensitivity Analysis

% Determine normalized gradients
normgradJx = [];
for i = 1:numvar
    normgradJx = [normgradJx; (x(i)/Jx)*gradJx(i)];
end

% Plot sensitivities (norm gradients)
figure;
hold on;
bar(normgradJx)

title('Normalized Sensitivities')
xlabel('Parametric Design Variables')
ylabel('(x_i / J_x) (DJ_x)')

% Plot performance vs. design variable perturbations
figure;
hold on;
disturb = .01:.02:.15;
perfpurd = [];
for i = 1:numvarset(gca,'XTickLabel',{'Width','Height','Thickness','TS X-
coord','TS Y-coord','Radiator Height'})
    set(gca,'XTick',1:numvar)
    perfpurd = [perfpurd;disturb.*normgradJx(i)];
end
plot(100*disturb,100*perfpurd(1,:), 'r', 'LineWidth',2.5)
plot(100*disturb,100*perfpurd(2,:), 'b', 'LineWidth',2.5)
plot(100*disturb,100*perfpurd(3,:), 'g', 'LineWidth',2.5)
plot(100*disturb,100*perfpurd(4,:), 'k', 'LineWidth',2.5)
plot(100*disturb,100*perfpurd(5,:), 'm', 'LineWidth',2.5)
plot(100*disturb,100*perfpurd(6,:), 'c', 'LineWidth',2.5)
xlabel('Parametric Variable Disturbance [%]')
ylabel('Change in Performance Function [%]')
legend('Width','Height','Thickness','xTS','yTS','Radiator Height')
hold off

%-----

```


Appendix D: Linearized Resistor Network 3-D Radiator Thermal Model

```
function [G,b,radmap] = solveRad(x0,pf)

%-----
% Unpack user radiator input parameters
sb = x0(1); % SB constant
em = x0(2); % Emissivity of radiating surface
w = x0(3); % Width of radiator in 'm'
h = x0(4); % Height of radiator in 'm'
t = x0(5); % Thickness of radiator in 'm'
Qin = x0(6); % Heat load in 'W'
dx = x0(7); % Radiator pixel size in all three directions
k = x0(8); % Conductivity of radiator in 'W/m-K'
TSfootprintX = x0(9); % Footprint of thermal strap lug in x- direction in 'm'
TSfootprintY = x0(10); % Footprint of thermal strap lug in y- direction in
'm'
TSlocationX = x0(11); % X- location of thermal strap plug-in in 'm'
TSlocationY = x0(12); % Y- location of thermal strap plug-in in 'm'

%-----

% Solve for isothermal equilibrium parameters
Ao = w*h; % Frontal surface area of radiator
Ai = dx^2; % Pixel area
To = (Qin/(em*sb*Ao))^(1/4); % Isothermal SS radiator temperature
QTSpix = (TSfootprintX*TSfootprintY)/(dx^2); % Number of pixels thermal strap
lug covers
QTSi = Qin/QTSpix; % Heat load on each pixel due to thermal strap

% Solve for system resistances
Rcond = (k*dx)^(-1);
Rrad = (4*sb*em*Ai*To^3)^(-1);
Israd = 3*sb*em*Ai*To^4;

% Generate nodal matrix, G and current source matrix, b
numnodes = (w/dx)*(h/dx)*(t/dx);
numwnodes = w/dx;
numhnodes = h/dx;
numtnodes = t/dx;
numAnodes = numwnodes*numhnodes;

% Find the node numbers that correspond to where the thermal strap plugs in
firstBSnode = (numtnodes-1)*numAnodes+1;
yoffset = (TSlocationY/dx)*numwnodes;
xoffset = TSlocationX/dx;
totaloffset = yoffset+xoffset;
firstTSnode = firstBSnode+totaloffset;
TSxwidth = TSfootprintX/dx;
TSywidth = TSfootprintY/dx;
TSnodes = [];
```

```

for i = 1:TSywidth
    TSnodes = [TSnodes firstTSnode+numwnodes*(i-
1)+1:firstTSnode+numwnodes*(i-1)+TSxwidth];
end

% This part generates variables that flag the node numbers that are on the
% sides of the 3D resistor network
xn_sides = 1:numwnodes:numnodes;
xp_sides = numwnodes:numwnodes:numnodes;
zp_sides = 1:numAnodes;
zn_sides = (numtnodes-1)*numAnodes+1:numnodes;
yp_sides = [];
yn_sides = [];
for i = 1:numtnodes
    yp_sides = [yp_sides numAnodes*(i-1)+1:numwnodes+numAnodes*(i-1)];
    yn_sides = [yn_sides numAnodes*i-numwnodes+1:numAnodes*i];
end

G = spalloc(numnodes,numnodes,7*numnodes);
b = zeros(numnodes,1);
for i = 1:numnodes
    % Store entries for current source matrix
    if ismember(i,zp_sides) == 1
        b(i) = b(i) - Israd;
    end
    if ismember(i,TSnodes) == 1
        b(i) = b(i) - QTSi;
    end

    % Store entries for nodal matrix

    % Radiation
    if i < (numAnodes) % if on outer surface
        G(i,i) = G(i,i) - (1/Rrad); % add radiation out term
    end

    % Conduction
    flags = [ismember(i,xp_sides) ismember(i,xn_sides) ismember(i,yp_sides)
ismember(i,yn_sides) ismember(i,zp_sides) ismember(i,zn_sides)];
    Gnum = -length(find(flags==0));
    G(i,i) = G(i,i) + Gnum/Rcond;

    if flags(1) == 0
        G(i,i+1) = 1/Rcond;
    end
    if flags(2) == 0
        G(i,i-1) = 1/Rcond;
    end
    if flags(3) == 0
        G(i,i-numwnodes) = 1/Rcond;
    end
    if flags(4) == 0
        G(i,i+numwnodes) = 1/Rcond;
    end
end

```

```

    if flags(5) == 0
        G(i,i-numAnodes) = 1/Rcond;
    end
    if flags(6) == 0
        G(i,i+numAnodes) = 1/Rcond;
    end

    disp([num2str(i), ' of ', num2str(numnodes)])

end

if pf == 1
    figure;
    hold on;
    spy(G);
    title('Sparsity Plot for Nodal Matrix')
    hold off
end

%-----
% Solve the system

[L,U] = lu(G);
y = L\b;
x = U\y;

Trad = x;
radmap = Trad;
if pf == 1
    radmap = [];
    % Build 3D array of temperatures for plotting
    count = 1;
    for i = 1:numtnodes
        for j = 1:numhnodes
            for k = 1:numwnodes
                radmap(k,j,i) = Trad(count);
                count = count + 1;
            end
        end
    end
end

% Plot radiator temperature distribution
figure;
hold on;
imagesc(radmap(:,:,1))
colorbar
hold off;
end

```

Appendix E: REXIS Preliminary Design Review Thermal Model

This appendix documents the thermal model used for the REXIS Preliminary Design Review (PDR). The REXIS thermal model was created in Thermal Desktop, an industry standard modeling tool for spacecraft thermal modeling. Aspects of the model include the geometry model, materials definition, connection of the components within the model, and heat loading.

Model Assumptions

Each thermally significant component was represented in the REXIS PDR thermal model. In general, a component is thermally significant when it:

- Lies in the thermal path of a critical REXIS component (e.g., CCDs)
- Facilitates significant heat transfer (e.g., radiator)
- Contains a sufficiently large temperature gradient across its surface or through its volume (e.g., TIL)
- Has significant thermal inertia (a function of mass and specific heat) to drive the time constants of the REXIS TCS (e.g., DAM)

However, each component cannot be modeled exactly in Thermal Desktop because it is time consuming for the user to define the geometry of a component and its connections to other components in the system. For example, it is cumbersome and requires many nodes to model a fillet on the corner of a box. Many of these details are burdensome to represent in Thermal Desktop and are thermally insignificant. Table 1 contains a list of model assumptions for the REXIS PDR thermal model. The assumptions state which components are included in the thermal model and the simplification made to represent the component in the model.

Table 1: Component assumptions for REXIS PDR thermal model

REXIS Component	Quantity	Material	Captured in thermal model?	Assumptions
Electronics box walls	6	Aluminum	Yes	All grooves, screw holes, and contact between walls are thermally insignificant. Modeled as six-sided box with edge-nodes that are welded together.
Printed circuit boards	3	FR4/G10	Yes	Very conservatively modeled as 2mm thick sheets of FR4 – the heat must travel through the FR4 to the edges of the board into the electronics box walls.
Electronic components	Many	--	Yes	Represent components as point heat loads with magnitudes equivalent to the component power draws. Current best estimates values are used for cold cases, and maximum expected values are used for hot cases.
CCDs	4	Silicon	Yes	Modeled as a single piece of silicon because the CCDs are so thin that there will not be a significant temperature gradient from its top to bottom surfaces.
TIL standoffs	5	Torlon 5030	Yes	Mechanical design is unknown at this point. The effective TIL geometry that must be included in the standoff is a 1.0 cm diameter standoff that is 1.25 cm long.
DASS	1	Aluminum	Yes	Heat transfer from the top to bottom surface is negligible so it can be modeled as a 2-D plane.
Truss panels	4	Aluminum	Yes	Modeled as a flat plate of thickness equivalent to the side shields – the X-webbing and thicker edges in the mechanical design were assumed thermally insignificant.
Side Shields	4	Aluminum	Yes	Integrated as part of the flat plate truss panel – in field of view of detector.
Radiator	1	Aluminum	Yes	Modeled as 2-D plane because it is assumed that the temperature differential from its outer to inner surface is negligible.
Thermal Strap	1	--	No	Captured as a conductor in the model – not physically represented. This is a custom piece and its absolute conductance is guaranteed by the vendor. Set baseline conductance to 0.25 W/K.
DAM	1	Aluminum	Yes	Captured as a solid piece of aluminum of equivalent mass to the actual DAM so that the thermal inertias are identical.

Radiator Cover	1	Aluminum	No	As a passive piece that is deployed during operation and only serves to protect the CCDs from radiation during Cruise Phase, this component was deemed thermally insignificant.
Frangibolt	1	Aluminum	Yes	Though the Frangibolt is a component made of many materials, some proprietary – it is captured in the model as a 3-D brick of aluminum of equivalent thermal inertia to the Frangibolt and its housing.
Spring hinge	1	--	No	This piece does not facilitate significant heat transfer in the REXIS design because it is not in the thermal path of any critical components.
Coded aperture mask	1	Stainless Steel	Yes	The coded aperture area is replaced with a solid hole of equivalent area to the total throughput of the mask.
Wiring	N/A	Copper	Yes	Only wiring that extends from the electronics box to the telescope truss structure is captured in the model through conductors that use the equivalent lengths and areas of the copper wires.
MLI	11	--	Yes	Numerically represented in Thermal Desktop with the 'Insulation' feature on a components 'edit' menu. MLI is placed on the outer surface of each truss panel, the outer surface of each electronics box side wall, the top surface of the electronics box, the bottom surface of the DASS, and the back surface of the radiator.

Geometry Model

The geometry model of REXIS is the physical construction of the components in the computer-aided design space of Thermal Desktop. The geometry model includes the discretizations of the components and their material properties. Figure 1 shows a three-sided view of the REXIS PDR thermal model in Thermal Desktop. This model contains 113 nodes (including insulation nodes for MLI) and was used to generate results for PDR.

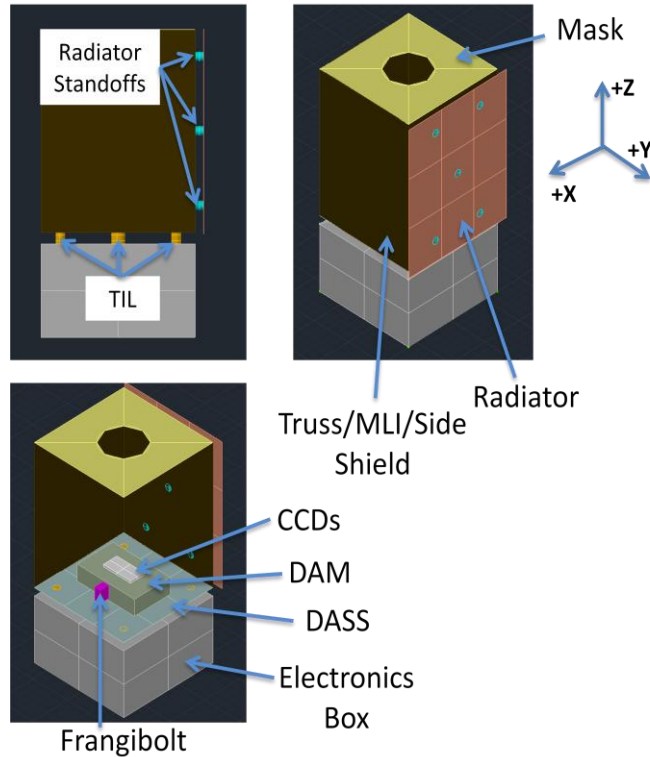


Figure 1: Geometrical thermal model of REXIS

Although the PDR thermal model is a reduced-order thermal model of REXIS, the component representation is very similar to the mechanical REXIS design. The electronics box is represented as a six-sided box of 2-D planes connected at the corners. The electronics boards are modeled conservatively as solid sheets of FR4 (glass-reinforced epoxy laminate sheets). The TIL standoffs rest on the upper surface of the electronics box and connect the telescope truss structure to the electronics box. Each truss panel, side shield, and MLI piece is represented by a single 2-D plane of thickness equivalent to the side shields. Assuming the very small side shield thickness is conservative for this model because heat flows in the $-z$ -direction to the thermal strap and radiator assembly – reducing the cross-sectional area reduces the efficiency of the heat transfer. The DASS is also represented by a 2-D plane, and the DAM is a brick of aluminum of equivalent size to match the thermal inertia of the actual mechanical DAM design. The CCDs are modeled as a brick physically connected to the top surface of the DAM, exposed to the asteroid through the hole in the coded aperture mask. The Frangibolt actuator is also attached to the DAM and physically represented in Figure 1 with 3-D blocks of aluminum. These blocks of aluminum

are meant to have equivalent thermal inertia to the true components, as described in Table 1. Finally, the radiator, represented as a 2-D plane, is mounted to the +y truss panel via five radiator standoffs. All components in the PDR thermal model are represented as 2-D planes except for the TIL, radiator standoffs, DAM, CCDs, and Frangibolt. Table 2 summarizes the discretizations and material properties of each component in the model. The corresponding thermo-physical and optical properties of each material can be found in spacecraft thermal lookup tables [18] and are shown below in Tables 5 and 6. Note: the number of nodes allocated in Table 2 does not include insulation nodes because MLI is represented mathematically on the outside of each surface that is covered with MLI.

Table 2: Summary of geometrical thermal model discretizations and material properties

Component	Discretization (# of nodes each)	MLI? (which surface)	Thermophysical	Optical
Electronics box walls	4	Outer	Aluminum	Annodized aluminum
Electronics boards	9	--	FR4	FR4
TIL	1	--	Torlon 5030	Torlon 5030
DASS	9	Outer	Aluminum	Annodized aluminum
DAM	1	--	Aluminum	Annodized aluminum
Frangibolt	1	--	Aluminum	Annodized aluminum
CCDs	4	--	Silicon	Vapor deposited graphite on aluminum
Truss/Side shields	1	Outer	Aluminum	Gold electroplate
Mask	4	--	Stainless steel	Gold electroplate
Radiator	9	Inner	Aluminum	AZ-2000-IECW White paint
Radiator standoffs	1	--	Stainless steel	Stainless steel

The conservative model of the DEs and MEB PCBs was a 2mm thick sheet of FR4 with no copper layers – this requires that all heat flow through the FR4 to the edge of the boards. At

the time of the REXIS PDR, the component layout of the DEs was largely unknown. Because the individual component power draws for both DE boards are relatively small, the heat load is modeled as distributed uniformly over each board. The left-hand side of Figure 2 shows the DE boards in the PDR thermal model. For the MEB, a functional component layout was used to spatially place the heat loads on the board where the component is located. The heat loads are equivalent to the component power draws. It was found that heat sinking the +3.3 VDC voltage converter, the +5 VDC voltage converter, and the FPGA directly to the spacecraft base plate was necessary to maintain satisfactory MEB component temperatures. Figure 2 shows the DEs and MEB Thermal Desktop representations in the PDR thermal model.

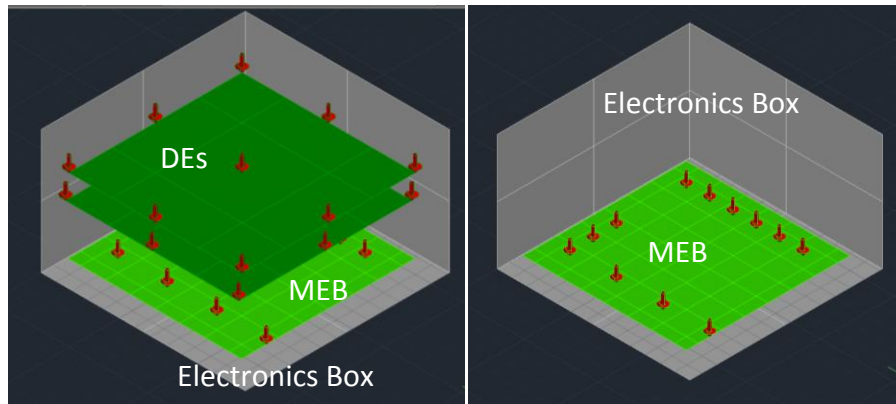


Figure 2: DE boards and uniformly distributed heat loads (left); MEB model and point heat loads corresponding to component power draws (right)

Model Connectivity

Components within the model are thermally connected with conductors and contactors that allow the user to specify the heat transfer relationship between components. In some cases, the absolute conductance between components is known. In other cases, simulation of a material between components, e.g., gap filler, is used. Thermal Desktop allows the user to specify the type of conductor/contactor depending on which is more physically relevant for a given connection. Table 3 documents the conductors and contactors used in the PDR thermal model. One exception to the conductors and contactors is the connectivity between the electronics box

wall sides – these are merged nodes to simulate a negligible contact resistance between any two sides of the box, as indicated in Table 3.

In Table 3, the units are dependent on the modeling scheme for the connection. For example, absolute conductance for the thermal strap is modeled in W/K, whereas the truss panels to DASS interface is filled with Indium foil, a gap filler, resulting in units of inches (an area to length calculation). All length units are in inches because the thermal model is transcribed from the mechanical design. Conductors are used to heat sink the +3.3 and +5.0 VDC voltage converters, and the Virtex-5 FPGA. During trial runs, it was determined that these components would exceed their maximum operating temperatures if not thermally grounded to a sink. In this case, it is assumed that Indium foil is used to connect the components to the base plate of the electronics box.

Table 3: Conductors and contactors for PDR thermal model

Conductors				
Name	Value	Units	Material	Notes
<i>Voltage Converter: +3.3 VDC Heat Sink</i>	10.3	in	Indium Foil	Area/length
<i>Voltage Converter: +5.0 VDC Heat Sink</i>	62	in	Indium Foil	Area/length
<i>FPGA Heat Sink</i>	165.4	in	Indium Foil	Area/length
<i>Thermal Strap</i>	0.25	W/K	--	Absolute
<i>Wiring Parasitic (each)</i>	0.008	W/K	--	Quantity: 4, absolute
Contactors				
Name	Value	Units	Material	Notes
<i>Electronics boards to electronics box walls</i>	0.25	Unitless	Aluminum	Thickness of contact area / length through material, edge contactor
<i>Truss panels to DASS</i>	198.9	in	Indium Foil	Area/thickness, edge contactor
<i>Truss panel to Mask (each)</i>	49.2	in	Indium Foil	Area/thickness, edge contactor, Quantity: 4
<i>Truss panel to truss panel (each)</i>	7.9	in	Indium Foil	Area/thickness, edge contactor, Quantity: 5
<i>CCDs to DAM</i>	0.2	in	Aluminum	Thickness, face contactor
<i>DAM to DASS</i>	0.015	in	Indium Foil	Thickness, face contactor
<i>FPGA to MEB</i>	10	W/K	--	Absolute, face contactor
<i>Frangibolt to DAM</i>	1.29	W/in ² /K	--	Conductance/Area, face contactor
<i>Radiator standoffs to radiator</i>	10	W/K	--	Absolute, face contactor
<i>Radiator standoffs to truss panel</i>	10	W/K	--	Absolute, face contactor
<i>TIL to DASS</i>	10	W/K	--	Absolute, face contactor
<i>TIL to electronics box</i>	10	W/K	--	Absolute, face contactor
Merged Nodes				
<i>Electronics box walls</i>	Edge nodes merged to simulate zero thermal resistance			

Heat Loading

Table 4 documents the heat loads applied to the PDR thermal model. REXIS draws power only when turned on. The trim heater is used during Orbit Phase A to warm the Frangibolt actuator prior to actuation. The MEB component power draws are applied as direct heat loads onto the PCBs where the components will be located. Modeling the power draws as point heat loads is conservative because the heat load, applied as a point source instead of a distributed load over the component area, must travel through the cross-section of FR4 to the electronics box walls and down into the spacecraft deck for dissipation. In Table 4, the heat loads of each component are equal to the component power draws and were obtained from the REXIS avionics engineering team.

Table 4: PDR thermal model heat loading

Component	Power Draw [W]	Notes
<i>CCDs</i>	0.108	Heat load for all four CCDs
<i>DE (each)</i>	1.845	Quantity: 2
<i>Trim Heater</i>	4.0	Prior to Frangibolt actuation in Orbit Phase A only
<i>MEB</i>		
<i>Voltage Converter: +1 VDC</i>	0.3	--
<i>Voltage Converter: +2.5 VDC</i>	0.26	--
<i>Voltage Converter: +3.3 VDC</i>	0.43	--
<i>Voltage Converter: +5 VDC</i>	3.92	--
<i>Voltage Converter: +12 VDC</i>	0.15	--
<i>Voltage Converter: +24 VDC</i>	0.1	--
<i>Analog/Digital Converter</i>	0.002	--
<i>Read-only Memory</i>	0.01	--
<i>RS422 (each)</i>	0.0004	Quantity: 2
<i>SD-Random Access Memory</i>	0.61	--
<i>SXM Shaper</i>	0.33	--
<i>Virtex-5 FPGA</i>	3	--

Thermo-physical and Optical Properties

Thermo-physical properties are properties of the bulk material of a component. These properties include thermal conductivity, density, specific heat, and effective emissivity. Effective emissivity captures the total effective emissivity of the radiation through the MLI blanket layers. Table 5 shows the thermo-physical property values assigned to each material. The components that correspond to each material are shown in Table 2.

Table 5: Thermo-physical properties

Material	Conductivity (W/in-C)	Density (kg/in³)	Specific Heat (J/kg-C)	Effective Emissivity
<i>Alumina</i>	0.762	0.6555	880	
<i>Aluminum</i>	4.26	0.04539	961.2	
<i>Beryllium</i>	3.825	0.03031	1882.8	
<i>Beryllium Oxide</i>	3.5179	0.03769	1047.6	
<i>Copper</i>	9.936	0.145189	385.2	
<i>G10/FR4</i>	.0064	0.00213	1500	
<i>Gold</i>	8.077	0.3163	129	
<i>Indium Foil</i>	2.1844	0.1198	0	
<i>MLI Blanket</i>	0	0	0	0.05
<i>Stainless Steel</i>	0.414	0.1316	504	
<i>TIL MLI</i>	0	0	0	0.1
<i>Titanium</i>	0.1981	0.072595	522	
<i>Torlon 5030</i>	0.009144	0.00213	1500	
<i>Tungsten</i>	4.265	0.3176	144	

Thermal Desktop uses optical properties to characterize a component's coatings on its inner and outer surfaces. Each component has a material or surface coating that is assigned a corresponding solar absorptivity and infrared emissivity in the optical properties toolbox. The solar absorptivity controls the amount of absorbed radiation in the visible spectrum and the emissivity controls the amount of absorbed radiation in the infrared spectrum. Table 6 shows the optical properties for the REXIS PDR thermal mode.

Table 6: Optical properties

Material	Solar Absorptivity (a)	IR Emissivity (e)	a/e
<i>Aluminized MLI</i>	0.13	0.03	4.33
<i>Aluminum</i>	0.15	0.08	1.875
<i>Aluminum, vapor deposited, on fiber glass</i>	0.15	0.07	2.143
<i>Bare M55J Composite</i>	0.78	0.93	0.839
<i>Black Paint</i>	0.90	0.90	1.0
<i>G10/FR4</i>	0.80	0.80	1.0
<i>Copper</i>	0.3	0.03	10.0
<i>Germanium Black Kapton (GBK)</i>	0.55	0.84	0.655
<i>Gold, electroplated</i>	0.23	0.05	6.0
<i>Gold, polished</i>	0.3	0.05	6.0
<i>Stainless steel</i>	0.42	0.11	3.818
<i>Tungsten</i>	0.6	0.05	12.0
<i>Torlon 5030</i>	0.8	0.8	1.0
<i>White paint, Generic</i>	0.52	0.93	0.559
<i>White paint, REXIS radiator</i>	0.50	0.80	0.625

Thermal Environment

The sun is modeled as a constant flux that varies as the inverse square to the heliocentric radius of the spacecraft, as shown in Chapter 2. The user inputs the solar flux and direction of sunlight for the spacecraft in its orbit, and Thermal Desktop applies sunlight from the supplied direction. The heat input on REXIS is dependent on the optical properties and surface areas of regions of REXIS exposed to direct sunlight. The asteroid Bennu is modeled using a spherical approximation where the temperatures of the asteroid are constant with time. The temperatures vary spatially on the asteroid and are input into Thermal Desktop as a function of latitude and longitude.

The effects of the sun, the asteroid, and the spacecraft are not captured using defined orbits and a geometry model of the spacecraft within the REXIS thermal model. Instead, a

REXIS reduced-order thermal model was incorporated into the spacecraft thermal model to generate predictions for each mission phase. The reduced-order model is a version of the PDR thermal model with fewer nodes that represents the important REXIS thermal physics. In this case, the reduced-order model was identical to the PDR level model, except the CCDs, TIL, radiator standoffs, and Frangibolt were not captured in the reduced-order model. The REXIS model was run with the spacecraft model to capture the influences of the spacecraft and the space environment. The OSIRIS-REx engineers generated sink temperatures and conductors to mathematically represent the thermal influence of the spacecraft and the environment on REXIS. By translating these conductors and temperatures into SINDA input cards, the REXIS PDR thermal model is run with the influence of the spacecraft and the space environment.

Test Case Results

A test case for the REXIS PDR thermal model is shown to demonstrate sample output from the working model. A notional spacecraft deck was constructed and the instrument was placed in a thermal environment similar to Orbit Phase B. As shown in Chapter 4, the spacecraft is in a 750 m altitude terminator orbit about the asteroid Bennu in Orbit Phase B and solar radiation comes from the +x-direction. For this sample case, the analysis ran until steady state temperatures were achieved. Figure 3 shows the temperature distribution on REXIS for the Orbit Phase B test case. The electronics box is approximately 30 °C and the telescope truss structure is approximately -70 °C and relatively isothermal.

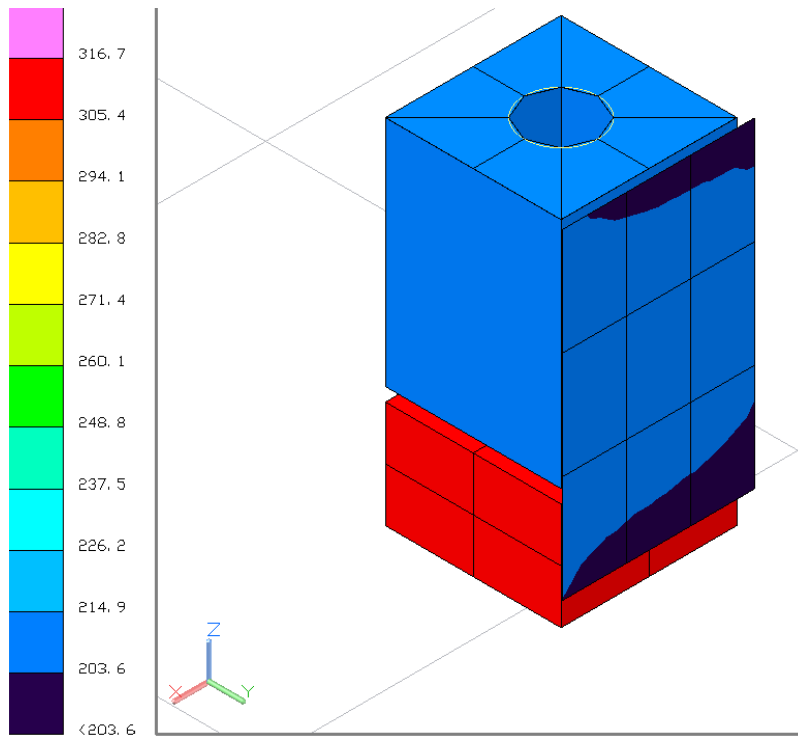


Figure 3: Orbit Phase B test case temperature distribution